Review

Pt–CeO$_2$-based composites in environmental catalysis: A review

M.A. Salaev **, A.A. Salaeva, T.S. Kharlamova, G.V. Mamontov *

Tomsk State University, 36, Lenin Ave., 634050, Tomsk, Russia

ARTICLE INFO	ABSTRACT
	The Pt–CeO$_2$-based composites have brought about a vivid research interest due to their use in advanced combustion engines, proton-exchange membrane fuel cells, etc. Complementing features of Pt and ceria particles cause numerous applications of such composites in environmental catalysis science and technology. The present review summarizes recent advances in Pt–CeO$_2$ chemistry and discusses the following key aspects: (1) catalyst preparation, including Pt and Ce-MOF-derived precursors, and treatment methods, (2) Pt-related factors: size, including single-atom formulations, and state, (3) CeO$_2$-related factors: morphology, surface defects, and derived features, (4) modification of catalyst composition, including the formation of bimetallic particles, (5) nature and structure of active sites, (6) features of metal–support interaction. The range of covered environmental catalytic applications includes oxidation processes (CO oxidation, VOCs abatement, soot oxidation, combustion of vehicle exhausts, etc.), reduction of nitroaromatics, CO$_2$ utilization (dry reforming of alkanes, CO$_2$ reduction, etc.), and photocatalytic reactions.

1. Introduction

Nowadays, CeO$_2$-based materials are widely used in catalysis science [1]. This is mainly due to the unique features of ceria, i.e., redox properties caused by Ce^{3+}/Ce^{4+} transitions, oxygen storage capacity, defect structure (including oxygen vacancies), own catalytic activity in a number of environmentally important reactions as well as its propensity to interact with various materials, especially noble metals [2]. Among the metals, Pt attracts attention due to its exceptional ability to convert various types of chemicals into value-added products that is caused by its high ability to activate C—H and C—O bonds. The Pt-based catalysts also feature high chemical and hydrothermal stability, while showing low tolerance to poisoning by some elements (e.g., chlorine). The combination of strong points of ceria and Pt causes wide opportunities to prepare various Pt–CeO$_2$-based catalytically active composites. In such systems, Pt usually plays the role of the active component, while in some applications (e.g., Ni-based catalysts for dry reforming of methane (DRM)) it is used as a (co)promoter. Ceria is usually used as a support with the fluorite structure, while in some composites it performs as a modifier for other supports (e.g., alumina, silica) or promoter for Pt component supported on such supports. Thus, the Pt–CeO$_x$ interfaces organized in catalysts constitute a large part of ceria applications that include but are not limited to electrooxidation of methanol [3–6],

ethanol [7], oxygen reduction reaction [8,9], valorization of methane (including DRM reaction) [10–15] and CO$_2$ [16–18], H$_2$ production through water-gas-shift (WGS) reaction [19], reforming [20–23] of alcohols, conversion of H$_2$ storing compounds [24]. Many publications deal with biomass conversion [25–27], alkane transformation [28], selective hydrogenation [29], hydrodeoxygenation [30], conversion of heterocyclic compounds [31], hydrosilylation [32], photocatalysis [33, 34], etc. Recently, a reverse system comprising the Pt-supported ceria composite also attracted great research attention [35–39].

The environmental catalysis comprises one of the largest segments of the application of Pt-CeO$_2$-based catalysts. The main market drivers are the automotive industry [40], manufacturing and application of alternative energy sources (alcohols, etc.) [41] as well as valorization of natural and artificial carbon-based sources (CH$_4$, CO$_2$, etc.) [42]. Indeed, pollution of both indoor and outdoor air with carbon monoxide and volatile organic compounds (VOCs) is considered a global problem, and special governmental regulations exist in many countries on their allowable concentrations. The effective utilization of such compounds is among the global environmental challenges. Many efforts have been made to address the challenge, with catalysis-based solutions demonstrating successes and high potential. Since CO oxidation is also a model reaction, many catalyst formulations were proposed, including metal-doped ceria [43]. Practical aspects of Pt−CO interaction are also

connected with poisoning [44] of the Pt sites in PEMFCs that reduces their exploitation terms and requires the introduction of additional components, e.g., ceria, to overcome the problem, naval submarine pollution control [45], etc.

The VOCs abatement technologies [46–49] are currently in demand in transportation, petroleum refining, fine organic synthesis, manufacturing of pharmaceuticals and pesticides, textile dyeing, etc. The composites utilizing Pt–CeO$_2$ interfaces are used in the abatement of various classes of VOCs, including but not limited to compounds containing O, S, Cl as well as hydrocarbons. The transportation vehicle exhausts are also the products of oxidation and incomplete combustion of hydrocarbon fuels significantly contributing to pollution of the atmosphere [50,51] with NO$_x$ [52], soot [53,54], hydrocarbons, etc.

Another important direction of the Pt–CeO$_2$ application is the utilization of nitroaromatic compounds (NCs) that are widely used in industry to prepare various dyes, agricultural chemicals (herbicides, pesticides, etc.), explosives, etc [55,56]. The NCs pollute the wastewaters being hazardous for the environment and human health. A promising way to reduce the harmful impact is to convert the NCs into less toxic compounds (e.g., NO$_2$ group into NH$_2$). Particular attention is paid to the photocatalytic conversion of greenhouse gases, oxidation of organic pollutants, and reduction of the harmful impact of dyes on the environment [57,58].

As a result of the abatement of various VOCs through the above-mentioned processes, large amounts of CO$_2$ are formed that require effective technologies for their utilization [59]. The main applications of Pt–CeO$_2$ interfaces in CO$_2$ valorization include DRM and reverse WGS reactions, while minor applications include ethane oxidative dehydrogenation [16], CO$_2$ hydrogenation [60], and CO$_2$ reduction [61].

High research interest is also reflected in the growing number of publications concerning Pt/CeO$_2$ composites and Pt–CeO$_2$ interfaces in catalytic reactions (Fig. 1). The environmental applications of Pt/CeO$_2$ composites constitute a large part of publications. The growing interest in Pt–CeO$_2$ for photocatalytic applications is observed due to the rapid development of photocatalysis during the last 20 years, including visible-light-response CeO$_2$-based photocatalysts [62]. The features of interfacial interactions (metal-support interaction, MSI) at the Pt–CeO$_2$ interfaces, including strong metal-support interaction (SMSI), are also under focused attention. Currently, single-atom catalysts are the new trend, and the intensive growth of the number of publications concerning single-atom Pt/CeO$_2$-based catalysts is observed starting from 2013.

Despite the high interest, currently, there is a lack of general review covering the major aspects of Pt–CeO$_2$ chemistry and their relationships with the catalytic performance. A recent review [1] deals with the fundamentals of catalytic applications of ceria-based materials.
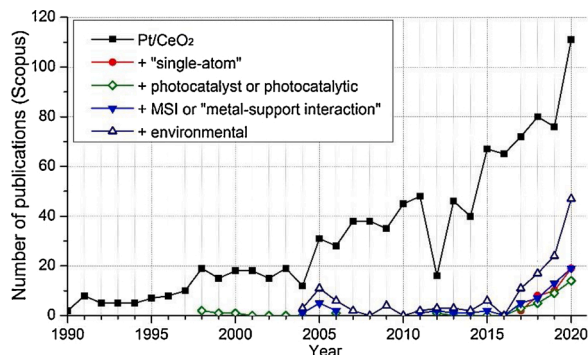

Fig. 1. Number of publications for Pt/CeO$_2$ in Scopus database (access date: 26 April 2021). Keywords for search: Pt/CeO$_2$: TITLE-ABS-KEY(Pt/CeO$_2$). For single-atom catalyst, photocatalysis, metal-support interaction, and environmental catalysts the following keywords were additionally added: "single-atom", "photocatalyst or photocatalytic", "MSI or metal-support interaction", and "environmental".

Although Pt/CeO$_2$-based materials are generally mentioned and compared with other metal/ceria composites in diesel engines and electrocatalytic applications, the peculiarities of Pt–ceria interactions are not considered in details. A recent review [2] carefully discusses the metal (M = Pt, Pd, Rh, Ru, Re, Ni, Au, Cu)–CeO$_2$ interfaces in several catalytic reactions (CO oxidation, WGS, CO$_2$ hydrogenation, CH$_4$ reforming, reforming of alcohols), while a large number of environmental catalytic reactions are not covered. Thus, the present review is focused on the recent advances and trends in designing, preparation, and environmental catalytic applications of Pt/CeO$_2$-based composites, including CO oxidation, VOCs abatement, applications in vehicles (three-way catalysts, soot combustion), conversion of nitroaromatic compounds, CO$_2$ as well as the opportunities in photocatalysis. We mostly consider the relevant publications within the period from 2016 to 2021. The following crucial aspects of Pt/CeO$_2$-based composites are discussed: (1) catalyst preparation, including Pt and Ce-MOF-derived precursors, and treatment methods, (2) Pt-related factors: size, including single-atom formulations, and state, (3) CeO$_2$-related factors: morphology, surface defects, and derived features, (4) modification of catalyst composition, including the formation of bimetallic particles, (5) nature and structure of active sites, (6) features of metal–support interaction. Theoretical insights are also provided where appropriate to deepen the understanding of the underlying processes. The outlook on the main directions of future research in the field of Pt–CeO$_2$-based environmental catalysts is also presented.

2. Catalyst preparation

The preparation method is known to influence on the Pt/CeO$_2$ catalyst performance by determining such features as size, shape, morphology of the Pt particles as well as their distribution within the catalyst grain. The morphology, electronic, redox, acid-base, and textural surface properties of the ceria support are also significantly affected and can be predesigned. Moreover, the interplay of both aspects tunes the strength and type of the metal–support interaction. The recent research activity within the considered period was mostly connected with the preparation of Pt–CeO$_2$-based composites using various techniques, including surface engineering approaches, the conditions of support and catalyst pretreatment (including reducing, oxidizing, plasma-assisted and thermal treatments) to affect the Pt and Ce states and sizes of species, organize the local surface atomic configurations and desired topological properties of interfacial sites. Recent publications also consider various precursors of Pt and ceria, with the latter being connected with the application of pristine and functionalized metal-organic framework (MOF)-derived ceria.

Tables 1–4 represent the selections of Pt–CeO$_2$ catalysts for CO oxidation (Table 1), VOCs abatement (Table 2), hydrogenation of nitroaromatic compounds (Table 3), and dry reforming of methane (Table 4). According to the data presented, many methods were proposed to synthesize the Pt–CeO$_2$-based catalysts with mono- and multimetallic formulations as well as those deposited on other supports. Large part of procedures is based on conventional approaches that can be used in industrial catalyst preparation protocols (e.g., (co)impregnation, (co)deposition, (co)precipitation, incipient wetness impregnation) [63–65]. Other methods are mostly used in fundamental studies (e. g., alcohol reduction [66], sol–gel synthesis [67], slurry phase impregnation [68], solvothermal method [69], surfactant template protocols [70], microemulsion approach [71], etc.). The catalyst synthesis procedures are often accompanied by the application of additional treatment techniques such as plasma- [72], microwave- [73], photo-assisted [74] approaches, microemulsion-mediated synthesis [75], pulsed laser ablation [76], etc. The application of such techniques allows additionally tuning of the Pt dispersion and distribution on the ceria surface.

Analysis of the catalyst performance (Tables 1–4) shows that the preparation method determines the catalyst activity and selectivity as well as physical-mechanical features in several environmentally

Table 1

Pt/CeO$_2$ catalyst performance in CO oxidation.

Catalyst designation	Reaction conditions	Preparation method	T$_{calc}$, °C/ t$_{calc}$, h	ω$_{Pt}$, wt.%	Pt size, nm	D$_{Pt}$, %	S$_{BET}$, m^2/g	T$_{50}$, °C	T$_{100}$, °C	TOF, s^{-1}	Ref.
Pt/CeO$_2$	12.5 mg/4 g quartz sand 1% CO, 20 % O$_2$, He balance flow rate = 50	ME	450/4	–	1–2	–	83	139	144	–	[75]
Pt@CeO$_2$ core–shell	0.05 g, 20 %vol. CO, 20 %vol. O$_2$, N$_2$ balance flow rate = 100	MSM	400/2	–	15	–	16.6	~185	~250	–	[93]
Pt/CeO$_2$ (IM)	0.36 g	IPM	400/6	1	2–6	45.8	35	–	60	–	
Pt/CeO$_2$ (DP)	0.02 % CO, 21 % O$_2$, N$_2$ balance flow rate = 350	DP	400/6	1	4–6	40.3	84	–	37	–	[63]
Pt/CeO$_2$ (IR)	WHSV = 60,000	IPM-RED	dried at 80 °C/12 h	1	2	46.7	33	–	70	–	
Pt/CeO$_2$-HT	125 mg	HT	175/12	1	–	53.5	114.9	~45	60	–	[83]
Pt/CeO$_2$-IM	1% CO, 1% O$_2$, Ar balance	IMP	–	1	–	36.5	105.5	~85	105	–	
CeO$_2$-AA-Pt-cal (Pt/CeO$_2$ + reducing reagent L-ascorbic acid)	100 mg 1% CO, 16 % O$_2$, N$_2$ balance	DP	300/1	1	atomic	–	–	~55	60	2.9·10^{-2}	[82]
CeO$_2$-IMP-Pt (Pt/CeO$_2$)	flow rate = 50	IWI	300/1	1.2	1–2	–	–	~58	~90	1.2·10^{-2}	
Pt/Ce-W (Pt/CeO$_2$)	0.25 cm^3	PLA (water)	450/–	4.2	15.6	–	59	142	~170	–	
Pt/Ce-Alc (Pt/CeO$_2$)	0.2 vol.% CO, 1.0 vol.% O$_2$,	PLA (alcohol)	450/–	2.7	9.8	–	61	74	~162	–	
Pt-Alc/Ce-W (Pt/CeO$_2$)	0.5 vol.% Ne, He balance flow rate = 1000 WHSV = 240,000	PLA (alcohol and water)	450/–	1.7	20.0	–	71	49	~130	–	[76]
Pt/Ce-700 (Pt/CeO$_2$)	0.36 g 0.2 vol.% CO, 1.0 vol.% O$_2$, 0.5 vol.% Ne, He balance	PA	700/-	4.58	–	–	71	191	~230	5.4·10^{-3}	[94]
Pt/CeO$_2$	32 mg + 0.15 g SiO$_2$ 1% CO + 20 % O$_2$/Ar flow rate = 40 WHSV = 75,000	AR	400/4	0.62	2.6	36.9	38	~70	~80	0.04	[95]
2.5 wt % Pt/CeO$_2$ reduced (300 °C/40% H$_2$)	200 mg 0.6 % CO, 1% O$_2$ GHSV = 50,000	IWI	500/2	2.5	1	–	81	~40	~60	–	[96]
10Pt/CeO$_2$	1% CO, 1% O$_2$, N$_2$ balance, 40 °C flow rate = 40 GHSV = 9600	SG IWI IMP	400/3	9.71	7.5	15	48	~55	~100	7.6·10^{-2}	[67]
Pt/CeO$_2$_S (S = subsequently steam-treated (hydrothermally aged))	30 mg 0.4 % CO, 10 % O$_2$, Ar balance WHSV = 200,000	IWI	800/12	1	atomic	–	25.6	~130	~150	–	[97]
R5-Pt/CeO$_2$ reduced (R5 = reduced at 550 °C)	75mg 6% CO, 40 % O$_2$, Ar balance	CP	650/–	0.5at %	1.7	–	–	~170	~200	–	[64]
Pt/CeO$_2$ (red)	0.01 − 0.1 g, 200 °C for reducing conditions: 13 % CO, 5% O$_2$, He balance for oxidizing conditions: 5% CO, 13 % O$_2$, He balance	DP	Dried at 80 °C/12	0.5	2.5	–	~107	~210	>300	0.48	[65]
Pt/CeO$_2$ (ox)								~187	>300	0.57	
Pt-CeO$_2$ (Gly-N) (Gly = glycine fuel, N = Pt(NH$_3$)$_4$(NO$_3$)$_2$ precursor)	16 mg/Al$_2$O$_3$ 2% CO, 2% O$_2$, 96% He flow rate = 50	SCS	–	1.14	4.2	–	47	~115	~150	–	[98]
1Pt/CeO$_2$_500	0.3 g / quartz glass 0.5 % CO, 4.5 % O$_2$ in He flow rate = 300	IWI	500/–	1	1.72	65.9	41	125	160	9.6·10^{-2}	[99]
Pt(2)/(800C)CeO$_2$ (ceria thermally pretreated at 800 °C)	0.05 g + 0.1 g α-Al$_2$O$_3$ 1000 ppm CO, 10 % O$_2$, N$_2$ balance, 190 °C flow rate = 200 GHSV = 120,000	IWI	500/2	2	<5	57	~135	140	~150	5.1·10^{-2}	[100]
Pt$_1$/PN-CeO$_2$ (PN = porous nanorod)	10 mg 1 %vol CO, 1 %vol O$_2$, Ar balance WHSV = 2100	HT PAD	350/3.5	0.57	atomic	–	–	~70	~85	–	[74]

Table 1 (*continued*)

Catalyst designation	Reaction conditions	Preparation method	T_{calc}, ºC/ t_{calc}, h	ω_{Pt}, wt.%	Pt size, nm	D_{Pt}, %	S_{BET}, m²/g	T_{50}, ºC	T_{100}, ºC	TOF, s⁻¹	Ref.
0.42% PtO$_x$/CeO$_2$ NWs-350 (NW = nanowire)	50 − 500 mg + SiO$_2$ 13 % CO, 33 % O$_2$, He balance	HT	–	0.42	0.6	100	~40	–	–	1.3·10⁻²	[101]
Rod/Pt	25 mg + 975 mg SiO$_2$ CO and O$_2$ flow rate =			1.0at.			78	~125	~150		
Cube/Pt	2.4 mL min⁻¹, N$_2$ balance	MAP	Dried	1.1at.	2−3	–	14	~140	~180	–	[102]
Octa/Pt	flow rate = 50			1.3at.			20	~165	~200		
Pt/CeO$_2$ HS (HS = hollow sphere)	50 mg 1% CO/20 % O$_2$/79% N$_2$ flow rate = 67 WHSV = 80,000	ST	300/4	1.4	5.7	–	190	155	158		[69]
0.5 % Au$_2$Pt$_3$/CeO$_2$	0.2 Vol.% CO, 1.0 Vol. % O$_2$ in an inert gas 0.36 g	IWI	200/2	0.29	3–5 (Au$_2$Pt$_3$)	–	~120	~60	~100	–	[103]
Pt/CeSn-700 (Pt/SnCeO$_x$)	0.2 vol.% CO, 1.0 vol. % O$_2$, 0.5 vol.% Ne, He balance	PA	700/-	2.37	–	–	39	175	~225	19.8·10⁻³	[94]
FeO$_x$/Pt/CeO$_2$	32 mg + 0.15 g SiO$_2$		400/4	0.61	2.6	28.5	30	~-8	~20	1.10	
CoO$_x$/Pt/CeO$_2$	1% CO + 20 % O$_2$/Ar flow rate = 40	DP	400/4	0.61	2.7	31.2	33	~5	~30	0.88	[95]
NiO$_x$/Pt/CeO$_2$	WHSV = 75,000		400/4	0.60	2.6	33.3	31	~40	~60	0.24	
4%Pt-16 %CeO$_2$/SiO$_2$	0.005–0.1 %CO, 21 % O$_2$, N$_2$ balance, 5% CO in N$_2$	IWI	300/2	4	–	42	257	–	–	0.028	[104]
Pt/CSAO (CSAO = Ce-Si-Al-O)	1% CO, 10 % O$_2$, and Ar balance flow rate: 200 GHSV = 48,000	HT + AlD Pt	–	–	3.8	–	8.5	~180	~350	–	[105]
Pt/Ce$_{0.8}$Zr$_{0.2}$O$_2$	50 mg 1 vol% CO, 21 vol% O$_2$, N$_2$ balance WHSV = 60,000	IMP	600/2	0.4	4	–	71.9	121	130	0.156	[106]
Pt/AlCe-AH (Pt/AlCeO$_x$)	0.02 g / 1 g SiC	P (NH$_4$OH)	500/2	1	–	24.0	102	~105	~122	–	
Pt/AlCe-PH (Pt/AlCeO$_x$)	1vol% CO, 4 vol% O$_2$ and 95 vol% N$_2$	P (KOH)	500/2	1	–	12.9	110	~120	~135	–	
Pt/AlCe-SH (Pt/AlCeO$_x$)		P (NaOH)	500/2	1	–	10.1	104	~125	~145	–	[107]
Pt/AlCe-PC (Pt/AlCeO$_x$)	flow rate = 200	P (K$_2$CO$_3$)	500/2	1	–	6.6	58	~182	~190	–	
Pt/AlCe-SC (Pt/AlCeO$_x$)		P (Na$_2$CO$_3$)	500/2	1	–	5.7	17	~188	~197	–	
1 wt.%Pt/5 wt.%CeO$_2$-Al$_2$O$_3$	50 mg / 500 mg quartz 8 % O$_2$, 0.1% CO, 0.5 % C$_3$H$_6$, N$_2$ balance flow rate = 500 WHSV = 600	FSP	500/5	0.8	<1	–	~130	~140	~193	–	[108]

Imp – impregnation; IWI – incipient wetness impregnation; Red – reduction; DP – deposition-precipitation; CP – co-precipitation; HT – hydrothermal process; MSM – modifier Stöber method; ME – microemulsion-mediated synthesis with SiO$_2$; PLA – pulsed laser ablation; PA – plasma-arc technique; AR – ethylene glycol reduction; FSP – flame spray pyrolysis; PAD – Photoassisted deposition; SG – sol–gel; UP – urea precipitation; MAP – Microwave-assisted precipitation; ST – solvothermal method; SCS – solution combustion synthesis; P – precipitation; D_{Pt} – Pt dispersion; ω_{Pt} – Pt loading; WHSV – weight hourly space velocity, mL g⁻¹ h⁻¹; GHSV – gas hourly space velocity, h⁻¹, flow rate in mL min⁻¹.

important reactions. The preparation method (including catalyst pre-treatment procedures and Pt precursor) significantly affects the dispersion, morphology, and state of Pt species in the final catalysts. The Pt dispersion is also affected by the catalyst pretreatment procedures (e.g., plasma treatments or oxidative/reductive treatments). One way to improve the dispersion and stabilize the formed Pt species is to use high-surface-area supports (including high-surface ceria). Thus, new metal redispersion strategies are required. The role and mechanisms of involvement of surface functional groups can also be envisioned. It is noteworthy also that most catalysts were tested under ideal conditions, while it is preferable to test them under the simulated real exhaust conditions taking into account the probable effects of humidity and poisoning. With that, it is crucial to apply advanced characterization techniques to determine the metal dispersion, including statistical analysis based on the TEM or environmental TEM data, chemisorption methods, etc.

For CO oxidation (Table 1) conventional methods allow producing the composites with a rather high surface area and small particle size, including single-atom formulations, with the interplay between these features being important. Such composites show low-temperature (room temperature and below) CO oxidation activity at space velocities of 50,000–75,000 h⁻¹. At the same time, such methods as pulsed laser ablation or incipient wetness impregnation allowed producing the catalysts operating at GHSV of no less than 200,000 h⁻¹. Moderate calcination temperatures (300−450 °C) are adequate to ensure lower T100 % and higher time-on-stream values. The size effect of Pt particles is not pronounced implying that other factors (e.g., ceria morphology) feature an equal or higher impact on the catalyst performance. Application of MO$_x$ promoters based on transition metals (Fe, Co, etc.) allows reducing the T100 % values as compared to unpromoted samples. One can expect the performance enhancement upon subsequent catalyst modification by other transition metal compounds (e.g., Mn-based components) as well as the use of ordered supports. Similar effects are observed for the DRM catalysts (Table 4). With that, it is crucial to compare the catalyst performance at similar reaction conditions.

The Pt-CeO$_2$-based catalysts were actively used in the abatement of different types of VOCs, including alkanes, alcohols, aldehydes, ketones, ethers, aromatics as well as Cl- and O-containing compounds (Table 2).

Table 2

A selection of Pt/CeO_2 catalysts for VOCs abatement.

Catalyst designation /Preparation method	Type of VOC	Reaction conditions	ω_{Pt}, wt.%	Pt size, nm	S_{BET}, m^2 g^{-1}	T_{50}, °C	T_{100}, °C	TOF, s^{-1}	Ref.
CePt500-red ($Ce_{1-x}Pt_xO_2$) citric acid method	methane	50 vol % CH_4, 3 vol % O_2, Ar balance GHSV = 30,000 200−500 °C	10	–	33	349	360	–	[109]
Pd-Pt/La_2O_3-Y_2O_3-CeO_2-ZrO_2 IWI	methane	5 ppm SO_2, 30 ppm NO_2, 120 ppm NO, 3200 ppm CH_4, 10% O_2, 12% H_2O, N_2 balance GHSV = 80,000 450 °C	0.48	1−2	75	430	550	–	[110]
Pt/CeTi-11 (Pt/CeO_2-TiO_2, pH of solution is 11) modified ethylene glycol (EG) reduction method	n-hexane	300 mg 1000 ppm of VOC flow rate = 75 GHSV = 15,000	0.5	1.53	25	255	310	–	[244]
Pt/Ce-USY-ex ion-exchange method	n-hexane	300 mg catalyst 1000 ppm of VOC flow rate = 75 GHSV = 15,000	0.43	2.4	545	163	200	–	[125]
Pt/Ce-USY-ex ion-exchange method	benzene	300 mg catalyst 1000 ppm of VOC flow rate = 75 GHSV = 15,000	0.43	2.4	545	180	190	–	[125]
Pt/CeTi-11 (Pt/CeO_2-TiO_2, pH of solution is 11) modified ethylene glycol (EG) reduction method	benzene	0.3 g catalyst 1000 ppm flow rate = 75 GHSV = 15,000	0.5	1.53	25	148	164	–	[244]
Pt(1 wt%)/Al_2O_3–CeO_2 (30 wt%) IWI	benzene	flow rate=70 1000 ppm of VOC WHSV = 8400	1.0	5−20	68	216	T_{80} = 300	–	[111]
0.2 % Pt/CeO_2(400) (Ce-MOF-120 calcined at 400 °C) high-temperature liquid phase reduction	benzene	1 ppm of VOC GHSV = 20,000	0.2	–	93.7	168	200	–	[112]
1.0% Pt/CeO_2-MM HT	benzene	2.0 g m^{-3} of VOC WHSV = 48,000	1.0	1.8	57.2	120	160	–	[205]
1.0% Pt/CeO_2-NC HT			1.0	2.8	19.2	270	–	–	
Pt/CeO_2 IWI	toluene	60 mg 0.1 % C_7H_8 in air flow rate = 200	0.5	2.5	3	250	~420	–	[113]
(Pt/CeO_2)-P HT + DBDP	toluene	120 mg 200 ppm toluene in 20 % O_2/N_2 flow rate = 100 WHSV = 50,000	0.77	3.27	87	185	230	$9.88^{.}10^{-4}$ (TOF_{Pt})	[72]
Pt/CeO_2 IWI + thermal and plasma treatments	toluene	100 mg + 400 mg silica 200 ppm toluene 0.02 % toluene, 20 % O_2, N_2 balance	0.79	2.4	96	~165	~225	$7.9^{.}10^{-3}$	[114]
Pt/EC-2.5 STP	toluene	0.40 g 0.09 vol% of toluene flow rate = 200 GHSV = 50,000, 160 °C	0.65	–	133	~170	~200	$5.52^{.}10^{-2}$ (TOF_{Pt})	[70]
Pt/CeO_2-r HT + IMP	toluene	200 mg + 800 mg silica 1000 ppm toluene dry air 0.1 % toluene, 20 % O_2, N_2 balance	0.19	(8 ± 2) (100–200)	103	138	180	$10.4^{.}10^{-2}$ (TOF_{Pt})	[66]
Pt/CeO_2-p HT + AR	toluene	WHSV = 48,000	0.18	25 ± 5	129	150	200	$6.91^{.}10^{-2}$ (TOF_{Pt})	
Pt/CeO_2-c HT + AR	toluene		0.18	100–300	15	170	230	$3.34^{.}10^{-2}$ (TOF_{Pt})	
Pt/CeO_2-1.8 HT + AR	toluene	200 mg + 800 mg silica 1000 ppm toluene dry air (20 % O_2/N_2, 160 mL min^{-1}) 0.1 % toluene, 20 % O_2, N_2 balance WHSV = 48,000	0.24	1.88	99	132	160	$6.75^{.}10^{-3}$ (TOF_{Pt})	[115]
Pt(1 wt.%)/Al_2O_3-CeO_2(30 wt.%) USP IMP	toluene	1300−3000 ppm GHSV = 12,000	1.0	12.7	92	~130	180	–	[116]
2%Pd–0.8 %Pt/CeO_2-10-γ-Al_2O_3 IWI	toluene	243 ppm GHSV = 5000	0.8	–	130.09	210	240	–	[117]
Pt(1 wt%)/Al_2O_3–CeO_2 (30 wt%)	toluene	flow rate=70 1000 ppm of VOC	1.0	5−20	68	190	250	–	[111]

Table 2 (*continued*)

Catalyst designation /Preparation method	Type of VOC	Reaction conditions	ω_{Pt}, wt.%	Pt size, nm	S_{BET}, m² g⁻¹	T_{50}, °C	T_{100}, °C	TOF, s⁻¹	Ref.
IWI		WHSV = 8400							
Pt(1 wt%)/Al₂O₃–CeO₂ (30 wt%) IWI	xylene	flow rate=70 1000 ppm of VOC WHSV = 8400	1.0	5–20	68	186	300	–	[111]
Pt1-CeO₂{100} (single-atom catalyst) IMP	methanol	0.28 g flow rate = 152 GHSV = 30,400	0.061	1.07	39	33	52	0.68	[175]
Pt1-CeO₂{100} (single-atom catalyst) IMP	ethanol	flow rate = 180 GHSV = 36,000	0.061	1.07	39	91	138	–	[175]
Pt-10Ce/C(CI) (10 %wt. CeO₂) IMP	ethanol	150 mg 1000 ppm of ethanol in air flow rate = 100	1.0	–	– (1324 for support)	74	125	–	[151]
Pt/Co₃O₄–CeO₂	isopropyl alcohol	toluene, ethyl acetate, isopropyl alcohol, ethylbenzene, and ethanol in the prepared gas were 0.4 ×10³ ppm, 0.9 × 10³ ppm, 0.9 × 10³ ppm, 0.3 × 10³ ppm, and 0.8 × 10³ ppm	5.0	–	–	150	250	–	[122]
PVP-assisted deposition and stiring in crucible		flow rate = 100 mL min⁻¹							
Pt(7 wt. %)/Ce₀.₆₈Zr₀.₁₇Sn₀.₁₅O₂(16 wt.%)/ZrO₂(24 wt.%)/SBA-16 IMP	phenol	0.4 g catalyst 1000 ppm phenol aqueous solution (10 mL)	7.0	–	138	–	80	–	[118]
Pt/Al₉Ce₁ IMP	Formaldehyde	0.1 g condensed HCHO(38 %)	0.8	3.0	318	–	RT	–	[119]
Pt/Ce-2 ME + IMP	Formaldehyde	0.1 g condensed HCHO(38 %)	1.19	–	58	–	RT	–	[120]
Pt1-CeO₂{100} (single-atom catalyst) IMP	Formaldehyde	flow rate = 210 GHSV = 42,000	0.061	1.07	39	20	57	–	[175]
Pt1-CeO₂{100} (single-atom catalyst) IMP	acetaldehyde	flow rate = 210 GHSV = 42,000	0.061	1.07	39	103	158	–	[175]
Pt/CeO₂/ZSM-5 IMP	acetaldehyde	50 mg flow rate = 24 GHSV = 1200	1.0	6.1	–	149	197	–	[121]
Pt/Co₃O₄–CeO₂ PVP-assisted deposition and stiring in crucible	ethyl acetate	100 mL min⁻¹ toluene, ethyl acetate, isopropyl alcohol, ethylbenzene, and ethanol in the prepared gas were 0.4·10³ ppm, 0.9·10³ ppm, 0.9·10³ ppm, 0.3·10³ ppm, and 0.8·10³ ppm	5.0	–	–	190	275	–	[122]
Pt1-CeO₂{100} (single-atom catalyst) IMP	ethyl acetate	flow rate = 180 GHSV = 36,000	0.061	1.07	39	135	195	–	[175]
Pt/CeTi-11 (Pt/CeO₂-TiO₂, pH of solution is 11) modified ethylene glycol reduction method	ethyl acetate	0.3 g 1000 ppm of VOC flow rate = 75 GHSV = 15,000	0.5	1.53	25	230	290	–	[244]
Pt/Ce-USY-ex ion-exchange method	ethyl acetate	300 mg 1000 ppm of VOC flow rate = 75 GHSV = 15,000	0.43	2.4	545	182	210	–	[125]
Pt1-CeO₂{100} (single-atom catalyst) IMP	methyl ethyl ketone	flow rate = 180 GHSV = 36,000	0.061	1.07	39	130	176	–	[175]
0.6 %Pt/CeO₂ IWI	dichloromethane	400 mg 500 ppm of VOC GHSV = 143,793 1.5 vol.% H₂O	0.6	~2.4	82	400	–	–	[123]
Pt/Ce-Al IWI		100 mg catalyst 500 ppm of DCM 1.5 vol.% H₂O	1.0	10	85	470	T_{90} = 560	–	[124]
Pt-Au/Ce-Al surface redox reactions in aqueous phase	dichloromethane	WHSV = 720	1.0	10–30	85	430	T_{90} = 570	–	[124]
Pt/CeTi-11 (Pt/CeO₂-TiO₂, pH of solution is 11)	1,2-dichloroethane	0.3 g 1000 ppm of VOC flow rate = 75	0.5	1.53	25	260	350	–	[244]

Table 2 (*continued*)

Catalyst designation /Preparation method	Type of VOC	Reaction conditions	ω_{Pt}, wt.%	Pt size, nm	S_{BET}, m^2 g^{-1}	T_{50}, °C	T_{100}, °C	TOF, s^{-1}	Ref.
modified ethylene glycol (EG) reduction method		GHSV = 15,000							
Pt/Ce-USY-ex ion-exchange method	1,2-dichloroethane	300 mg catalyst 1000 ppm VOC flow rate = 75 GHSV = 15,000	0.43	2.4	545	225	300	–	[125]
0.90Ru$_{2.77}$Pt/3DOM CeO$_2$ polyvinyl alcohol (PVA)-protected NaBH$_4$ reduction route	trichloroethylene	250 °C 1000 ppm of TCE, 20 vol%O$_2$, N$_2$ balance flow rate = 16.7 WHSV = 20,000	0.37	3.4	39	321	T$_{90}$ = 373	1.0	[126]
Pt/CeO$_2$ IMP Pt-1W/CeO$_2$ Co-IMP Pt-4W/CeO$_2$ Co-IMP Pt-8W/CeO$_2$ Co-IMP	Chlorobenzene (CB) / 1,2-dichlorobenzene (1.2-DCB) / benzene (B)	200 mg 1000 ppm of VOC, 10 % O$_2$, N$_2$ balance feed flow = 100 GHSV = 60,000	0.52 0.43 0.46 0.44	– – – –	94 88 82 71	327 / 334 / 266 273 / 308 / 172 263 / 293 / 174 270 / 285 / 192	500 / 500 / 360 450 / 450 / 215 395 / 420 / 200 385 / 400 / 222	– 7.3·10^{-4} 2.9·10^{-4} 1.4·10^{-4}	[127]
Pt/Ce-Al (Pt/CeO$_2$-Al$_2$O$_3$) IWI	dimethyl disulfide	300 mg 500 ppm of DMDS WHSV = 720	1.20	–	70	380	T$_{90}$ = 460	–	[231]

IMP – impregnation; IWI – wet impregnation; USP IMP – ultrasound–plasma assisted impregnation; HT – hydrothermal method; DBDP – dielectric barrier discharge plasma; ME – microemulsion process; RME – reverse-micelle emulsion process; STP – surfactant template protocol; AR – alcohol reduction; Co-IMP – co-impregnation; PVP – polyvinylpyrrolidone, ω_{Pt} – Pt loading; WHSV – weight hourly space velocity, mL g^{-1} h^{-1}; GHSV – gas hourly space velocity, h^{-1}, flow rate in mL min^{-1}.

Table 3

A selection of Pt/CeO$_2$ catalysts for nitroaromatic compounds hydrogenation.

Catalyst	Nitroaromatic compound	Reducing reagent	Reaction temperature	Rate constant (s^{-1}) or Conversion (X, %) and Selectivity (S, %)	Ref.
Pt-CeO$_2$	4-NP (ethanol:water = 2 : 1)	H$_2$ (1.5 MPa)	25 °C	X = 100 %; S = 99 % after 6 h	[55]
Pt/CeO$_2$ catalysts with different Pt particle sizes	p-CNB (ethanol)	H$_2$ (1 MPa)	40 °C	X = 100 %; S = 100 % for 0.6 wt.% Pt	[128]
Pt/CeO$_2$ surface-embedded (se) or surface-loaded (sl)^a	4-NP (aqueous solution)	NaBH$_4$ (aqueous solution)	25 °C	1.95·10^{-2} 3.58·10^{-2} 1.95·10^{-2} 9.75·10^{-3}	[129]
Pt/meso-CeO$_2$ Pt/nano-CeO$_2$	4-NP (aqueous solution)	NaBH$_4$ (aqueous solution)	RT	6.03·10^{-3} 4.07·10^{-3}	[130]
Pt/meso-CeO$_2$ Pt/meso-CeO$_2$Co$_{30}$ Pt/mesoCeO$_2$Co$_{10}$	4-NP (aqueous solution)	NaBH$_4$ (aqueous solution)	RT	6.03·10^{-3} 9.63·10^{-3} 11.30·10^{-3}	[86]
disk-like Pt/CeO$_2$-p-TiO$_2$ (treatment at RT, 300 °C, 550 °C, 700 °C)	4-NP (aqueous solution)	NaBH$_4$ (aqueous solution)	RT	6.96·10^{-3} (RT) 6.19·10^{-3} (300 °C) 15.08·10^{-3} (550 °C) 5.22·10^{-3} (700 °C)	[131]
CeO$_2$ Fe$_3$O$_4$ Fe$_3$O$_4$@CeO$_2$ Fe$_3$O$_4$@CeO$_2$/Pd Fe$_3$O$_4$@CeO$_2$/Pt Fe$_3$O$_4$@CeO$_2$/Pd-Pt	4-NP (aqueous solution)	NaBH$_4$ (aqueous solution)	RT	0 0.33·10^{-3} 0.50·10^{-3} 21.5·10^{-3} 17.8·10^{-3} 10.3·10^{-3}	[56]
Pt/CeO$_2$ Pt/Fe$_3$O$_4$–CeO$_2$	4-NP (aqueous solution)	NaBH$_4$ (aqueous solution)	RT	3.19·10^{-3} 5.47·10^{-3}	[87]
PLAL-Pt$_{100-x}$Au$_x$-alloy-NP/CeO$_2$-NT hybrids (Pt-Au/CeO$_2$)	4-NP (aqueous solution)	NaBH$_4$ (aqueous solution)	RT	3.5 10^{-2} (x = 0) 10.87 10^{-2} (x = 50) 5.5 10^{-2} (x = 30) 10.14 10^{-2} (x = 70) 1.08 10^{-2} (x = 100)	[132]
Pt-Ag/CeO$_2$	4-NP (aqueous solution)	NaBH$_4$ (aqueous solution)		15.93·10^{-3}	[133]
Pt@CeO$_2$/RGO	4-NP (aqueous solution)	NH$_3$BH$_3$ (aqueous solution)	24 °C	7.17·10^{-3}	[85]

^{a} Nanostructures before heat treatment (se) after heat treatment at 500 °C (se500), nano-structures before heat treatment (sl) after heat treatment at 500 °C (sl500). 4-NP – 4-nitrophenol, p-CNB – p-chloronitrobenzene.

Table 4

A selection of DRM catalysts.

Catalyst designation / Preparation method	Reaction conditions	ω_{Pt}, %	S_{BET}, m^2/g	Catalyst performance	Ref.
PtO$_x$/ MgO–Al$_2$O$_3$ IMP	80 mg 650 °C	0.9	163	X(CH$_4$) = 81 (72)%; H$_2$/CO = 0.8	[134]
PtO$_x$/ CeO$_2$–La$_2$O$_3$ IMP	CH$_4$:CO$_2$:N$_2$ = 1:1:1 700 °C	1.0	151	X(CH$_4$) = 90 (78)%; H$_2$/CO = 0.9	
PtO$_x$/ CeO$_2$–Al$_2$O$_3$ IMP		0.9	87	X(CH$_4$) = 50 (85)%; H$_2$/CO = 0.8	
Pt/1CeO$_2$–ZrO$_2$ IWI	0.05 g 550 °C CH$_4$(20%), CO$_2$(20%), N$_2$ balance flow rate: 100 mL min^{-1}	1	197	X(CH$_4$) = 20.1 %; X(CO$_2$) = 21.0 % H$_2$/CO = 0.48	[135]
PtCo/CeO$_2$ SPI	20 mg, CO$_2$: CH$_4$:Ar = 10:10:60 1 atm, 600 °C	1.67	~35	X(CH$_4$) = 14.3 % X(CO$_2$) = 25.5 %	[68]
Pt$_{25}$Ni$_{75}$/Ce (Pt-Ni/CeO$_2$) P	0.050 g 500–800 °C CH$_4$(33%): CO$_2$(33%), N$_2$ balance total flow = 90 mL min^{-1}	31.23 at.	67	At 650 °C: X(CH$_4$)=~43 %; X(CO$_2$)= ~46 % H$_2$/CO = 0.65	[136]
Pt/FeMo/Ni/ Al$_2$O$_3$-CeO$_2$ IWI	300 mg + sand (1:6) CH$_4$/CO$_2$ = 50/50 GHSV = 12,000 mL g$_{cat}$$^{-1}$ h^{-1} 700 °C	2.258 (Fe, Mg, Pt)	77	X(CH$_4$) = 81%; X(CO$_2$) = 86% H$_2$/CO = 0.91	[137]
Pt/CePr/Al$_2$O$_3$ IWI	SiC/catalyst ratio = 1.5 CH$_4$:CO$_2$ = 1:1 flow rate = 100 mL min^{-1} 800 °C	1.0	118	X(CH$_4$) = 67%; X(CO$_2$) = 72% H$_2$/CO = 0.90	[138]
Pt/CeNb/Al$_2$O$_3$ IWI		1.1	112	X(CH$_4$) = 58%; X(CO$_2$) = 68% H$_2$/CO = 0.88	
Pt/CeZr/Al$_2$O$_3$ IWI		1.1	116	X(CH$_4$) = 63%; X(CO$_2$) = 72% H$_2$/CO = 0.87	

SCS – solution–combustion synthesis; Co-P – coprecipitation; IMP – impregnation; DP – deposition–precipitation; SG – sol–gel; FC – flame combustion; Co-D – codeposition; HT – hydrothermal method; Co-IMP – coimpregnation method; IWI – wet impregnation method; SPI – slurry phase impregnation; P – precipitation; ω_{Pt} – Pt loading; WHSV – weight hourly space velocity; GHSV – gas hourly space velocity.

The VOCs abatement usually requires the catalysts with higher specific surface and higher T100 % values as compared to CO oxidation. At the same time, lower Pt loadings are used. It is noteworthy that conventional impregnation techniques allow producing the high-performance catalysts for the removal of O-containing VOCs (methanol, ethanol, iso-propanol, formaldehyde, acetaldehyde, ethyl acetate, etc.) as well as dichloromethane. A higher number of C atoms in the alcohol molecule (or the presence of more branched radical) usually requires higher temperatures to completely remove the VOCs. Both high surface area and Pt particle sizes are beneficial for low-temperature activity in the removal of O-containing VOCs.

The high-performance catalysts for the removal of alkanes (methane, hexane) and aromatic VOCs (benzene, toluene, xylene) feature different behavior, and the application of hydrothermal treatment procedures during the preparation of supports and/or catalysts is usually favorable for the overall performance of the final sample. Higher Pt content ensures higher activity in methane combustion, with the sample prepared using citric acid showing superior performance. The higher surface area of the composite is beneficial for hexane removal, with the sample prepared using the ion-exchange method being more active. In benzene removal, the catalysts featuring moderate surface area and Pt size below 2 nm show the highest performance, while in toluene oxidation, the specific surface is almost independent of the Pt size. Due to the presence of the second methyl group, xylene is removed at a higher temperature as compared to toluene.

The abatement of S- or Cl-containing VOCs generally requires elevated temperatures that can be connected with both geometric and electronic factors. In particular, the presence of the aromatic ring in pristine and Cl-substituted benzenes causes the application of higher energy costs to remove these VOCs. The Pt loadings below 0.52 wt% showed rather high activity, with the sample produced using the ion-exchange approach being superior.

Although the Pt-CeO$_2$-based composites showed the capability to selectively transform a number of typical VOCs (e.g., glycerol [77], propane [78], butane [17], cyclohexane [79], methyl cyclohexane [80], acetonitrile [81], etc.), still the total oxidation activity can be further studied in more extent for other typical VOCs (e.g., naphthalene, eth-ylenediamine, methyl mercaptan, olefins, etc.).

In the reduction of nitroaromatic compounds (Table 3), the Pt-CeO$_2$ catalysts show near room-temperature activity in aqueous, alcoholic, and mixed water-alcohol solutions, and different reducing agents (H$_2$, NH$_3$BH$_3$, NaBH$_4$). However, the exact reaction mechanisms in each case and their effect on such behavior remain debating.

Recently, high research attention was given to facile surface engineering approaches. For instance, in CO oxidation reaction, the utilization of molecule – surface charge transfer adducts implying the generation of an adequate amount of Ce^{3+} defective sites through the adsorption of reductive ascorbic acid molecules [82] was proposed. A spontaneous surface redox reaction between the Ce(OH)$_3$/CeO$_2$ and [PtCl$_6$]$^{2-}$ to obtain highly dispersed Pt nanocatalyst anchored on porous CeO$_2$ nanorods in a Cl-free environment was introduced to show strong electronic MSI (Fig. 2) [83]. It is noteworthy that the formation of the active surface Ce^{3+} sites with the participation of Pt species without an oxygen supply or the application of reducible molecules was also proposed [84].

To prepare the catalysts for conversion of nitroaromatic compounds, an inorganic approach to synthesize Pt@CeO$_2$ multicore@shell nano-spheres was proposed [85], where Ce(NO$_3$)$_3$ interacted with K$_2$PtCl$_4$ in an alkaline aqueous solution and Ar atmosphere without adding reducing agents and surfactants. The structure was stable upon calcination at 600 °C for 5 h.

The encapsulation of metal NPs (Pt, Au, Ag, and Pd) into the hier-archically self-assembled 2D ceria nanoplatelets was proposed [71] using the buckling of colloidal ceria nanoplatelets in oil-in-water emulsions (Fig. 3A). The Pt NPs (~2 nm in diameter) were obtained through the interaction of Pt(acac)$_2$, benzyl alcohol, and oleylamine. Ceria platelets and metal nanoparticles are mixed in chloroform with a desired nanoparticle ratio. The Pt/CeO$_2$ catalyst showed superior activity in 4-nitrophenol reduction and CO oxidation (Fig. 3B). It is note-worthy that the completeness of removal of organic ligands from the NPs and the role of residual ligands in catalysts performance remain unclear.

The composites with the ordered structure for 4-nitrophenol reduction were introduced. The KIT-6-based template synthesis utilizing polyamidoamine (PAMAM) dendrimers that allowed stabilizing the Pt NPs on ordered mesoporous ceria [86] combined hydrothermal and hard template techniques. The normalized rate constant was significantly higher than for a number of Pt-based catalysts prepared by
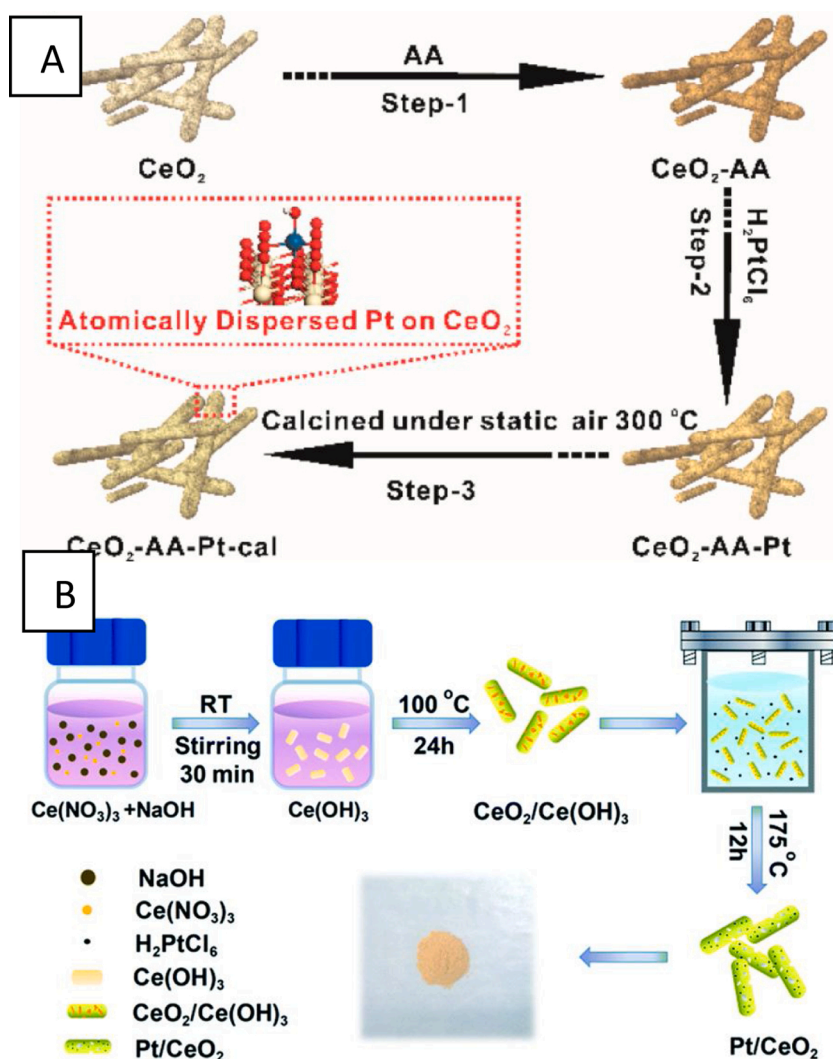
Fig. 2. (A) Schematic illustration of the L-ascorbic acid (AA)-assisted reduction synthesis of the atomically dispersed Pt/CeO$_2$ catalyst (CeO$_2$-AA-Pt-cal). Reproduced with permission from Ref. [82]. Copyright Royal Society of Chemistry. (B) Synthetic routine of the highly dispersed Pt/CeO$_2$ catalyst through the spontaneous surface redox reaction between Ce(OH)$_3$/CeO$_2$ nanorods and metal salt by a hydrothermal process. Reproduced with permission from Ref. [83]. Copyright Royal Society of Chemistry.

precipitation or modified solvothermal methods. Ordered mesoporous 0.1 %Pt/Fe$_3$O$_4$–CeO$_2$ heterostructured gel comprising a magnetic Fe$_3$O$_4$ layer, ceria core and Pt NPs evenly dispersed in ceria matrix was also fabricated using aerogel technology and chemical deposition [87]. The Fe$_3$O$_4$ crystal sheet thickness was ~16 nm. High photocatalytic activity expressed in hydrogen production rate (4.967 mmol/g) was achieved due to fast reactant diffusion and higher content of active sites ensured by mesoporous ceria matrix. The thermodynamically favorable Fe^{2+}–Ce^{4+} transfer due to oxidation-reduction cycle of Ce^{4+} in the presence of BH$_4^-$.

Although such catalysts featured high surface area and multiple defect sites, these features can be for good and for bad in the catalytic reaction since, from one hand, the defective sites are usually more reactive, while, from the other hand, their inhomogeneous structure implies unequal distribution of catalyst components resulting in inhomogeneous activity and selectivity. It is noteworthy also that the large-scale approach (e.g., [85]) will require high attention to the composition of impurities in the feedstock that may drastically affect the catalyst performance.

The positive effect of dielectric barrier discharge plasma treatment was demonstrated in catalytic toluene oxidation [72]. The plasma treatment results in the breaking of ceria nanorods to increase the surface area and formation of a higher amount of surface notches. The Pt size and dispersion significantly improved along with the increased concentration of oxygen vacancies. Moreover, plasma treatment

imposed high stability and water resistance. The nature of plasma action still requires additional studies. The relationship between plasma mode parameters and the structure-performance interplay in specific reactions should be thoroughly investigated. Particular attention can be paid to plasma-surface interactions. It is noteworthy that other plasma-based techniques (e.g., low-temperature plasma approach based on the cold hollow-cathode arc [88] or vacuum-arc plasma-assisted deposition with plasma flow filtering [89]) can be considered.

2.1. Catalyst treatment

The conditions of support and catalyst pretreatment were found crucial for the organization of the active surface and bulk catalyst structure in a number of environmental reactions catalyzed by composites utilizing Pt–CeO$_2$ interfaces. Most effects are caused by the reductive and oxidative treatments and the catalyst calcination temperature. The treatment conditions (reducing or/and oxidizing) affect the local surface atomic configurations and states of Pt and Ce. In CO oxidation, the catalyst treatment conditions controlled the sizes of Pt species and concentration of oxygen vacancies, with the latter accelerating the reaction below 150 °C due to the synergistic effects with the adjacent Pt species [64]. The Pt–O–Ce ensembles can be formed during the oxidative treatment, while under reducing conditions Pt atoms are located on the oxygen vacancies of the reduced CeO$_2$ surface [90]. Moreover, thermal stability was found a function of the number of such
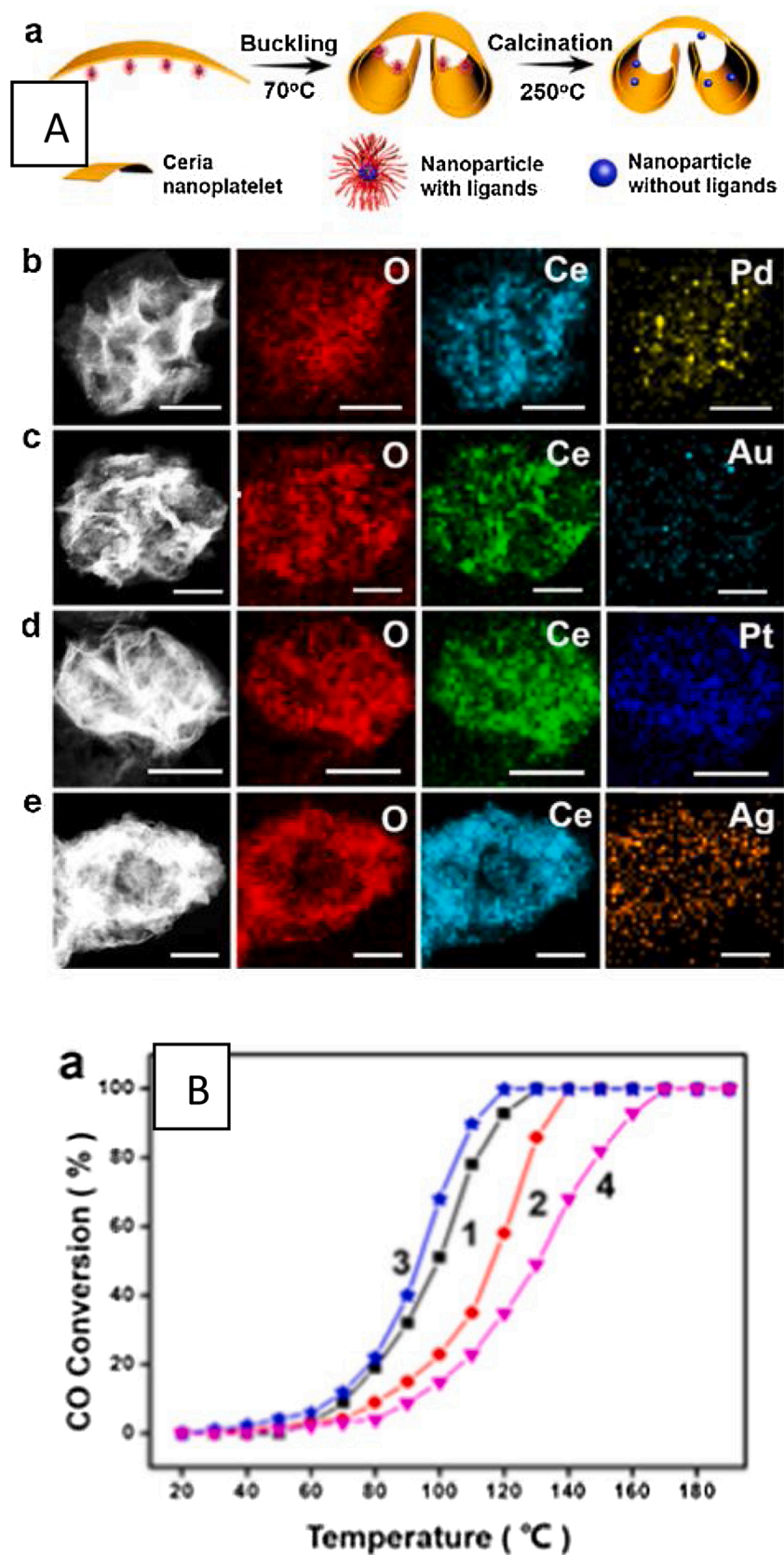
Fig. 3. (A) (a) Schematic illustration of the coassembly of ceria platelets and metal nanoparticles. (b − e) HAADF-STEM images (left panel) and EDS-STEM (right panel) of ceria platelets loaded with various metal nanoparticles: (b) Pd, (c) Au, (d) Pt, and (e) Ag. All scale bars are 100 nm. (B) Percentage conversion versus temperature plots for the oxidation nanoparticles: 1, Pd; 2, Au; 3, Pt; and 4, Ag. Reproduced with permission from Ref. [71]. Copyright American chemical society.

ensembles that were more resistant to H_2 reduction after high-temperature oxidative treatment. Under low-temperature oxidative treatment and the subsequent high-temperature calcination (up to 800 °C), only the formation of the Pt–O–Ce interactions was facilitated, while the support-bound Pt° species were not formed [91].

The reducing and oxidizing treatments were shown to be beneficial for the formation of interfacial sites with desired topological properties. Dynamic reducing/oxidizing cycles revealed the increase of ceria reducibility at elevated temperatures and upon employing stronger reducing mixtures or interaction with reduced Pt particles [92]. Higher Pt particle sizes reduced the interfacial perimeter suppressing the ceria reduction.

Below 200 °C, the closely packed Pt clusters were shown to be arranged permanently out of several pseudo-stable states of Pt on ceria, namely, sub-nanometric raft-like clusters, 3D hemispherical NPs (1–2 nm) under reducing conditions, and isolated cations under oxidizing conditions at high temperature, and an intermediate 2D monolayer was formed [139]. Both the rates of formation and redispersion of Pt NPs during the reduction were faster at 500 °C. Cycling redox treatments at different temperatures ensured the formation of ceria-supported Pt species with different sizes and shapes. The species were different in terms of oxidation degree and interactions with the support.

It is noteworthy that the temperature of oxidative decomposition of Pt precursor defines the nature, state, and size of the Pt species formed ensuring a high amount of Pt–O–Ce ensembles due to the formation of $[O_xPtCl_{6-x}]_n$ and PtO_x species on the surface or in the bulk of ceria as well as at the interfacial $Ce_{1-x}Pt_xO_{2-y}$ solid solution [99] (Fig. 4).

The partial reduction of CeO_2-based supports and metal-doped catalysts on the basis thereof generally leads to their improved features (e.g., oxygen storage and release capacity, reducibility, etc.) [140]. The mentioned effects usually result in improved activation of reaction feedstock (e.g., CO_2 [17,18]). For Pt–Ba–Ce/γ-Al_2O_3 catalysts it was shown that the extended exposure time with H_2 improved both NO_x storage efficiency and conversion [141].

The formation of the multimodal porous network in the pre-reduced Pt–CeO_2 catalyst was shown (Fig. 5) [142], where ceria nanocrystallites formed 3D aggregates and puzzle-like 2D walls separating large mesopores and macropores, while the small voids between the imperfectly assembled crystallites formed micropores. ~50 % of the Pt NPs were located within ceria. Partial reduction of Pt NPs was also achieved [96].

To sum up, the local structure of the surface of partially reduced ceria remains debating, and more surface science and theoretical studies are required to elucidate the surface atomic configurations formed, including native defects. The Pt species interacting with the ceria surface can impose a different degree of ceria reduction depending on their sizes and morphology, and this issue can be further clarified. The exact location of Pt ions in the bulk and/or on the surface of the oxidized samples remains unclear. The oxygen stoichiometry in the reduced ceria still remains debating [143]. Moreover, although most proposed theoretical models used to study this issue assume preserving the fluorite-like local structure for ceria upon doping with Pt, this seems unlikely in the case of real catalytic systems, and more realistic model conditions are required. The process and conditions (namely, temperature) of solid solution formation in the bulk and/or on the surface upon the sample reduction as well as the reversibility of such a process are also of particular interest.

2.2. Pt precursor

The nature of the precursor of the active metal component is known to influence on the catalyst performance. Usually, for Pt–CeO_2 composites, H_2PtCl_6 [98] (or its salts [144]), $Pt(NO_3)_2$ [145] precursors and $Pt(acac)_2$ [71] are used, while organometallic complexes can be employed for mono- (trimethyl (methylcyclopentadienyl) platinum(IV) ($MeCpPtMe_3$) [146] or $(EA)_2Pt(OH)_6$ [147]) and bimetallic (e.g., $[AuEn_2]_2[Pt(NO_2)_4]_3 \cdot 6H_2O$ for Au-Pt/CeO_2 catalysts [103], $[Rh(4-pic)_4Cl_2]_2[Pt(NO_3)_6]$, $[Rh(bpy)_3]_2[Pt(NO_3)_6]_3$, $[Rh(bpy)_3][Pt(NO_3)_6](NO_3)$ $(CH_3COCH_3)(CH_3CN)(H_2O)$ [148] for Rh-Pt/CeO_2 catalysts) composites. Polynuclear Pt nitrato complexes $([H_3O \subset 18\text{-crown-}6]_2[Pt_2(\mu^2-OH)_2(NO_3)_8][Pt_4(\mu^3-OH)_2(\mu^2-OH)_4(NO_3)_{10}]$ [149]) tetraalkyl ammonium salts $((Me_4N)_2[Pt_2(\mu-OH)_2(NO_3)_8]$, $(Et_4N)_2[Pt_2(\mu-OH)_2(NO_3)_8]$, $(n\text{-}Pr_4N)_2[Pt_2(\mu-OH)_2(NO_3)_8]$, $(n\text{-}Pr_4N)_2[Pt(NO_3)_6]$, and $(n\text{-}Bu_4N)_2[Pt(NO_3)_6]$ [150]) were introduced. The Pt_nO_m
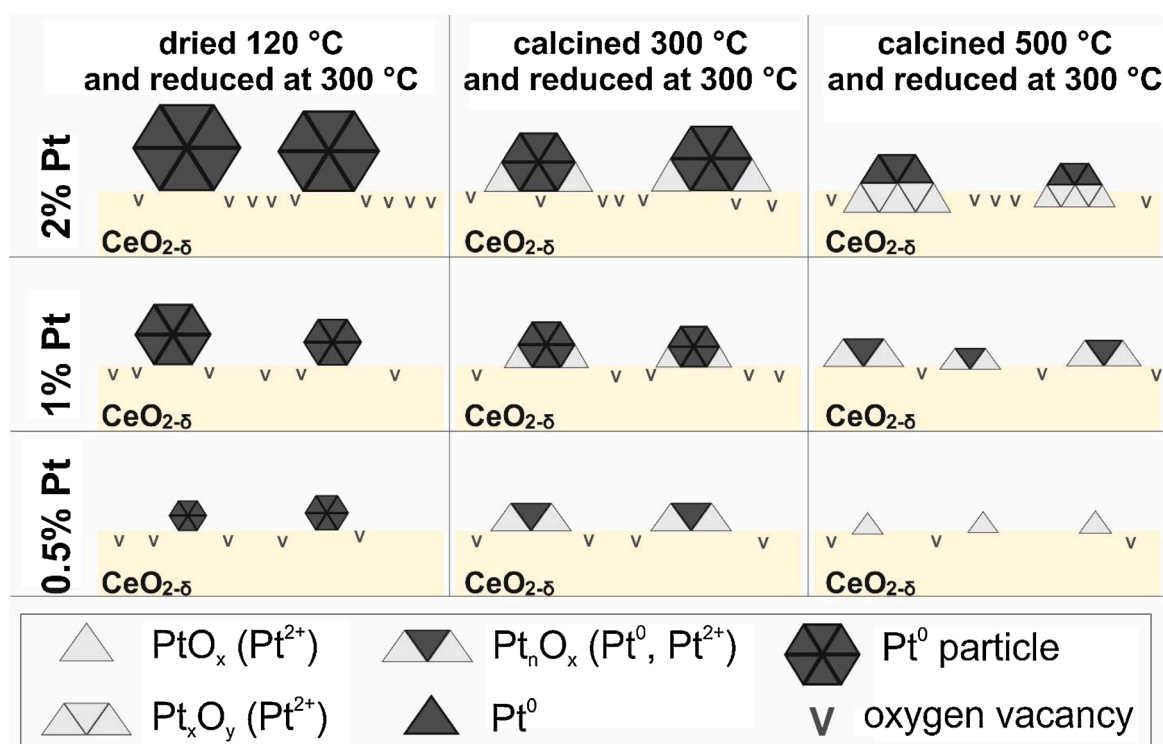

Fig. 4. A schematic representation of the oxidized and reduced samples. Reproduced with permission from Ref. [99]. Copyright Elsevier.
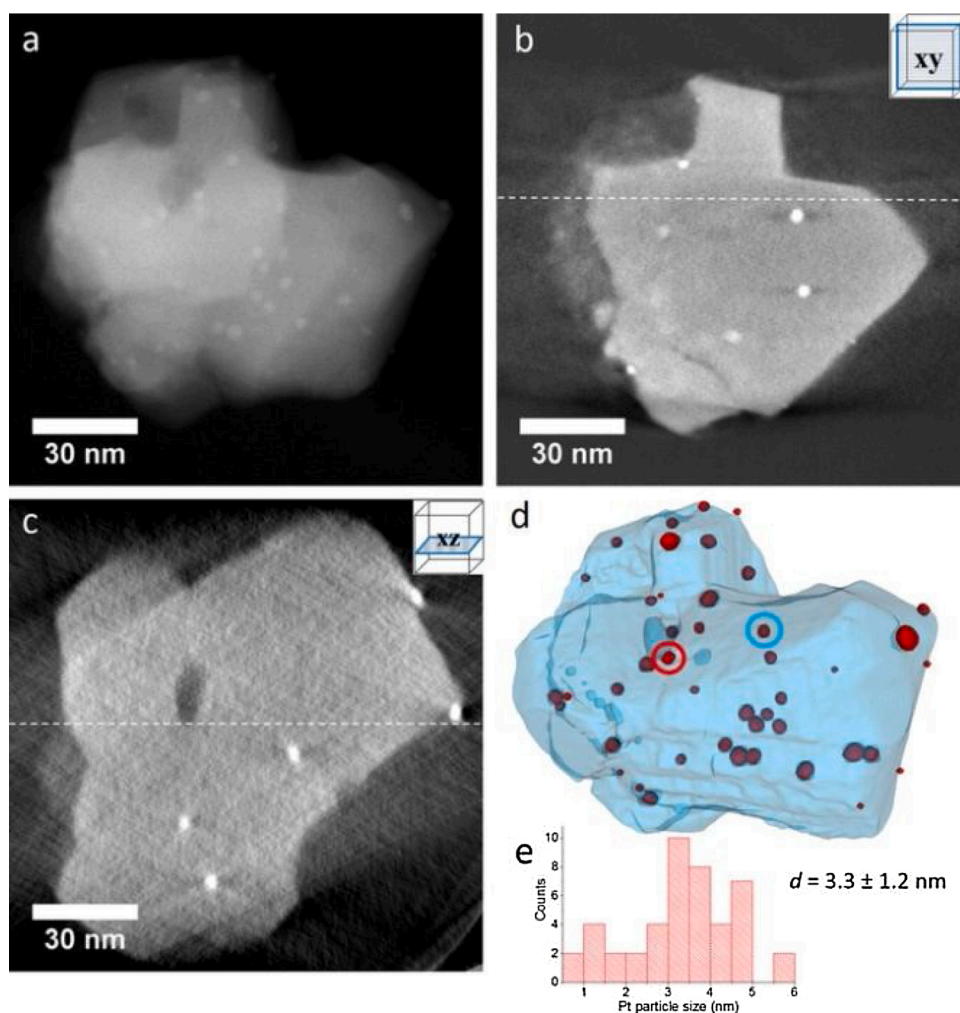
Fig. 5. STEM-HAADF tomography analysis of a ceria aggregate supporting Pt nanoparticles. a) Projection at 0°, in which the white dots correspond to Pt particles; b) cross section along the XY plane; c) cross section along the XZ plane; the dashed line shows the intersection between the two slices; d) model of the aggregate (shown in a viewing direction corresponding to that in a), with ceria and Pt represented in blue and red, respectively. The bright red particles (as the one circled in red) are located at the surface of the ceria aggregate and the dark red particles (as the one circled in blue) are buried in ceria; e) Pt particle size distribution. Reproduced with permission from Ref. [142]. Copyright Wiley. (For interpretation of the references to colour in this figure legend, the reader is referred to the web version of this article.)

clusters with low coordination number in the second shell were formed under the activation of NO$_3$-rich support in combination with thermolabile Pt precursor and determined the catalyst activity. Interestingly, different surrounding of Pt atoms in polynuclear nitrato complexes is expected to impart different behavior of the sites derived thereof. For instance, the presence of a reducing agent in the Pt(NO$_3$)$_2$(NH$_3$)$_2$ results in the formation of larger Pt particles during the calcination. Thus, detailed surface science studies are required to shed the light on the nature of functionalization of such sites and the mechanisms of formation of the corresponding Pt species. The specific roles played by the ligands can also be further clarified.

The Pt precursor can also diffuse through the preformed porous ceria film structure and then decompose only at the ceria surface to produce homogeneous Pt-doped ceria after the saturation of Pt^{2+} sites to result in the formation of metallic nanoclusters [146]. Moreover, the nature of the counter ion in the precursor salt may affect the performance also depending on the application reaction. For instance, in CO oxidation the samples derived from Cl-based precursor were found less active than those derived from NO$_3$-based precursor [98], while the opposite situation was observed in the total oxidation of alcohol [151].

Analysis of the literature shows that the composition of the Pt precursor can drastically affect the performance of the designed catalyst. In that sense, it is crucial to pay more attention to the order of component introduction as well as the procedures of their treatment during the catalyst preparation and in the course of the target environmental reaction. More efforts are required to reveal the factors causing different behavior of anionic moiety of metal precursor to making these and other impurities work in cooperation with the active metal but not as a catalyst poison blocking the active sites. The mixtures of Pt precursors with different nature and structures can be also considered to unlock the potential synergistic effects of anionic moieties. The functionalization of the catalyst surface upon decomposition of the precursor containing organic moieties and the derived structure-performance relationships should also be investigated in more details.

2.3. Ceria precursor

Although in supported metal catalysts the role of metal precursor cannot be overemphasized, the precursor of the support material can be equally important. Indeed, the selection of Ce precursor determines the features of the ceria formed, including textural, redox, and acid-base properties. For Pt/CeO$_2$ catalysts, the Ce(NO$_3$)$_3$ hydrates are the most frequently used precursors as they are available, and the catalyst synthesis procedures on the basis thereof meet the requirements on economical feasibility. Recently, the opportunities to use other Ce precursors were shown for cerium nitrate mixture with oxalate [152], cerammonium nitrate [92,153], Ce(OH)$_3$/CeO$_2$ nanorod precursor [83], cerium tetrakis (1-methoxy-2-methyl-2-propanolate) (Ce(mmp)$_4$) [146]. Cerium chloride is less often used in the preparation of ceria-based environmental catalyst [154] due to low tolerance of ceria to Cl [127] and high affinity of cerium to Cl to yield cerium oxychlorides and Cl effect on the morphology of the ceria formed. It is noteworthy that commercial ceria is frequently used to prepare the Pt/CeO$_2$ catalysts or promote Pt-based catalysts supported on other oxide materials. The role of oxalate [152] was connected with the formation of void

spaces upon the slow release of gases during its thermal decomposition.

Physical methods of CeO_2 production such as pulsed laser ablation from liquids for Ce target [76] are also used. The Ce precursor can also be involved in the formation of the porous structure of the support as well as surface oxygen vacancies that were shown for the Pt-doped CeO_2 thin films prepared by direct liquid injection chemical vapor deposition (DLI-CVD) technique.

Recently, metal-organic framework (MOF)-derived ceria-supported Pt catalysts were prepared by pyrolysis of as-synthesized Ce-benzene tricarboxylate (Ce-BTC) or Pt@Ce-BTC [155] and ultrafast laser processing of Pt-encapsulated cerous metal–organic framework (Ce-MOFs) to obtain 2-nm Pt NPs on defective 5-nm CeO_2 NPs [156] (Fig. 6). The benefits are imposed by the MOF-derived hierarchical structures retaining MOF morphology while preventing migration and aggregation of the Pt NPs along with their uniform distribution within the ceria matrix. Moreover, the obtained composites demonstrate rather high stability in the oxidation of CO and toluene. However, the effects caused by the high-energy treatments on the surface features and states of both Ce and Pt should be further clarified. The activity response to changing parameters of treatment procedures can be also revealed. Recently, the effect of structural isomerism was revealed in Ce-BTC MOF [157], and Pt NPs were loaded on two topologically different Ce-BTC featuring the same ligands and metal sites. Tetragonal Ce-BTC framework irreversibly transformed to monoclinic isomer upon water soaking treatment. The Pt/CeO_2 composite derived from tetragonal Ce-BTC featured a higher amount of Pt0 and smaller Pt NPs to ensure high CO oxidation activity.

The Pt@CeBDC MOF was used to prepare the 1D nanostructure of Pt@CeO_2−BDC catalyst for toluene oxidation [158], with 2-nm Pt clusters being located on the polycrystalline ceria. The composite feature increased number of oxygen vacancies. Fig. 7 shows the schematic of Pt@CeO_2−BDC formation as well as the morphology of the obtained samples. The peculiarities of the catalyst surface allow changing of the reaction mechanism from the Langmuir-Hinshelwood mechanism at low temperatures to the Mars-van Krevelen one as the temperature increases.

The functionalized MOFs were shown to demonstrate improved performance. Thus, the highly dispersed Pt particles with sizes below 1.5 nm were formed over mesoporous ceria due to the coordination of Pt ions with amino groups in NH_2-Ce-MOFs [159]. The NH_2 groups facilitated the formation of Pt-CeO_2 interfacial sites (including the surface peroxo species) during the Ce-BDC transformation to CeO_2. However, the exact mechanism of NH_2 contribution can be further clarified.

Thus, the Ce precursor is no less important than the Pt one, since it affects the structural and textural properties of the ceria formed during the catalyst preparation. At the same time, there is a lack of information on the mechanisms of transformation of Ce precursors (especially, for the case of MOF-derived composites) into CeO_2 with the desired features, while understanding of these regularities can be used in purposeful design and synthesis of ceria supports. The role of functionalization of Ce-based MOFs on dispersion and stability of Pt

species can also be thoroughly investigated. The nature and structure of the formed surface CeO_x complexes existing in the proximity with Pt species also remain poorly described.

The overview of the literature in the field of preparation of Pt–CeO_2 composites by both chemical and physical methods shows that different approaches exist to control the Pt size and state, catalyst morphology, MSI, and other factors that show a significant effect on their catalytic performance. The treatment conditions (temperature and atmosphere) play important roles in the formation of ceria-bound Pt species. The features of catalyst preparation influence on the catalytic properties in such important environmental processes as CO oxidation, VOCs abatement, reduction of nitroaromatic compounds, and dry reforming of methane.

3. Pt-related factors

Usually, Pt is the active component of Pt/CeO_2 catalysts, while in minor catalyst formulations (e.g., ceria-supported Ni-based DRM catalysts) it rather acts as a promoter. Several Pt-related factors significantly affect the performance of such catalysts in environmental applications. Among these factors are size, shape, dispersion, and the state of Pt. The Pt precursor is of profound importance to obtaining Pt species with desired features.

3.1. Pt size and shape

For supported metal catalysts, the size of metal moiety usually plays a crucial role in the catalyst performance. The environmental Pt/CeO_2 catalysts for various processes feature the Pt size effect, and three main types of species usually coexist: (1) isolated single-atom Pt species, (2) Pt nanoclusters, and (3) Pt nanoparticles. The sizes of single-atom species, clusters, and nanoparticles can be ranged around 0.1 nm, 1−5 nm, and above 5 nm, respectively [160]. Not only do these species differ in intrinsic activity, but also in selectivity and physical-mechanical properties (especially, catalyst stability), and exarticulation of their performance in terms of activity and/or selectivity is a challenging task.

The size and shape of Pt species interacting with ceria support contribute to such important features as interfacial perimeter length [161], charge transfer, the chemical composition of the interface, and the strength of the metal–support interface. At the final end, these features affect the binding energies of the substrates, the potential number of molecules that can be bound and converted by such surface, and the mechanisms of the reactions considered. It is noteworthy that even if one prepares the single-atom Pt–CeO_2 catalyst, it is not in every instance that such a catalyst will exhibit higher activity in a certain reaction as compared to the counterparts based on Pt clusters or larger nanoparticles (Table 1). While cooperation of the single-atom sites closely located on the catalyst surface provides the enhanced catalyst performance, still such systems suffer from the impact of reactive atmospheres, and the approaches providing the precise design of such composites with
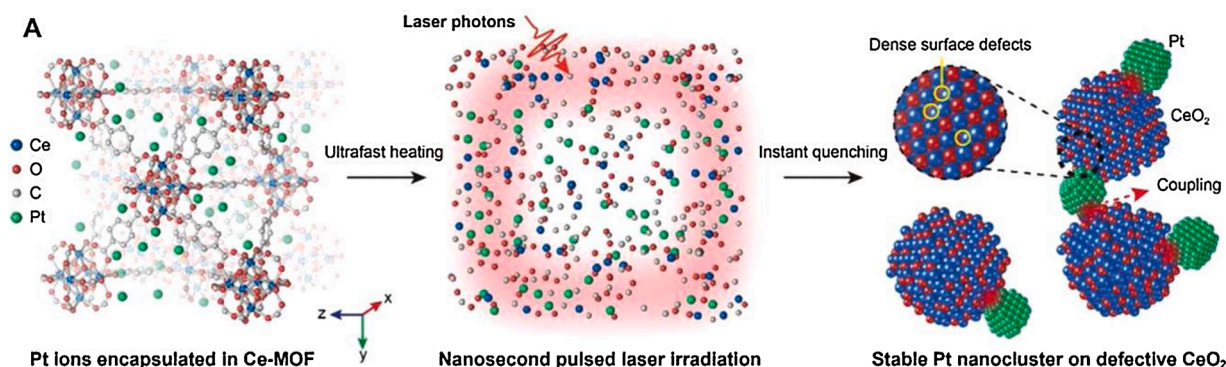

Fig. 6. Schematic of the laser-induced formation of defective CeO_2 supported Pt nanoclusters. Reproduced with permission from Ref. [156]. Copyright Wiley-VCH.
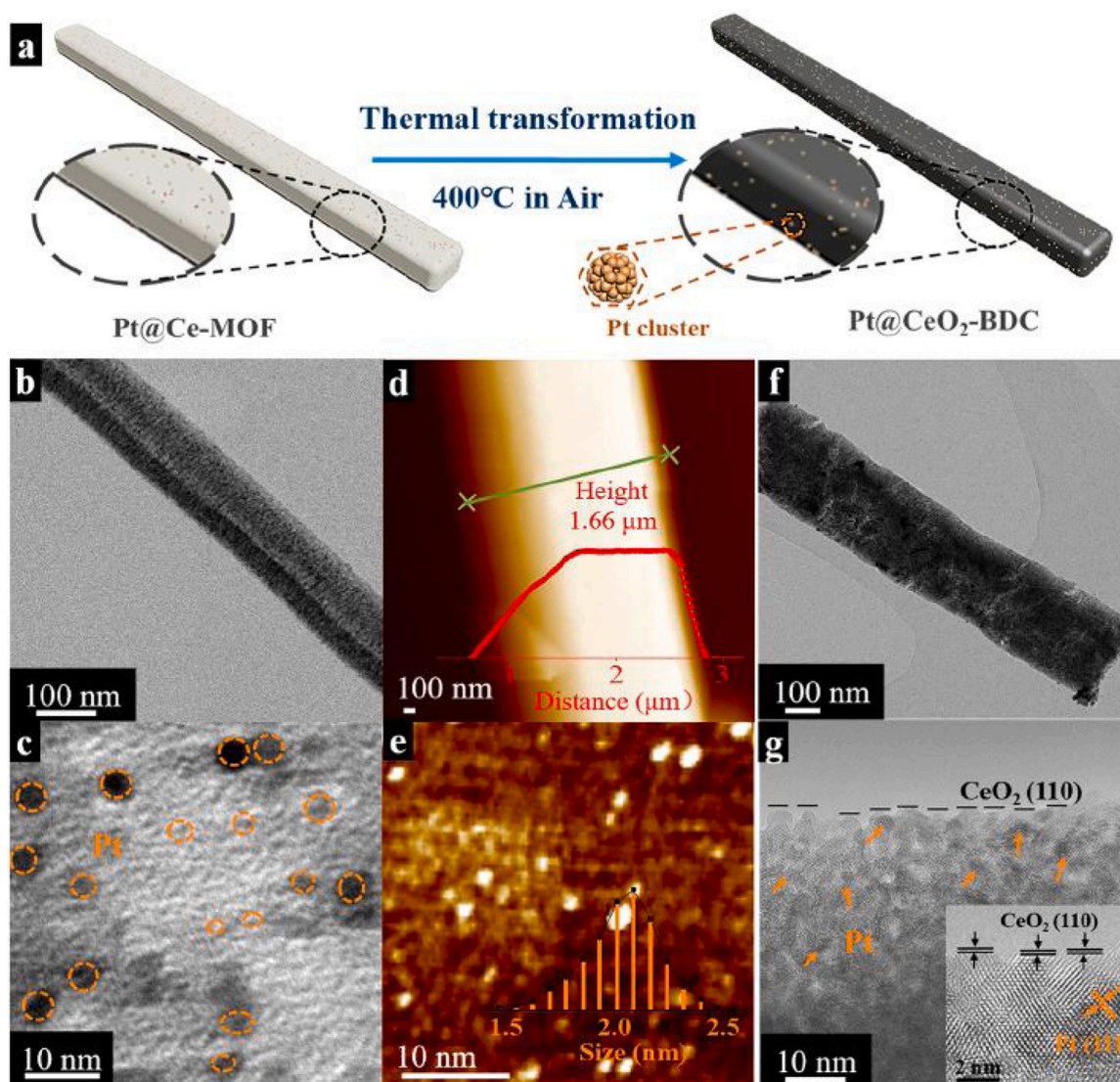
Fig. 7. (a) Schematic drawing of Pt@CeBDC transformation into Pt@CeO$_2$−BDC during heat treatment in air. (b and c) TEM micrographs of Pt@CeBDC MOF showing (b) the morphology, and (c) deposited Pt clusters. (d and e) Atomic force microscope image of Pt@CeBDC MOF showing (d) the morphology with an inset of the cross-section profile, and (e) Pt clusters on the surface with an inset of Pt cluster size distribution. (f and g) TEM micrographs of Pt@CeO$_2$−BDC derived from Pt@CeBDC MOF displaying (f) the morphology, and (g) Pt clusters (indicated by arrows) and mesoporosity with a high magnification inset revealing atomic details of a Pt cluster and CeO$_2$. Reproduced with permission from Ref. [158]. Copyright American chemical society.

a given size, morphology, and stability remains challenging.

3.1.1. Single-atom Pt

Recently, an interest arose in the isolated single-atom configurations (Fig. 1) that could ensure high catalyst activity along with high Pt efficiency [162]. Fig. 8 shows the typical HAADF-STEM images of the single-atom Pt/CeO$_2$ catalysts and those utilizing Pt clusters.

Single-atom environmental Pt/CeO$_2$ catalysts were prepared by a number of techniques, including atomic layer deposition (ALD) [163, 164], high-temperature vapor-phase atom trapping [165,166] as well as more traditional and less resource-consuming wet impregnation [167, 128] and coprecipitation [168,169] techniques. Small Pt loadings usually ensure high dispersion of Pt species, if appropriate catalyst pretreatment conditions are employed. Among such conditions are the temperature of reduction under hydrogen atmosphere [74,145], calcination temperature for the support or/and catalyst [99,169], high-temperature steam treatment [97], and their combinations. Atomic size and homogeneous distribution impose enhanced reactivity of the Pt$_1$ species caused by their electronic structure. In particular, the

increased low-temperature CO oxidation activity and high hydrothermal stability were achieved by steam treatment activation at 750 °C of atomically dispersed ionic Pt supported on the thermally stable ceria to organize a new type of active sites in the proximity of Pt^{2+} species stable up to 800 °C under oxidizing environments [97].

Although physical approaches provide the opportunity to "put" the Pt atoms into the "right" position on the ceria surface, still they are rather expensive and require advanced equipment as compared to traditional approaches. At the same time, conventional techniques are more relevant to industrial catalyst preparation methods, while their limitations make the performance of single-atom configuration less efficient. Thus, it is of importance to develop a balanced approach to the preparation of the single-atom catalysts that collocate the advantages of the abovementioned approaches. The recently developed approaches to synthesize single-atom Pt species utilizing the MOF-derived ceria sources (e.g., [156]) can be considered promising for the production of new generations of environmental Pt/CeO$_2$ catalysts.

Since the small Pt loadings are usually used in single-atom catalysts, the most experimental techniques cannot detect and characterize the
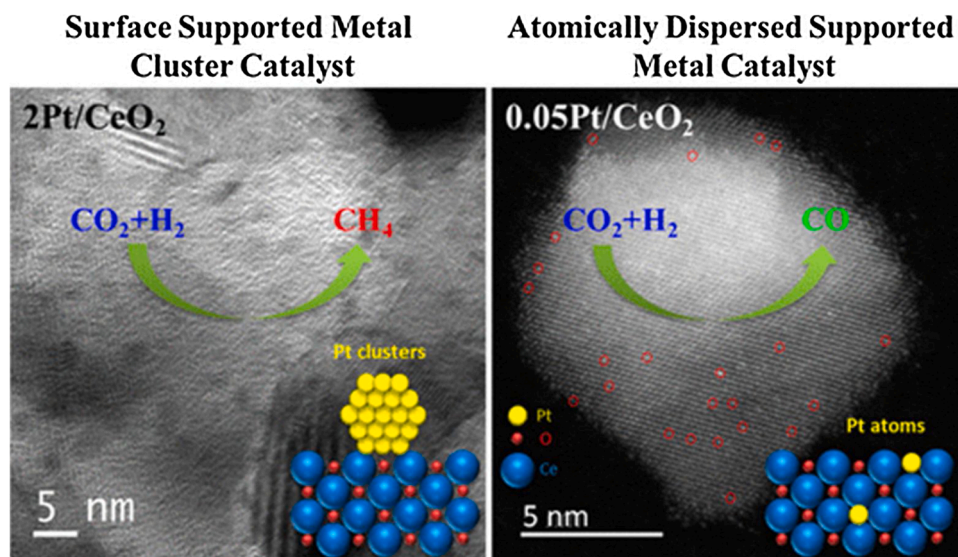
Fig. 8. Structural morphology for surface supported Pt cluster and atomically dispersed supported Pt catalysts. Reproduced with permission from Ref. [61]. Copyright American Chemical Society.

nature and behavior of surface Pt species. Theoretical approaches became helpful to provide new insights into the state of active surface sites and overcome the limitations of the experimental techniques in the characterization of materials and reactions related to environmental catalysis. The Pt–CeO$_2$ interfaces, including single-atom configurations, are actively studied with theoretical methods [e.g., 170,171], and those approaches usually employed for metal-doped ceria (e.g., Cu/CeO$_2$ [43], Ag/CeO$_2$ [172]) are in use. Correct calculation and interpretation of cerium states and ceria surface species as well as proper selection of calculation methods are considered. Currently, hybrid functionals and the DFT + U approach are actively used [173].

Among the key research directions for environmental single-atom

Pt/CeO$_2$ catalysts is the revealing of the nature of stability of Pt species towards coalescence to clusters, agglomeration to NPs, and subsequent sintering. The approach to determine the thermodynamic stability of ceria-supported single-atom and nanoparticle platinum in the presence of substrates at the given conditions was proposed [174]. The Pt doping to (111) ceria surface provided high CO oxidation turnover rate due to the strong CO binding to single-atom Pt species over stoichiometric ceria or Pt$_1$O over step-edge sites (Fig. 9). High Pt-O-Ce distortion was obtained for Pt$_1$-CeO$_2$(100) [175] and was considered the reason for improved thermal stability along with the enhanced adsorption capacity towards O-containing substrates.

The substitution of lattice Ce ions by single-atom Pt species was
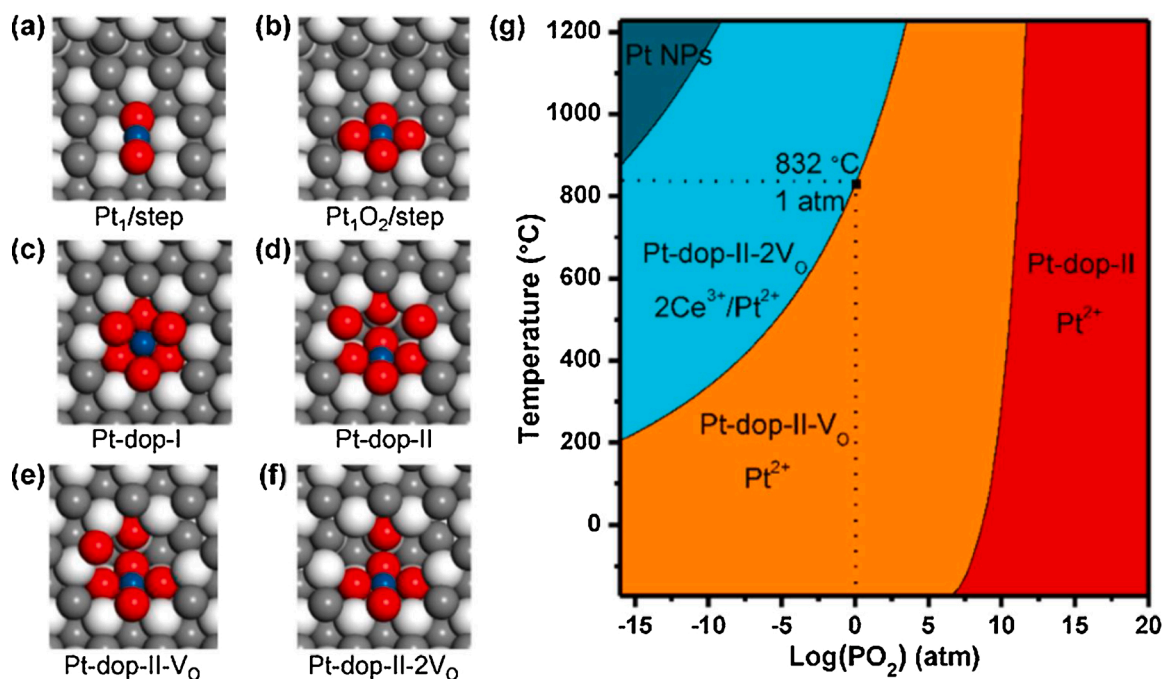
Fig. 9. Pt SAs located at a CeO$_2$(111) step before (a) and after (b) O$_2$ dissociation, and (c − f) doped into the CeO$_2$(111) surface (color code: white, Ce; gray, irrelevant O; red, relevant O; black, C; blue, Pt). (g) Ab initio-determined phase diagram of the Pt-doped CeO$_2$(111) surface. Reproduced with permission from Ref. [174]. Copyright American Chemical Society. (For interpretation of the references to colour in this figure legend, the reader is referred to the web version of this article.)

shown to be thermodynamically stable [176], and the species were found to be the electron donor/acceptor in the redox processes. Oppositely, the Pt_1 species were also found unstable [177] and preferably substituted Ce atoms rather than were attached to the $CeO_2(111)$ surface. Recently, it was also reported [164] that the stability of single-atom Pt_1/CeO_2 catalyst with nanorod morphology can be tuned by the ceria defect sites, metal loadings, and high-temperature calcination at 600 °C. The ceria-supported single-atom Pt species predominantly existed as Pt^{2+} state at the defect and step edge sites, while Pt^{4+} states were formed on terrace sites.

Nevertheless, despite thorough discussion, the stability of the single-atom Pt/CeO_2 catalysts remains a debating issue, and the synthetic approaches that can improve this parameter are of particular interest. The range of parameters that can affect the stability should be widened, and their relationships can be further modeled.

The surrounding of the single-atom Pt species ensuring their coordination is also of particular importance. Lattice distortion caused by the electronic structure of the dopant affected the Pt segregation [178], with the O vacancies forming at the segregated surface in the vicinity of the interfacial Pt atom. The formation of grain boundaries near the nanocrystalline ceria surfaces resulted in Pt trapping out of the grains that suppressed their accumulation on the surface under O-lean conditions. Six oxygen atoms coordinated with the Pt_1 site [177]. The square-planar structure was also found preferable when a single oxygen vacancy was created [179]. The model comprising Pt-passivated ceria (100) surface, where Pt atoms occupied hollow sites and coordinated with four oxygen atoms, adequately described the Pt charge states in the single-atom catalysts [168]. Metal dispersion in the form of single atoms on the O_4 ceria sites was energetically favorable for the formation of metal NPs [170] to result in rather stable sintering-resistant adsorption complexes on the nanoparticulate oxide. For the row of M-doped (M = Pt, Pd, Ni, Cu) ceria NPs, the energetics of the surface reactions was shown to be controlled by both surface position and coordination of dopants. The Ce^{4+} substitution by Pt was favorable for bulk positions within the unreduced ceria NPs. In the most stable surface position, Pt was agglomeration-resistant and featured high dispersion [180,181].

Another crucial point is the "optimal" distances between the isolated single-atom species and/or surface defects and/or promoters/modifiers on the support surface. Indeed, if the Pt atoms are too distant from or too close to each other, there can be a place for processes leading to nonselective transformations that include but are not limited to (1) formation of the large surface area not covered with active Pt species, (2) complete coverage of the Pt species by several substrate molecules and/or products of their conversion, (3) rearrangement of the surface defects that is crucial for those processes where ceria and Pt activate different reagents (e.g., CO_2 conversion [61], tandem catalytic reactions [182]), (4) close proximity (<1.5 nm) of Pt atoms resulting in multi-atom ensembles that compete with the single-atom configurations in activity (and it is difficult to exarticulate the own activities of single-atom species and such ensembles). Thus, the development of synthesis strategies that allow a homogeneous distribution of single-atom Pt species accompanied by the organization of the tailor-made surface defects is still challenging.

The Pt size dependence of the catalyst performance was shown for Pt/CeO_2 catalysts in several environmental reactions. For instance, for selective hydrogenation of p-chloronitrobenzene (p-CAN) [128], the selectivity towards p-CAN featured a volcano-type dependence on the Pt loading. At Pt loadings of 3 wt%, the p-CAN selectivity decreased simbasically with the Pt particle size. The reverse selectivity increase was observed during the subsequent reduction of the Pt loading. Both 0.3 % Pt/CeO_2-SAC and 0.6 % Pt/CeO_2-SAC catalysts featuring atomically dispersed Pt exhibited ~100 % selectivity to p-CAN under these conditions. The latter sample possessed a superior activity implying 100 % atom utilization efficiency that could be obtained over this single-atom catalyst. Electrostatic repulsion between the nonbonding Cl orbitals and predominant Pt orbitals with steric hindrance suppressed the dehalogenation.

The superior performance of single-atom configuration as compared to Pt clusters was also demonstrated for Pt/CeO_2 catalysts for CO_2 reduction [61]. The 0.05 wt%Pt/CeO_2 catalysts showed a 7.2 times higher CO_2 reduction rate as compared to nanoclustered counterparts. Thermal stability was observed at 500 °C. Ceria activated CO_2 molecule, while Pt contributed to H_2 dissociation. Single-atom configuration allowed restricting hydrogenation reactions and preventing CO poisoning. Fig. 10 shows the difference in the reaction mechanisms for single-atom and cluster configurations.

The relationship between Pt dispersion and catalyst reactivity was also considered for CO oxidation and was clearly observed at high CO concentrations in the feed [100]. The low and high CO concentrations were converted on the active sites with low and high activation energy. High Pt dispersion was assumed to compensate high activation energy of the catalyst.

When discussing the activity of the single-atom Pt species it is also necessary to bear in mind that in real catalysts these species can coexist with larger Pt aggregates (i.e., clusters and/or particles), and accounting for their combined effects is rather important to receive new insights on the mechanism that facilitate dispersion or prevent sintering and aggregation and ensure higher catalyst stability. These crucial issues can be clarified by applying precise surface models in combination with advanced surface science techniques (e.g., EXAFS, XANES, HAADF-STEM, aberration-corrected scanning transmission electron microscopy (AC-STEM), high-pressure scanning tunneling microscopy (HP-STM), etc.).

3.1.2. Pt clusters

Contrary to the single-atom species, Pt clusters feature a larger number of atoms that impose different properties, in particular, the more metallic nature of the adsorbed Pt species. The diverse cluster structures demonstrating different performance can be formed for an equal number of Pt atoms, and such a performance becomes a function of structural peculiarities, order, and coordination of Pt atoms in the cluster. The particle–support interfacial perimeter length also becomes higher in the case of clusters. When Pt exists in cluster states, it tends to feature a positive charge. The modern preparation techniques do not allow synthesizing the ceria-supported Pt clusters with the given number and arrangement of atoms. Moreover, the organization of such clusters on the ceria surface is also challenging since the compatible defect structure should be organized as well.

The Pt clusters were studied both experimentally and theoretically. Recently, particular attention was given to growth trends of Pt clusters [183], cluster reactivity in NO adsorption and reduction [184], CO adsorption and oxidation [101,185,186] as well as strong MSI [183,187, 188].

The growth trends and morphology evolution for the Pt cluster remain debating. For Pt_N clusters (N = 1–10) supported on $CeO_2(111)$, the 2D planar structures were formed up to Pt_8, while 3D clusters were formed further [183]. The $CeO_2(111)$-supported Pt_n (n = 5–13) clusters formed a 2D morphology for n = 5 and a 3D morphology for n≥6, with the 3D tri-layer structure formed when n≥10 [187]. The relative fraction of the clusters per each morphology type was estimated. For $Pt_n/CeO_2(111)$ (n = 3–6), the metal–support interface and cluster morphology was shown to determine the charge transfer, cluster binding with the substrate, and the degree of ceria reducibility [188]. Reverse O spillover changed from highly endothermic to exothermic. Ceria-supported Pt_6 clusters were found resistant to sintering.

The reactivity of the PtO_x clusters over Pt_4O_x clusters and single Pt atom (Pt_1O_x) supported on CeO_2 (110) model surface was discussed in CO oxidation reaction [101]. CO adsorption decreased as the amount of coordinated oxygen increased. The interfacial oxygen of PtO_x facilitated the CO_2 formation.

It is noteworthy that the shape and morphology of Pt clusters are greatly affected by the state of the support surface and can be
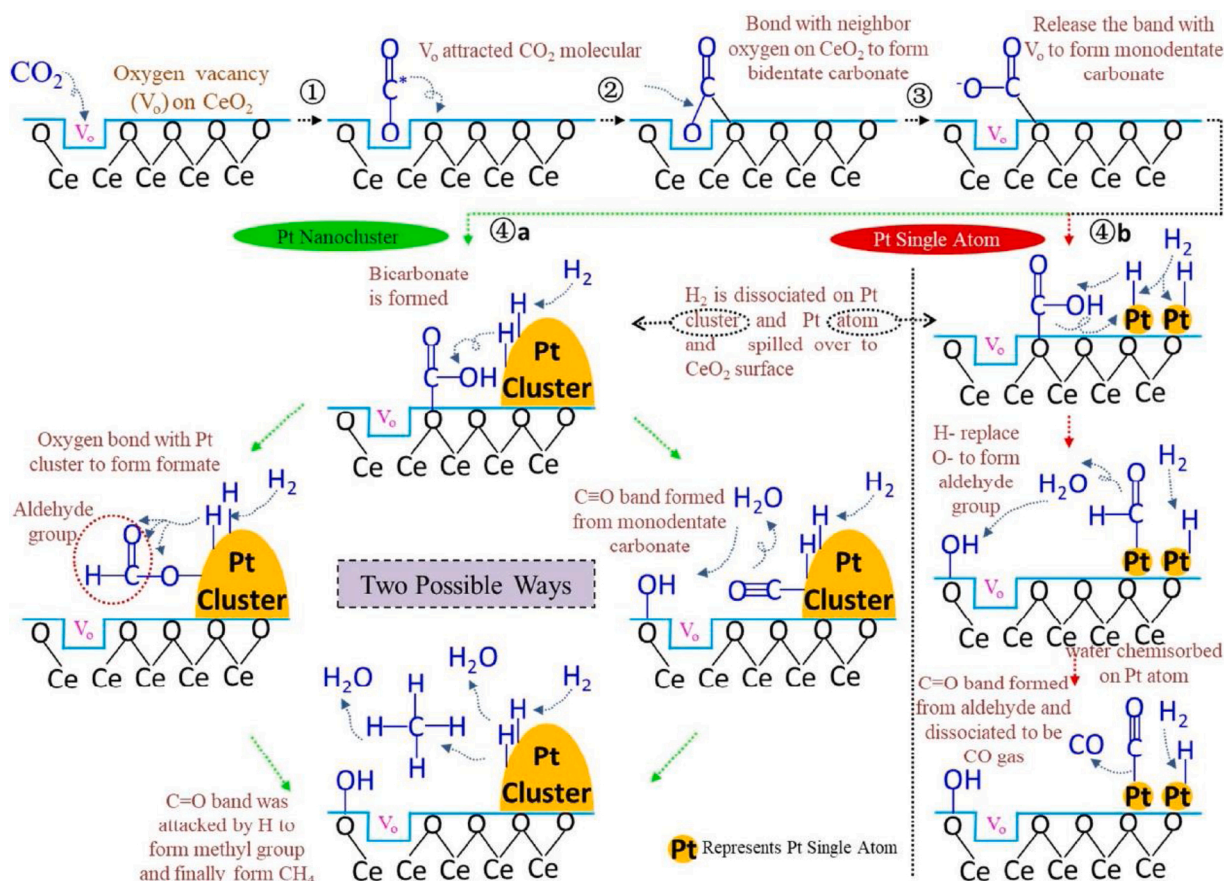
Fig. 10. Proposed reaction mechanism on Pt/CeO2. Illustration of reaction mechanism of 2 Pt/CeO2 (pathway 4a) and 0.05 Pt/CeO2 (pathway 4b) for CO2 reduction. Reproduced with permission from Ref. [61]. Copyright American Chemical Society.

additionally tuned by other catalyst components. The support features surface defects (i.e., oxygen vacancies, steps, and other point defects) that generally behave as active sites. Such defect structure can be organized at the stages of catalyst preparation and/or treatment as well as upon the catalyst interaction with the reaction reagents, intermediates or products. Thus, the particular mechanisms of Pt cluster nucleation and growth on specific support surfaces should be revealed given the peculiarities of the surface arrangement of atoms in the support and cooperative action of surface defects in these processes.

Substrate binding was shown to affect both structure and stability of small Pt clusters over $CeO_2(111)$. Thus, CO coverage resulted in the decomposition of Pt clusters to Pt, $Pt^0(CO)$, and/or $Pt^{2+}(CO)_2$ species, with the first two processes being endothermic and energy neutral, respectively [185,186]. The latter species were formed if the support comprised small ceria NP providing low-coordinated O sites and reducible Ce^{4+} sites. High CO coverage depleted the occupied 5d PDOS close to the Fermi level and appearance of new states. The d-band center in all systems shifted to lower energies indicating the reduction of Pt reactivity upon CO adsorption, with linear CO adsorption to a single Pt atom as well as bridge adsorption between two Pt atoms for larger systems being the most stable adsorption sites.

Few efforts were given to understanding the Pt cluster segregation and coalescence. The activation energies for these processes in the air reflected strong Pt anchoring on ceria under reducing atmosphere [189]. The cluster became mobile only above 900 °C. Thermal treatment conditions determined the nature of the segregated Pt particles. The $Ce_{21}O_{42}$-supported mononuclear Pt species and their stability upon reduction or oxidation were described [179], with $Pt^{2+}/CeO_2(100)$ being the most stable system found. For the case of mononuclear Pt species at $CeO_2(111)$, the exothermic agglomeration of Pt clusters was proposed.

Although many informative and reliable models were proposed to reflect the $Pt–CeO_2$ interactions and their roles in catalytic conversion of various VOCs, the main drawbacks of such models are connected with the fact that they represent the "gas phase" interaction of Pt and ceria moieties, while many physical phenomena arising from the interaction of Pt atoms and clusters with ceria surface are not considered. In particular, the restructuring of ceria surface induced by "immersion" of Pt adatoms or clusters is usually poorly discussed, while accounting for such a phenomenon would allow describing in more details the charge transfer processes and the features of the interfacial perimeter. It is also noteworthy that the adsorbate-induced restructuring of Pt species depends on the size of the adsorbate molecule and is usually not taken into account.

3.1.3. Pt nanoparticles

Contrary to single-atom and cluster configurations, the Pt NPs feature a more metallic nature, high impact of bulk properties, the facets consisting of a larger number of atoms, and collective effects of coordinated atoms. The mass and size of the NP are much higher implying the opportunities for the Pt/CeO_2 system to feature several types of MSI effects. Large Pt NPs can possess many geometries, atomic coordination of grains, and defects. These aspects can contribute to the overall catalyst performance, while it is still challenging to exarticulate the effects originating from different moieties. Different Pt content in NP, cluster, and single-atom configurations also imposes the difference in the intrinsic activity of the species as well as different Pt metal efficiency. At the same time, in the case of large nanoparticles, reduced catalytic activity can be observed that can be connected with the lower free surface energy and more ordered structure of the NPs [190]. The crucial role of

the metal NPs in CeO_2 reduction was also proposed [191], with the high effect being achieved over bimetallic $Au_{0.8}Pt_{0.2}$ NPs. The charge transfer effect from the NPs to ceria was observed similar to the case of ceria-supported metal clusters [192]. The different electronegativity of Pt NPs and oxygen atoms in ceria was assumed to be the reason for such processes.

The Pt NP size effects were shown in Pt/CeO_2 catalysts for several reactions. In particular, in toluene oxidation [115], the Pt NPs (1.3–2.5 nm) facilitated the ceria reducibility and the formation of surface oxygen vacancies, with the latter being shape-dependent and controlling the reaction rate. Simultaneously, more Pt–O–Ce bonds and Ce^{3+} species were formed. The Pt particle size contributed to the reaction rate, and complete conversion was achieved in the presence of water vapors.

The aggregation of Pt particles was considered. Thus, the interparticle coarsening of ceria-embedded or -loaded Pt particles at elevated temperatures was discussed, with significant suppression of migration and coalescence of Pt NPs taking place in the embedded structures up to 450 °C [129]. The conversion efficiency of p-nitrophenol with $NaBH_4$ was >70 %, with the 7.8-time activity increase as compared with the commercial Pt/C system being observed. The aggregation and formation of Pt NPs were shown to mostly occur over $CeO_2(111)$ surface [193] (in a row of (100), (110), and (111) surfaces).

The growth of Pt NPs during the catalyst aging also caused attention. Thus, for the aged diesel oxidation catalyst, the origin of anomalous growth of Pt particles imposed by accelerated catalyst aging was connected with the vapor-phase PtO_2 transport under oxidizing conditions [194], with ceria being capable of trapping the Pt ions to suppress such transport.

Recently, to improve the high-temperature stability of the Pt/CeO_2 catalysts and to suppress the agglomeration and migration of supported NPs during the CO oxidation, the $Pt/CeO_2/NiAl_2O_4/Al_2O_3@SiO_2$ composite was fabricated [195]. The stability of microstructure up to 1000 °C was shown to be caused by the "confinement" effects related to energy traps.

Despite thorough investigation, the catalytic performance of the ceria-supported Pt NPs can be further developed in more details. In particular, the mechanisms of particle sintering, restructuring or rearrangement on the surface should be additionally studied. Currently, it is not unambiguous how and why the processes of particle agglomeration, coalescence, sintering, restructuring, and rearrangement occur on the catalyst surface. Among the opened questions are also the mechanisms of formation of Pt species on the defect-rich ceria surface, where the surface can behave as a template for nucleation and growth of Pt component. The "optimal" size of Pt species also remains debating. Understanding such phenomena will allow preparing the catalyst with the desired features. Moreover, the intrinsic catalyst activity calculated per Pt loading is often omitted, while the observed catalyst performance is assigned to the whole catalyst. Shape-dependent behavior of CeO_2-supported Pt NPs can also be elaborated given the ceria facet defects.

3.2. Pt state

The states of Pt in the Pt/CeO_2 catalysts are actively discussed. Basically, three main Pt states are considered, namely, Pt^0, Pt^{2+}, and Pt^{4+}. The Pt^{2+} and Pt^{4+} can be formed due to the distortion of the ceria surface to become dominating species localized in the single-atom state or as ceria-supported PtO_x clusters controlling the redox properties of the catalysts, with the former species showing higher stability [169]. The Pt^{2+} species is usually four-coordinated. Although Pt^{4+} species can be organized on the ceria surface, it is usually reduced into Pt^{2+} species upon calcination. The coexistence of monodispersed Pt^{2+} and $Pt^{\delta+}$ species along with metal Pt clusters occurred at the step edges [196]. Reduction of surface O concentration or increasing in the Pt loading hindered the Pt–O charge transfer while facilitating the Pt–Ce charge transfer (Fig. 11).

For the single-atom CO oxidation catalyst, the Pt oxidation state was

shown to be different over different terminations. For the cases of (111) and (100) planes, the Pt^{4+} oxidation state existed due to Ce^{4+} substitution, and a planar Pt^{2+} state was formed over (110) grains through the spontaneous formation of the surface peroxide species [176,197].

It is noteworthy that oxidized $Pt^{\delta+}$ states can be formed on the surface $PtCeO_x$ solid solutions and/or PtO_x clusters [76] in the catalysts prepared using pulsed laser ablation (PLA) in alcohol and water media. The roles of the Pt^0 and partially oxidized $Pt^{\delta+}$ species in CO oxidation were differentiated, and the species were active in low- and high-temperature processes, respectively [198]. A higher fraction of partially oxidized Pt species also ensured high Pt dispersion and improved catalyst activity.

For Pt/Al_2O_3- and Pt/CeO_2-based CO oxidation catalysts, the Pt oxidation state correlated with the ceria redox features, and slight sintering of the Pt particles was favorable for the formation of the Pt–ceria interface. Spatially resolved operando high energy resolution fluorescence detected X-ray absorption near edge structure (HERFD-XANES) technique coupled with CO concentration gradient profiles along the catalyst bed showed the importance of the Pt–CeO_2 perimeter sites that overcame the CO self-inhibition effect at low temperatures [199] (Fig. 12).

Most recently, the effect of Pt loading on the Pt state and derived low-temperature CO oxidation activity was demonstrated [200]. The high Pt content was expressed as dispersed Pt^{2+} and Pt^{4+} states that facilitated the oxygen release and reduced the light-off temperature. The 8%wt and 20 %wt Pt samples were active below 0 °C, while the one with 1%wt Pt content was active only above 100 °C (Fig. 13). The low-temperature activity was caused by the impact of O_2 and CO molecules weakly adsorbed on PtO_x sites.

At the same time, to determine the exact state of Pt species one should not rely only on the C—O vibrational frequencies [201], and a complex of modern physical-chemical studies and advanced theoretical approaches should be used. The nature of the partially oxidized Pt species can be additionally studied to reveal the degree of oxidation that is "optimal" for specific reactions.

4. Ceria-related factors: morphology effect

In Pt/CeO_2 catalysts, ceria is usually used as a support, while in some applications it rather performs as a promoter or modifier. It is noteworthy that ceria is not inert to the components of the environmental catalytic reactions due to the developed surface area and defect structure as well as the presence of the reactive surface species. The literature overview allows highlighting the following recent ceria-related factors in Pt/CeO_2 systems: (1) ceria precursor, (2) morphology of ceria particles, including facet-dependent performance.

The morphology–performance relationship of ceria was considered in several environmental catalytic reactions and energy applications [202]. A number of ceria morphologies were detected, including open-ended ceria hollow fibers [203], rod [72,204], cube [66,205], octahedral [102], highly porous CeO_2 hollow sphere [69], disk-like [131], microsized mesoporous ceria [205], nanobelts (as a component of 2 wt%$Pt/CeO_2/Bi_2WO_6$ composite) [206], etc.

In several environmental reactions, the nanorod-based samples demonstrated superior performance. For CO oxidation, the Pt catalysts supported on nanorod-based ceria were found more active as compared to nanocube and nanooctahedral morphologies due to the formation of surface carbonate species with low stability at the reactive planes of nanorods (Fig. 14).

For toluene oxidation, the nanorod-based catalyst showed the highest activity as compared to nanocubes and NPs [66] caused by a higher concentration of oxygen vacancies that also controlled the reaction rate. The Mars-van Krevelen reaction mechanism was proposed [207] (Fig. 15). The mechanism included benzyl radical transformation into benzaldehyde that further converted into formate through benzoate species, and finally completely oxidized to CO_2 and H_2O. The benzyl
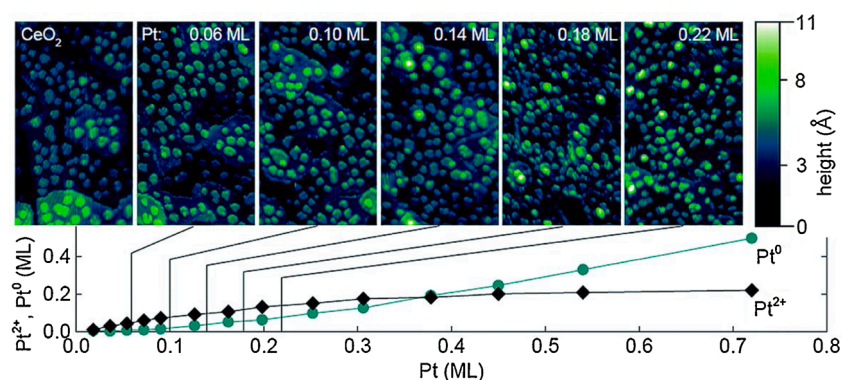
Fig. 11. Evolution of Pt^{2+} and Pt^0 SRPES signals during deposition of Pt on CeO_2(111) and annealing of Pt in O_2. Reproduced with permission from Ref. [196]. Copyright Royal Society of Chemistry.
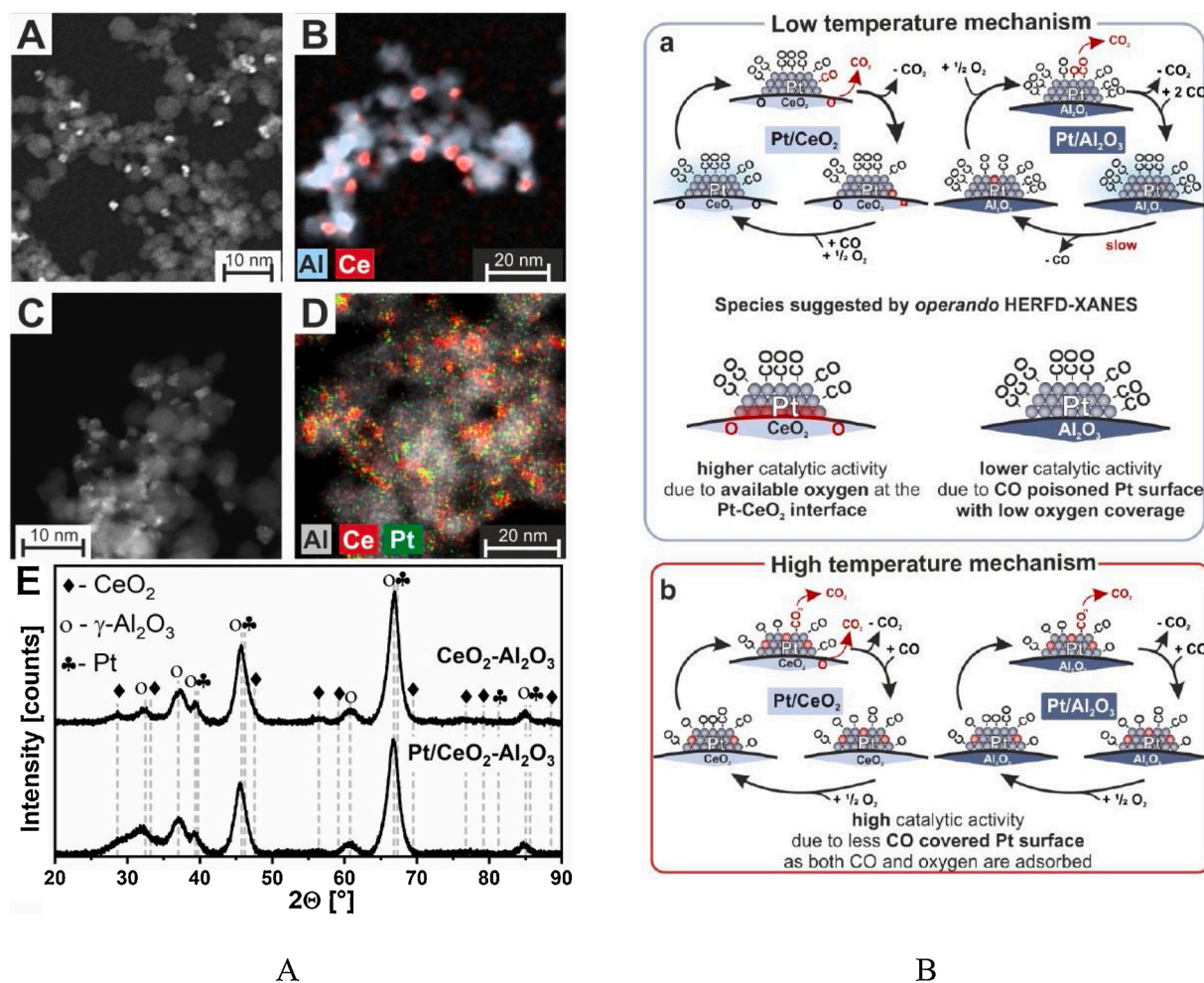
Fig. 12. (A) HAADF-STEM image (A) and EDX map (B) of CeO_2-Al_2O_3 reveal the presence of ceria NPs (3-5 nm) on the alumina support. HAADF-STEM image (C) and EDX map (D) of Pt/CeO_2-Al_2O_3 show again ceria NPs in the range of 3-5 nm. In addition, they identify Pt to be in a highly dispersed state and in intimate contact with ceria. XRD patterns (E) confirm the presence of ceria as small crystallites (broad reflections) and the absence of Pt reflections. Reproduced with permission from Ref. [108]. Copyright American Chemical Society. (B) Dominant CO oxidation reaction pathways for Pt/CeO_2 and Pt/Al_2O_3 at a) low temperature and b) high temperature. Reproduced with permission from Ref. [199]. Copyright American Chemical Society.

species were formed upon C—H bond breakage in the methyl group during the toluene adsorption on the catalyst surface. The platinum-ceria interaction facilitated the desired transformations.

The Pt catalysts supported on nanorod ceria were also subjected to dielectric barrier discharge plasma to reduce the T90 % value, increase Pt dispersion as well as concentrations of oxygen vacancies and Ce^{3+}

sites [72]. Toluene conversion was stable for 50 h under 9.6 vol% water vapor. Plasma treatment contributed to the organization of the surface morphologies and defects and facilitated the surface MSI [114].

For the NO_x storage-reduction Pt/BaO/CeO_2 catalysts, the rod-based specimen was superior to those based on cube and particle morphologies [208]. At GHSV = 360,000 h^{-1}, ~99 % NO_x conversion was achieved at
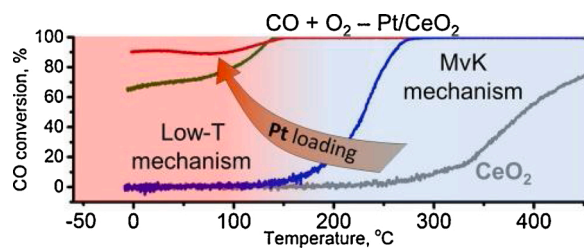
Fig. 13. Temperature dependence of CO conversion for Pt/CeO_2 catalysts with different loading. Reproduced with permissioan from Ref. [200]. Copyright Elsevier.

200−400 °C. For this catalyst, the NO_x storage capacity linearly depended on the concentration of oxygen vacancies [209]. The nanorod-based $PtRh/CeO_2/Al_2O_3$ three-way catalyst prepared by the hydrothermal method also showed high performance [210] that was caused by the formation of hollow ceria nanorods coated with nanoparticle arrays (2−5 nm) that served as selective supports for metals on ceria surfaces.

The Pt nanocrystals embedded into mesoporous ceria nanorods for CO_2 reduction with methane using focused solar light were fabricated [211]. Interfacial oxygen species impacted into CH_4 dissociation and oxidation of intermediate CH_x species over both ceria and Pt particles, with the reverse oxygen spillover occurring in the latter case. Simultaneously, Pt NPs participated in CO_2 dissociation to yield oxygen species migrating to ceria via oxygen spillover.

Thus, the nanorod-based systems showed high catalytic activity in several reactions. Still, the mechanisms determining the enhanced performance of such systems in the formation of surface ceria defects (first of all, oxygen vacancies) should be additionally elaborated given the possible contribution from the adjacent nanorod CeO_2 particles.

Recently, the support morphology effect on the states of Pt and Ce during CO oxidation was discussed [212]. While Pt/CeO_2 nanowires ensured the formation of higher content of Ce^{3+} and atomically dispersed Pt species, the nanocube-based system featured a higher impact of $Pt\delta^+$ species. The former morphology ensured stronger MSI, while the latter controlled the Pt particle size and availability of surface oxygen species.

For the Pt-embedded highly porous CeO_2 hollow sphere composites with the controlled position, distribution, and uniformity of Pt NPs, the morphology effects inhibited aggregation of NPs over the external shell of the ceria hollow spheres. The self-assembly-reduction-Ostwald ripening evolution mechanism involving the formation of oxygen vacancies and activation of surface chemisorbed oxygen was proposed [69, 213].
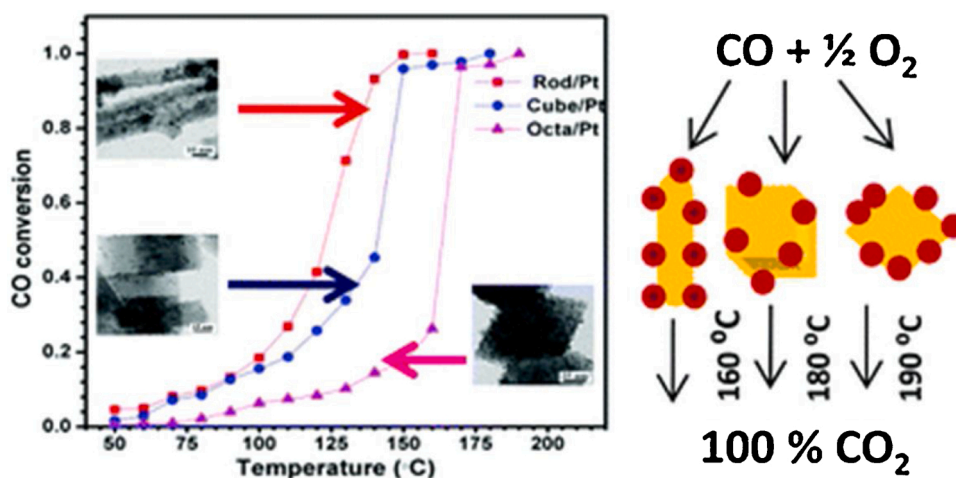
Fig. 14. The effect of ceria morphology on the performance of Pt/CeO_2 catalysts. Reproduced with permission from Ref. [102]. Copyright Royal Society of Chemistry.
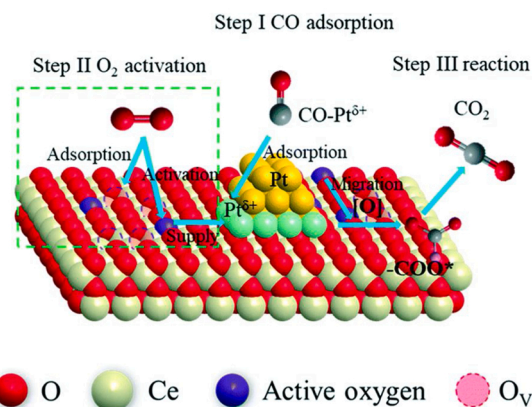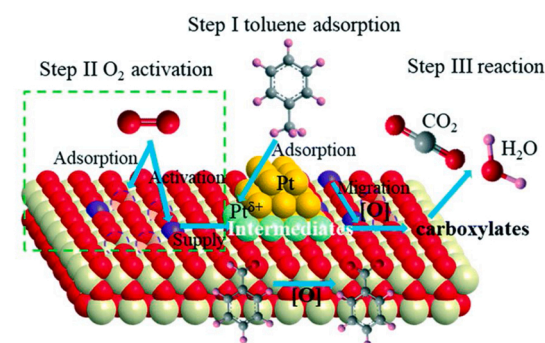
**Fig. 15.** Reaction mechanism of CO and toluene oxidation over the $Pt–CeO_2$ catalyst. Reproduced with permission from Ref. [207]. Copyright Royal Society of Chemistry.

Strong support morphology effect was demonstrated in the NO_x-assisted soot oxidation over ceria-supported Pt and Pt_3Sn NPs stabilized by organosilane or organostannane, with ceria nanocubes showing the synergistic effect with Pt NPs [215]. Tin contributed to low-temperature oxidation reactions. A similar approach was used for the nanostructured ceria-praseodymia impregnated with Pt nanoparticles [214], and the presence of mixed Ce-Pr oxide ensured improved NO_2 adsorption. The Pr effect prevailed the one of Pt. The synergistic effect of the nanocube morphology with the larger Pt NPs was assumed [215].

The core/shell and yolk/shell systems were proposed. The core-shell microporous ordered ZrO_2-supported 3DOM $Pt@CeO_{2-x}$ composites were prepared by the co-precipitation method [216]. The reactant-catalyst contact efficiency was improved due to the 3DOM support structure, while the core-shell structure increased the number of accessible active sites. Larger shell thickness caused lower catalyst activity. However, the question of the structure of the formed interfaces and uniformity of ceria shell distribution over Pt core remains unclear. The diffusional limitations that can take place under conditions of high space velocities should be also taken into account.

The (metal yolk)/(porous ceria shell) nanostructures for plasmonic catalysis under visible light with controlled shell thickness and metal yolk composition and size by heterogeneous growth of ceria on porous metal NPs followed by their calcination-induced shrinkage were obtained [217]. Monometallic Pt and bimetallic PtAg yolks were probed, with Ag incorporation resulting in enhanced visible light absorption of the yolk/shell nanostructures.

To sum up, the morphologies of ceria and Pt/CeO_2 catalysts on the basis thereof are diverse and complex and feature unique structural peculiarities defining their catalytic performance. The bulk properties of the ceria particles can affect the aboveling surface layers and physical-mechanical features of the whole catalyst grain. This aspect is frequently omitted, especially, when modeling the ceria morphology with theoretical approaches. The joint cooperative influence of the adjacent surface defects (e.g., the particle edge and the neighboring oxygen vacancies) on the reaction pathways may also take place and requires additional studies.

Morphological effects are also directly connected with the facet-dependent behavior [179,193,197,218]. The main facet-related aspects that can be further elaborated include but are not limited to (1) size effect of facets related to the number of atoms forming the facets, including those forming the subsurface layer, (2) joint action of adjacent facets on large molecules, (3) joint catalytic action of similar or different facets of two or more separate particles of equal or different sizes. The atomic composition of these facets plays an important role in catalysis, and the "size effects" for the facets with a different number of atoms can be different (e.g., the (111) grains composed of 15 and 55 atoms will demonstrate different performance caused by the coordination of atoms at the top and the subsequent layers). The structural peculiarities of the ceria facets determine the state of the adsorbed Pt species. In the case of real environmental processes utilizing rather large substrate molecules (e.g., nitrophenol), different molecule moieties can be activated over adjacent facets of the particle due to the rapid chemical processes. This also relates to the probable joint participation of the facets belonging to two or more adjacent particles. Both aspects can be additionally elaborated.

5. Modification of catalyst composition

The features and performance of $Pt–CeO_2$ catalysts in environmental catalytic reactions were also enhanced by applying supports and/or promoters. In a selection of cases represented, Pt or CeO_2 were used as a second metal or promoter/modifier, respectively.

5.1. Supports

The supports based on silica, alumina, and other oxides are actively

used to organize $Pt–CeO_2$ composites on their surfaces. The recent research activity was concentrated on the testing of ordered supports, alloys, and mixed oxide systems.

Various industrial and up-to-date research applications of silica-based supports attracted attention to the $Pt–CeO_2$ systems on the basis thereof. Generally, in environmental catalytic reactions silica allows improving both catalyst activity and stability. To enhance the support effects, the catalyst composition based on either core-shell or ordered mesoporous silicas were introduced.

In the core-shell-based catalyst formulations, the resulting composites featured porous/hollow structure beneficial for diffusion of reaction components, while SiO_2 shell effectively protected the catalyst [219] as well as afforded the high-temperature sintering resistance (up to 700 °C) with Pt NPs being self-assembled on 2-nm thick CeO_2 nanowires [220]. The modified core-shell structure was also applied to composites for two-step tandem CO_2 transformation into C_2-C_4 hydrocarbons (Fig. 16) [182]. In the latter case, the CeO_2-$Pt@mSiO_2$-Co composite was formed, where the Pt–ceria interface was responsible for CO_2 and H_2 selective conversion, while the Co–silica shell interface contributed to the subsequent Fischer-Tropsch process. The catalysts were stable for 40 h.

Ordered mesoporous silica (mainly, SBA-16) was used as a support for gas-phase water-resistant formaldehyde elimination over $Pt(0.7$ wt %)$/Ce_{0.68}Zr_{0.17}Bi_{0.15}O_{2-\delta}(16$ wt%)/SBA-16 composite [221] as well as in liquid-phase oxidation of phenol [222], 4-methylphenol [223] and 1,4-dioxane [224] over Pt/CeO_2–ZrO_2–SnO_2/SBA-16 catalyst. The SnO_2 dopant enhanced the oxygen release and storage abilities of the support. Although high catalyst performance was mentioned, more information could be provided on the role and distribution of components in the SBA channeled structure or on the support external surface as well as on their particular interactions and the derived synergistic effects. It is not unambiguous whether the component distribution within the ordered structure to form "nanoreactors" [225,226] is equally beneficial for all types of reactions. The roles of support steric effects and other catalyst components should also be discussed in more details.

Alumina-supported catalysts are widely used in environmental applications due to diverse phase composition and pronounced surface properties. Organization of $Pt–CeO_2$ interface on alumina was used in advanced diesel converters as well as in abatement of VOCs with different chemical composition and structure, including formaldehyde [119], toluene [227], dimethyl disulfide [228], n-butanol [229], dichloromethane [230], etc.

In toluene oxidation, the $Pt–CeO_2$ composites supported on γ-alumina allowed improving the dispersion of both Pt and ceria resulting in enhanced low-temperature component activities [113]. Moreover, a positive effect of plasma-assisted ultrasound irradiation on the surface morphology of Pt/Al_2O_3–CeO_2 nanocatalyst was demonstrated [116]. The 3DOM (3-dimensional ordered materials) ceria structure in 0.27 Pt/3DOM 26.9CeO_2–Al_2O_3 catalyst ensured higher activity as compared to samples utilizing Au, Ag, or Pd (Fig. 17) [227].

In formaldehyde removal, the use of AlOOH resulted in the RT activity of the as-prepared Pt/Al_9Ce_1 catalyst caused by a high content of surface hydroxyls, oxygen storage capacity of ceria, high Pt dispersion [119]. The reaction mechanism included formaldehyde oxidation into dioxymethane that can also isomerize to $(HCOOH)_{ads}$ and then interact with the active oxygen of ceria for complete decomposition. However, the phase transitions in the support and the roles of intermediate phases were poorly discussed.

In CH_3SSCH_3 oxidation, the 1.12 %Pt/CeO_2 and 1.20 %Pt/CeO_2-Al_2O_3 catalysts showed T50 % values of ~300 °C and ~380 °C, respectively, at WHSV of 720 g $gcat^{-1}$ h^{-1}, with the tendency to deactivation observed for the latter sample [231]. The drawback of the catalyst was connected with the Pt involvement in SO_3 production, with the latter interacting with water, active phase and/or support to produce H_2SO_4 and metal salts resulting in catalyst deactivation. At the same time, Cu- or Au-based samples were more active, and CH_3SSCH_3 reaction with the surface and/or bulk oxygen species enhanced the activity.
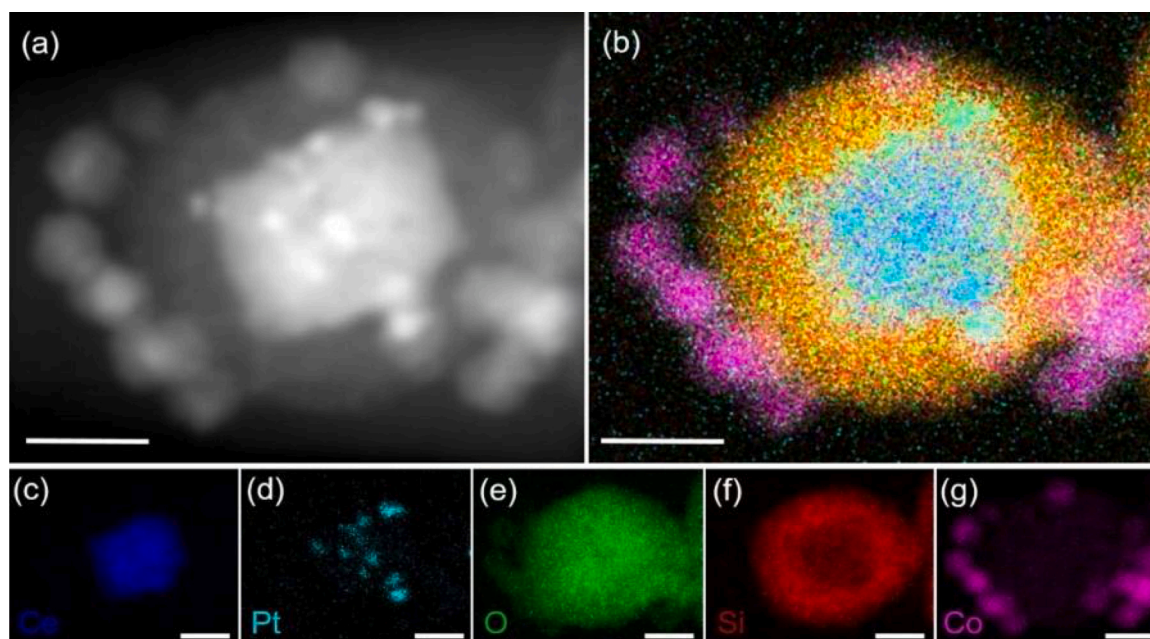
Fig. 16. (a) HAADF-STEM imaging of CeO_2-Pt@$mSiO_2$-Co. (b) Elemental mapping of $CeO_2-Pt@mSiO_2-Co$ with energy dispersive X-ray spectroscopy (EDS). Corresponding EDS elemental mapping for (c) Ce, (d) Pt, (e) O, (f) Si, and (g) Co, respectively. Scale bar: 20 nm. Reproduced with permission from Ref. [182]. Copyright American Chemical Society.
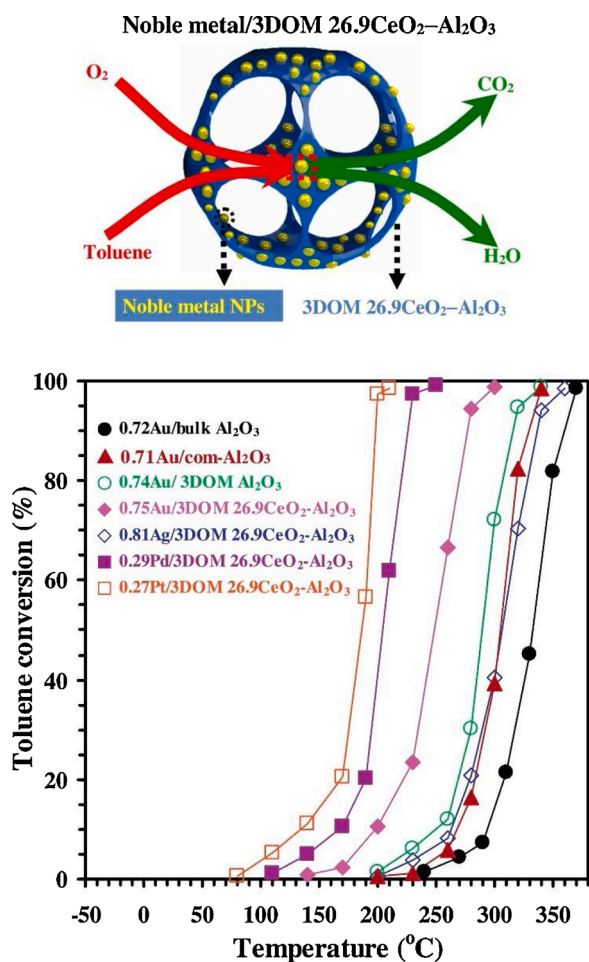

Fig. 17. Toluene conversion as a function of reaction temperature over the as-prepared samples at SV = 20,000 ml g^{-1} h^{-1}. Reproduced with permission from Ref. [227]. Copyright Elsevier.

Later [228] the 5%Cu-0.3 %Pt/γ-Al_2O_3-CeO_2 catalyst demonstrated improved CH_3SSCH_3 abatement activity (T50 %=~195 °C and T100 % = 262 °C, GHSV = 50,000 h^{-1}) accompanied by S tolerance and long-run stability for 1000 h.

Alumina is also the main part of the advanced diesel oxidation systems where platinum and ceria are dispersed over the support surface to form active ensembles. Generally, alumina provides the catalyst durability and opportunity to control the acid-base balance, while a number of additives were also used to further improve the catalytic properties and textural features of the materials. In CeO_x/Pt/Al_2O_3 catalysts for CO oxidation, the Pt NP reoxidation was considered the starting point of CO_2 formation and the loss of Pt-bound CO that existed as linearly bound surface species even after the light-off [232]. The CeO_x changed the CO adsorption properties over Pt sites. A dual CO light-off during the simultaneous oxidation of CO and C_3H_6 was reported [233], with C_3H_6 intermediates inhibiting the CO oxidation. The formation of intermediates was not suppressed by ceria that reduced the CO light-off temperature to a higher extent.

Due to the effect of support and synergistic action of Pt and ceria, the Pt-CeO_2/Al_2O_3 catalyst showed high NO_x conversion above 400 °C for anaerobic feeds [234]. Ceria redox pathway showed a secondary effect on NO_x conversion in O_2 excess inhibiting NO_x reduction above 400 °C. NO_x and oxygen storages were crucial factors (Fig. 18).

The alumina-supported Pt/BaO/CeO_2 [235] and Pt/Rh/BaO/CeO_2 [236] lean NO_x trap (LNT) catalyst for NO_x storage and reduction with H_2 or propene as reductants were proposed. The improved NO_x conversion for cycle times below 10 s was achieved, while higher cycling frequency improved the site efficiency and decreased NH_3 selectivity. In the latter case, the NO_x conversion did not depend on the reductant used and was caused by improved NO_x storage utilization. Hydrogen was a less effective reductant due to exothermic heat effects. Basically, the alumina support improved the deactivation resistance of the catalysts through several cycles. This was also mentioned for the system comprising the mixture of Pt-BaO/CeO_2 and Cu/CeO_2 composites [237, 238]. The synergistic effect of both catalysts improved the low-temperature NO_x removal efficiency during the lean-rich cycle operation. Under lean conditions, Cu/CeO_2 was more active in NO oxidation that allowed rapid NO_x storage over Pt-BaO/CeO_2. Under rich
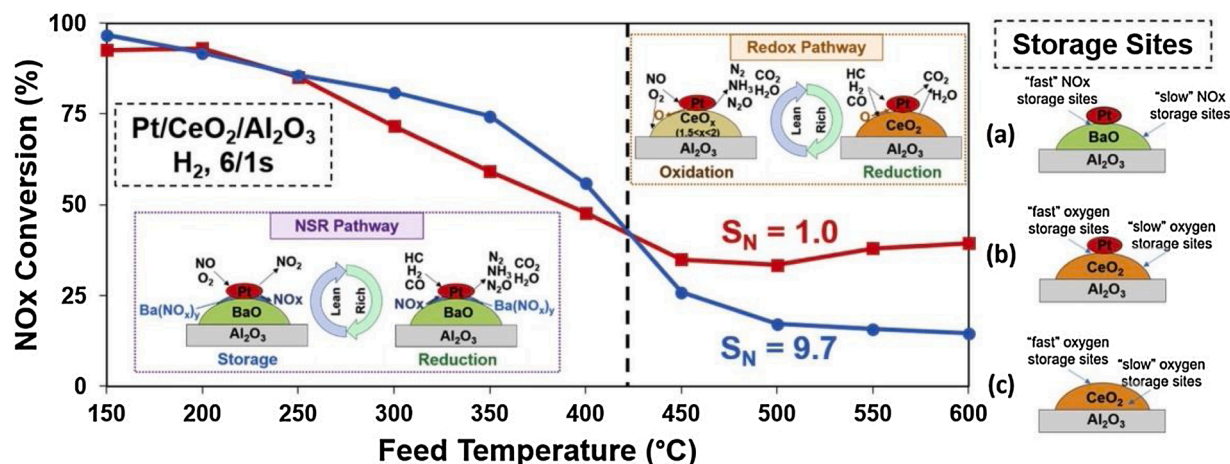
Fig. 18. Three working mechanism possibly involved in the Di-Air system, and Fast and slow NO_x or oxygen storage sites. Reproduced with permission from Ref. [234]. Copyright Elsevier.

conditions, the WGS reaction over Cu/CeO_2 generated hydrogen that facilitated the reduction of NO_x stored on Pt-BaO/CeO_2 with improved N_2 selectivity. The Pt–BaO–Cu/CeO_2 catalyst prepared by Pt and Cu co-deposition on ceria was less effective. Nevertheless, the structure of the catalyst active sites remains elusive, and the mechanism of cooperative action of such sites can be studied in more details. The mixture of catalysts of different nature allows enhancing the performance, and, hence, other combinations can be envisioned.

When speaking about alumina-based systems, it is noteworthy that some specific structural peculiarities (e.g., coordination of aluminum atoms) are most often not taken into account when discussing the support-related effects. The precursors of alumina (e.g., pseudobohemite [239,240]) also can be tested to prepare the alumina-supported catalysts with enhanced performance.

Recently, more attention was also given to mixed oxide systems comprising ceria mixture with transition metal oxides (Ti, Zr, etc.). Thus, TiO_2-CeO_2 composition was investigated due to its high own activity in O-containing VOCs abatement. The Pt-based catalysts were tested in phenol oxidation [241], and high conversion and CO_2 selectivity were caused by the small size of Pt particles or/and the presence of Lewis acid sites. In acetone removal [242], the 0.57 wt%CeO_2-0.05 wt% Pt/TiO_2 sample gave T90 % = 245 °C (1000 ppm acetone, SV = 40,000 ml g^{-1} h^{-1}), and the reaction proceeded through the substrate conversion into acetic and formic acids followed by the formation of carbonate species and resulting in total oxidation products. The 0.8 % Pd-Pt/CeO_2-Al_2O_3-TiO_2 catalyst completely converted 35 % methanol (1.0 vol.% CH_3OH, 2.0 vol.% O_2, GHSV: 35,000 h^{-1}) at 27 °C with the T50 % and T90 % values being 35 °C and 58 °C, respectively [243].

Most recently, Pt/CeO_2–TiO_2 catalysts prepared by modified ethylene glycol reduction method [244] showed improved activity in benzene and 1,2-dichloroethane degradation, and such an improvement was caused by the effect of reduced Pt size on the metal–support interaction of PtO_x species and CeO_2–TiO_2 mixed oxides. The sample with the smallest Pt size (1.53 nm) showed T90 % of 152 °C (1000 ppm, GHSV = 15,000 h^{-1}). Strong acidic sites were formed in the cases of larger Pt NPs. Nevertheless, the interplay between the oxygen vacancies and other surface defects (e.g., M^{3+} sites) of TiO_2 and CeO_2 can be additionally studied to reveal the probable synergistic effects. The effects of Pt species on the formation of surface defects in mixed oxide support also require research attention.

The $Ce_xZr_{1-x}O_2$ system demonstrated high potential as a support for environmental applications (e.g., soot oxidation [245], oxygen storage materials for three-way converters [246]). Recently, a solvent evaporation–induced co-assembly process to prepare $Pt/Ce_{0.8}Zr_{0.2}O_2$ catalysts with high surface area and large pore size using poly(ethylene

oxide)-block polystyrene as a template (Fig. 19) [106]. The hydrolyzed hydrophilic inorganic Ce and Zr species can interact with the PEO segments via hydrogen bonding, and the copolymers can give spherical composite micelles (that were further packed into face-centered cubic ordered mesostructures) composed of hydrophobic blocks as the core and inorganic species associated PEO segments as the shell.

The core-shell type CeO_2/ZrO_2 support was proposed to reduce the Pt content in the exhaust gas catalyst [247]. Ceria formed a thin layer and aggregates over zirconia, while Pt concentrated at CeO_2-rich sites. Macroporous $Ce_{0.5}Zr_{0.5}O_2$ solid solution was also fabricated as support for Pd + Rh + Pt three-way catalyst [248] that exhibited ignition temperature for CO + NO_x and C_3H_8 at ~240 °C and 270 °C (air rate = 200 L/h, A/F = 14.0), respectively, with the maximal efficiencies for CO, NO_x, and C_3H_8 of 100 %, 98 %, and 97 %. The $Pt/Ce_xZr_{1-x}O_2$ composite was used in passive NO_x adsorber applications [249]. CeO_2 addition to zirconia improved low-temperature (<160 °C) NO_x storage efficiency. An increase in CeO_2 content resulted in the formation of a higher amount of nitrite species. The Pt-Pd-copromoted sample showed enhanced NO_x adsorption-desorption performance.

In Pt/CeO_2-ZrO_2/Al_2O_3 composites [250] zirconia and ceria interacted with alumina hydroxyls and Lewis acid sites, respectively. The isovalent Zr^{4+} cations partially incorporated into ceria lattice to form $Ce_{1-x}Zr_xO_2$ mixed oxide, while a part of zirconia also presented in a highly disordered amorphous form. This facilitated the low-temperature ceria reduction. Larger $Pt°$ particles were formed over ZrO_2/Al_2O_3. NO readily adsorbed over reduced Pt-based materials due to the promotion of NO disproportionation by metallic Pt. NO_x was reduced in the presence of H_2.

It is noteworthy that the $Ce_xZr_{1-x}O_2$ composites usually feature composition-dependent performance, and a detailed analysis of the effects of Ce/Zr ratios is required. Moreover, the calcination temperature can impose significant effects in such a mixed oxide system, and its influence can be further elaborated. It is noteworthy that over reduced Pt/CeO_2-ZrO_2 catalysts, the spillover of H species onto the support can occur even at room temperature [251].

The Pt–CeO_2 composition was also anchored on a number of other supports such as Fecralloy 3D opened foam substrate to form CO oxidation [252] and methanol combustion [253] catalysts, BEA zeolite to prepare ozone-enhanced toluene decomposition catalyst [254], and carbon-based supports (graphene oxide (GO)/CeO_2 nanosheets [120] or N-doped activated carbon [255]). The Fecralloy-based catalysts demonstrated stability against sintering and active phase reconstruction up to 800 °C [252]. The content and functional features of the support were responsible for the stabilization of active oxygen through the π-bonding [120]. However, the nature of active sites and features of
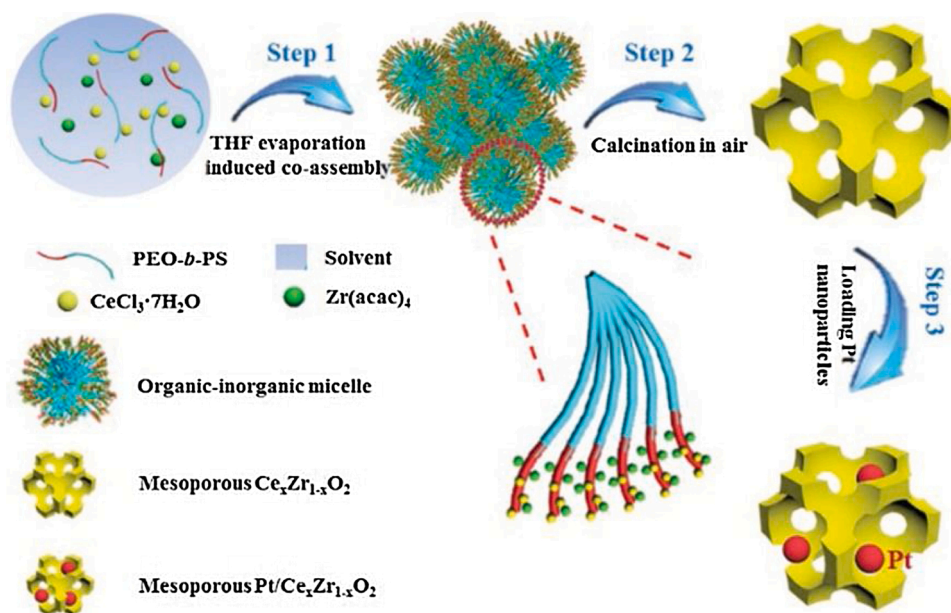
Fig. 19. The synthesis process of ordered mesoporous $Ce_xZr_{1-x}O_2$ solid solutions and $Pt/Ce_xZr_{1-x}O_2$ catalysts. Reproduced with permission from Ref. [106]. Copyright WILEY-VCH Verlag GmbH & Co. KGaA.

surface ensembles remains unclear given the existence of several interfaces between the catalyst components.

The nano-array monolithic catalyst comprised highly dispersed uniform Pt NPs decorated with ceria nanoflakes supported on 3D-channeled cordierite honeycomb substrates [105] as well as the Pt-CeO$_2$ [256] and 1 wt%Pt-incorporated CoO_x-CeO_x [257] composites supported on stainless steel wire meshes to prepare the cartridges capable of simultaneous combustion of VOCs (n-hexane, acetyl acetate, and toluene) and soot were also proposed. The relationship between phase composition and catalyst performance should be further developed. The effects of support thermal conductivity on the catalyst performance can also be additionally studied.

Thus, various supports for interacting Pt–CeO$_2$ ensembles were proposed and showed a profound effect on the features of Pt and ceria species, including dispersion, the strength of interaction, etc. At the same time, the surface properties of these supports, namely, the involvement of the support-related surface species (e.g., hydroxyls), coordination of oxide-forming atoms, are often ignored when interpreting the experimentally observed catalyst behavior. The structure-performance relationships should also be taken into account when dealing with the mixed oxide multicomponent composites.

5.2. Promoters and modifiers

The performance of Pt/CeO$_2$ catalysts can be also enhanced by applying metal-based promoters and modifiers to form bimetallic ceria-based composites. Recently, Sn [94], noble metals (Au [258], Ag [259]), and transition metal compounds (Co [260], Ni [95], Mn [261,262], Eu [70], etc.) showed appealing activity. Tin destabilized Pt^{4+} cations and increased the content of lattice Ce^{3+} up to 50 at.% in the $Pt/CeSnO_x$ composites prepared by ceria modification using plasma-arc sputtering of active components (Pt, Ce, Sn) along with carbon from a graphite electrode in a helium environment [94]. The lanthanoid-based materials [70] effectively promoted Pt/CeO$_2$ catalysts and affected the redox properties, concentration of lattice oxygen species as well as Ce^{3+} content to increase the dispersion and activity of Pt active sites.

The Fe-, Co- and Ni-modified catalysts possessed higher stability due to reversible compensation of the consumed oxygen species and strengthening of the MSI [95]. The bimetallic Pt-Ni-based composites showed superior activity as compared to monometallic counterparts in

ethane and butane reforming [17,18], and the effect was caused by the synergistic action of metals as well as the existence of Pt–CeO$_2$ interface. Recently, the hybrid architecture of a 0D/2D CeO$_2$ quantum dot (QD)/porous NiO hexagonal nanoplate supported ultralow-content (0.08 wt%.) Pt was proposed [263]. The obtained composite denoted as Pt/NiCe$_4$ was used in formaldehyde abatement and was superior to Pt/CeO$_2$ and Pt/NiO. The NiO-deposited QD ceria morphology ensured higher exposure of active sites and contact of the components. The Ni insertion into the ceria lattice increased the amount of generated active oxygen species. Earlier [264] the NiO additive to Pt/CeO$_2$-ZrO$_2$/γ-Al$_2$O$_3$ catalysts was shown to enhance oxygen release and storage features. Thus, for Ni-based composites, the catalyst performance was achieved by using Pt as a promoter or due to the specific ceria morphology or the use of additional supports and modifiers. A combination of these options can further improve the catalyst performance in certain reactions, including the DRM process.

A series of core-shell Fe$_2$O$_3$@CeO$_2$-Pt catalysts (Fig. 20) showing $X_{CH4}=\sim80$ %, $X_{CO2}=\sim82$ %, and $Y_{H2}=\sim11$ mmol g^{-1} in the first cycle was prepared [265]. The DRM process was integrated into a chemical looping-based H$_2$ production scheme. Under the process conditions, the Pt NP growth was observed. The PtO$_x$–support interaction ensured redispersion of these NPs on ceria during the oxidative regeneration.

It is noteworthy that the transition metals feature several oxidation states, and their probable simultaneous transitions in multicomponent systems should be taken into account for correct interpretations of the catalytic action and synergistic effects. Sophisticated surface science studies are required to detect such states and understand how the ratios between them affect the catalyst properties. The structure of solid solutions formed will also be of profound interest.

Noble metals mostly affect the strength of Pt–CeO$_2$ interaction as well as the reduction temperature, reoxidation ability, and availability of mobile oxygen species in ceria. Application of gold in Pt-Au/CeO$_2$ [258] and Pt-Au/TiO$_2$-CeO$_2$ [266] composites showed the opportunities for simultaneous room-temperature abatement of CO and formaldehyde caused by the effect of more negatively charged Pt NPs and Au^+ species to yield chemisorbed oxygen. Water had a negative effect on the mixture conversion, while H$_2$ promoted the co-oxidation of formaldehyde and CO due to the formation of OOH and OH intermediates. The Au^+ reduction and a decrease of Ce^{3+} content weakened the MSI. The PLA in the liquid produced Pt and Au alloyed NPs assembled on ceria nanotubes
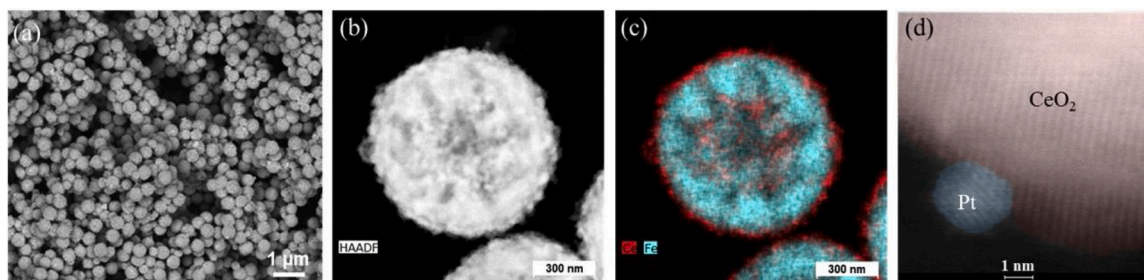
Fig. 20. (a) SEM image of the as-synthesized $Fe_2O_3@CeO_2$-Pt, (b) HAADF-STEM image of $Fe_2O_3@CeO_2$-Pt (c) Elemental mapping of $Fe_2O_3@CeO_2$-Pt with EDS, (d) High resolution HAADF-STEM image of a Pt NP on the CeO_2 shell. Reproduced with permission from Ref. [265]. Copyright Elsevier.

to show strong synergistic effect due to shifting of Pt d band center after alloying accompanied by cooperation between Pt and Au or PtAu particles in 4-nitrophenol reduction [132].

Recently, the opportunity to use silver to form ceria-supported Pt-Ag catalysts for 4-nitrophenol hydrogenation with $NaBH_4$ was demonstrated [267]. The superior catalyst activity as compared to ceria-supported monometallic (Pt or Ag) samples was caused by the formation of Pt-Ag bimetallic NPs due to the simultaneous reduction of highly dispersed interplaying platinum and silver species (Fig. 21) [133]. The core effect of Ag was connected with the fine-tuning of the MSI and enhancement of the catalytic activity.

Although not all noble metals are highly miscible with Pt (e.g., silver), still it is interesting to understand the optimal distribution of both metals and their bimetallic species on ceria to ensure the potential synergistic effects arising from their proximity on the support surface. To unlock the potential of such complexes, it is necessary to develop robust preparation techniques. Sophisticated surface science methods and theoretical models will also help to deepen the understanding.

The MnO_x-containing Pt-CeO_2-based systems are actively studied in the abatement of VOCs, e.g., toluene [268], due to the high effect of MnO_x on the ceria properties. The improved low-temperature reducibility of such composites is connected with the formation of MnO_x–CeO_2 solid solution, while Pt facilitated the O_2 activation over the support. The formation of three formaldehyde oxide isomers (formic acid, dioxirane, CH_2OO Criegee) over Pt/MnO_x-CeO_2 catalyst was revealed [269], with the latter being more reactive, but having a lower lifetime. The water exhibited a positive effect.

For toluene abatement, $PtMn_y$ intermetallic nanocrystals were proposed to prepare the 0.37Pt−0.16MnO_x/meso-CeO_2 sample derived from the KIT-6 pathway. The ordered mesoporous architecture ensured thermal stability and water resistance [268]. The catalyst activity did

not change much upon the addition of up to 5%vol. water vapor (Fig. 22A). The catalyst deactivation upon CO_2 addition was found reversible due to the competitive adsorption of toluene and CO_2 (Fig. 22B).

The promotion by NO_x additives on Pt/MnO_x-CeO_2 catalysts for soot oxidation under tight contact (TC) and loose contact (LC) conditions was shown [270]. Under TC conditions, no NO_x promotion was observed due to the surface blocking by soot, while under loose contact conditions the NO promoting effect was superior to the one of NO_2. When MnO_x-CeO_2 mixed oxides were introduced to Pt/Al_2O_3 catalyst for soot oxidation, the opportunity for complete recovery of the S-poisoned Pt/MnO_x-CeO_2/Al_2O_3 catalyst after 30 min reduction in ammonia at 550 °C was demonstrated [271]. Both surface and bulk sulphates were detected, with the latter species being able to migrate onto the Pt surface in the ammonia presence. The Pt-assisted reduction of sulphates occurred at lower temperatures as compared to the case of catalyst regenerated in N_2 medium. NO oxidation depended strongly on the Pt particle size distribution and oxidation state. It is noteworthy that while preparing the mixed Mn–Ce oxide supports it is necessary to bear in mind that many phases can be formed during the preparation procedures, and, hence, the effects of calcination temperature as well as conditions of support/catalyst pretreatment should be studied in more details. The order of component introduction can also cause different catalyst surface structures and should be thoroughly considered for specific reactions.

Thus, many kinds of promoters were proposed for environmental catalysts utilizing Pt-CeO_2 interfaces. Depending on the promoter nature, various features of catalyst components were affected, with the core attention being paid to the MSI effects (that is discussed below). The promoters are selected in such a way that they affect the properties of ceria (compounds based on lanthanoids, transition metals (e.g., Zr)) or platinum (noble metals) or both components (e.g., compounds of iron
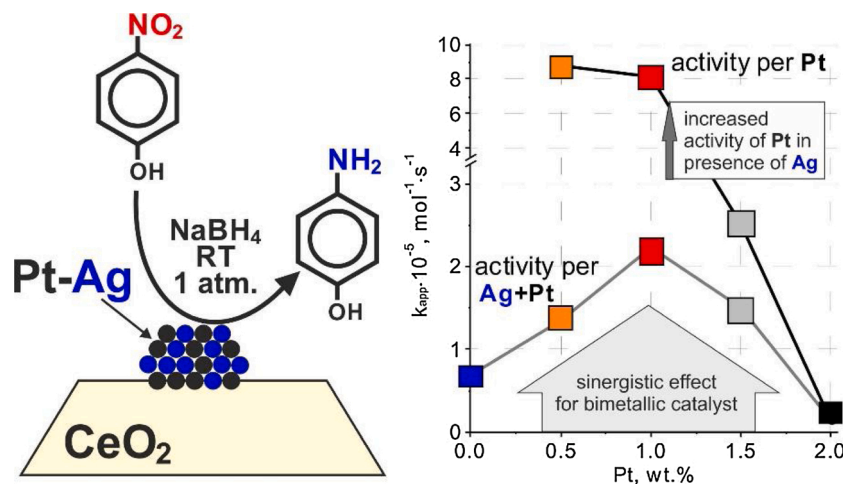

Fig. 21. Catalytic activity of Pt-Ag/CeO_2 catalyst in 4-nitrophenol reduction and the corresponding synergistic effect of Pt and Ag in bimetallic catalysts. Reproduced with permission from Ref. [133]. Copyright Elsevier.
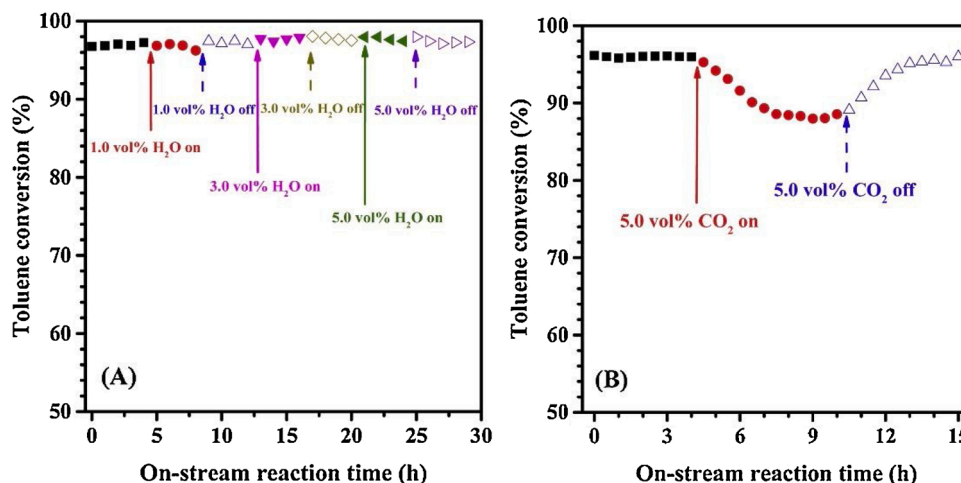
Fig. 22. Effects of (A) H_2O and (B) CO_2 on catalytic activity of $0.37Pt-0.16MnO_x/meso-CeO_2$ at 180 °C and SV = 40,000 mL/(g h). Reproduced with permission from Ref. [268]. Copyright Elsevier.

triad metals). The bi-, tri- and multimetallic catalyst formulations were proposed, and the mechanisms of formation of bimetallic particles, ordered and/or unordered alloys with different structures should be understood in more details as these species significantly affect the catalyst performance. At the same time, small amounts of promoters used make the promoter-containing phases formed highly dispersed that complicates their experimental studies with the majority of available techniques. Nevertheless, new insights can be provided here using the theoretical approaches that can be directed towards revealing the surface distribution of the promoters, including self-organization and fine-tuning of the catalytic active sites, and the mechanisms of their involvement in the key stages of the considered environmental processes.

6. Active sites and metal–support interactions

6.1. Nature and structure of active sites

The nature and structure of the active sites are one of the cornerstone issues in catalysis. The reasons are connected with the fact that due to the extremely small sizes and limitations of experimental techniques. It is usually difficult to detect such sites, reveal their structure, and in situ understand the mechanisms of their formation during the catalyst synthesis and under the influence of the reaction mixture as well as the dynamics of their reactivity in a particular reaction. With that, a number of currently available advanced characterization techniques allow shedding light on the structure of active sites. These techniques include but are not limited to operando high energy resolution fluorescence detected X-ray absorption near edge structure (HERFD-XANES) [199], high-angle annular dark-field imaging scanning transmission electron microscopy (HAADF-STEM) [61,71,108,180,262], synchrotron radiation photoelectron spectroscopy (SRPES) [190], scanning tunneling microscopy (STM) [187,272], ambient-pressure X-ray photoelectron spectroscopy (APXPS) [273], in situ X-ray absorption spectroscopy (XAS) [191], etc.

Structural defects in ceria, especially oxygen vacancies, are crucial factors in the surface chemistry of $Pt–CeO_2$ interfaces. Oxygen vacancies belong to those ceria surface defects considered the active sites. Basically, the vacancy is formed during the electron transfer from O atoms to Ce ions located nearby the vacancy site to make the latter reduced to Ce^{3+} state. The formation of oxygen vacancies was shown to depend on a number of factors, including applied preparation approaches [274], high-energy impact [72] and treatment procedures [64,90], catalyst composition [178,115], support morphology [66,72]. The effect of the converted substrate molecules can also be expected and requires

additional investigation. A number of publications also show the opportunities to characterize the oxygen vacancies using surface science and physical-chemical methods, including XPS [175,208], STM, XAS [175,208], temperature-programmed methods [208,275], UV–vis DR spectroscopy [275], EPR, and IR spectroscopy [275]. The positron annihilation spectroscopy (PAS) [175] also allowed exarticulating the type of vacancy that traps Pt atoms. Recently, the advanced Raman techniques for ex situ, in situ, and operando characterization of CeO_2-based catalysts were discussed [276], and the peculiarities of the spectral modifications induced by nanocrystallinity, defects, doping, and reduction were revealed. The described approaches allowed identifying the effects of adsorbed molecular species, isolated atoms, nanoclusters as well as peroxo and superoxo ensembles and surface hydroxyls.

Generally, the organization of metal–CeO_2 interfaces with the participation of dopants was shown to be crucial for the formation of oxygen vacancies and improvement of ceria reducibility [277]. The formation of interfacial oxygen vacancies can be controlled by the low-lying partially occupied Pt-induced gap states [175]. Most recently, the use of co-dopants (noble metals, iron triad metals, Sn, Ga, Sm, etc.) was shown to enhance oxygen vacancy formation, and the process depended on the dopant binding energy on various ceria surfaces ($CeO_2(111)$, (110), and (100)) [278] implying the opportunities to tune the binding strength. Higher binding energy reflected hindered the formation of oxygen vacancies. For Pt/CeO_2 and $Pt/CeSnO_x$ catalysts of low-temperature CO oxidation, the Ce^{4+} substitution by Sn^{4+} favored the formation of oxygen vacancies near the dopants and induced high oxygen mobility in the nanostructured ceria that was caused by strongly distorted oxygen coordination of Sn^{4+} compared to Ce^{4+} [94]. The Ga dopant facilitated the formation of oxygen vacancies, and Ga-anchored single Pt atoms were more stable [279]. Oxygen vacancies participated in O_2 activation further reacting with Pt-preadsorbed CO with a lower energy barrier. Small Pt clusters facilitated the formation of oxygen vacancies in Pt-lean and Pt-rich ceria(111) catalysts as well as Pt-containing reduced $Sm_{0.2}Ce_{0.8}O_{1.9}(111)$ (SDC) system [280]. In a row of ceria-supported noble metal catalysts (M = Ag, Au, Pd, Pt, and Rh) the following activity row was obtained [281]: Rh/CeO_2 > Ag/CeO_2 > Pt/CeO_2 > Au/CeO_2 > Pd/CeO_2 > CeO_2. The DFT calculations showed that the vacancy formation energy gradually decreased in a row CeO_2 > Pd_4/CeO_2 > Pt_4/CeO_2 > Au_4/CeO_2 = Ag_4/CeO_2 > Rh_4/CeO_2.

It is noteworthy that the cooperation of several types of oxygen vacancies was recently shown. Thus, for $Pt-CeO_2/MnO_2$ heterocatalysts for toluene oxidation [282] the synergistic effect of oxygen vacancies decorated on the surface as well as the intrinsic ones was assumed to occur through the oxygen replenishment–migration pathway (Fig. 23) that was responsible for the observed activity.

There is an ongoing discussion on the nature of active oxygen species that can be related to Pt, ceria and/or interfacial sites. The process of formation of oxygen species was shown to depend on the catalyst preparation method [263], the composition of the reaction mixture [97] that affects the source of oxygen species (e.g., the concentration of surface nitrates formed upon NO addition [275]), etc. Interfacial O* species at the boundary with ultrasmall Pt clusters (~1.5 nm) ensured high activity, while ceria did not alter the CO binding energies but enhanced the reactivity of the interfacial lattice oxygen atoms [283]. Strong interaction between the surface oxygen and adjacent Pt species affected migration of oxygen species, the formation of surface oxygen vacancies, and changing of the low-temperature catalyst reducibility [207]. The formed carbon-related species (bicarbonates and carbonates) were completely converted to CO_2.

The nature of the active surface lattice oxygen species produced using the high-temperature steam treatment of atomically dispersed Pt/CeO_2 catalysts was also discussed [97]. High-temperature exposure to water imposed oxygen vacancies redistribution to the CeO_2(111) facet resulting in the filling of oxygen vacancies by water to yield a couple of $O_{lattice}$[H] sites near Pt atoms. Such sites coordinated with Pt to react with Pt-bound CO and yielded oxygen vacancies that were refilled through oxygen adsorption. The O_2-assisted deprotonation of carboxyl intermediate yielded CO_2. The OO[H] species interacted with another CO molecule to yield CO_2 that then readily desorbed. The high thermal stability up to 767 °C of the $O_{lattice}$[H] was pointed out and can be regenerated during the CO oxidation cycles.

The role of oxidative species in photocatalytic oxidation of formic acid was also mentioned for Pt-loaded ceria [284]. Three modes of illumination conditions were employed, i.e., (1) no illumination, (2) no illumination with UV light pretreatment, and (3) continuous UV illumination. The key species were surface active oxygen (PtO_{ads} and O^-_{ads}) under no illumination with and without light pre-treatment, while under photocatalytic conditions, photogenerated holes and electrons formed hydroxyl $^{\cdot}OH$ and superoxide radicals ($^{\cdot}O_2^-$), respectively (Fig. 24).

Due to the high interest in Pt–CeO_2 catalytic interfaces, several interpretations of the active surface ensembles serving as active sites were proposed. The Pt loading connected with the Pt dispersion and distribution on the catalyst surface significantly affected the structure of such surface complexes. In particular, the Pt–O–Ce ensembles with a low oxygen coordination number were considered the active sites [67,74]. It is noteworthy that the coordination number of Pt-bound oxygen also affected the catalytic activity in the case of subnanometric PtO_x clusters supported on CeO_2 (110) nanowires [101], with the increased concentration of the surrounding oxygen overstabilizing Pt atoms resulting in the lower activity of some Pt sites. The opportunity for the transition of the homogeneous solid solutions of Pt in ceria lattice ($PtCeO_x$) into
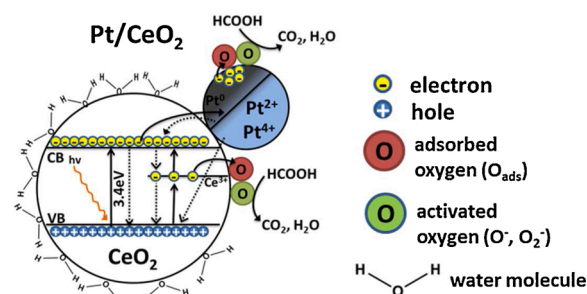

Fig. 24. Schematic detailing the mechanisms for dark catalytic FA oxidation using UV light pre-treated Pt/CeO_2. Reproduced with permission from Ref. [284]. Copyright Elsevier.

$(PtO)_m$ associates was also demonstrated [285]. Thermodynamic calculations revealed the PtO species to be the most stable ones at standard conditions [179].

Recently, the formation of Pt–O–Pt ensembles on ceria in Pt_1/CeO_2 catalyst demonstrating enhanced performance in CO oxidation under O-rich conditions was proposed [177]. The calculations over Pt_8/CeO_2 showed rearrangement into Pt_8O_{14} that contained Pt–O–Pt unit. Different transition states of O_2 activation were found for the cases of the Pt_1-O-Ce (Mars-van Krevelen mechanism of CO oxidation) and Pt–O–Pt (participation of bridge oxygen) ensembles (Fig. 25). It is noteworthy that some of the Pt atoms probably do not form the Pt – O–Ce ensembles.

More complicated compositions of the active ensembles were also considered. Additional interpretations showed the formation of energetically stable peroxo Pt–O–O–Ce species upon PtO_2 species adsorption at (100) facet of the $Ce_{40}O_{80}$ model substrate [197]. The interfacial Pt – O–Ce – O–Al ensembles and high concentration of oxygen vacancies were proposed for the Pt/15 %CeO_2/SiO_2-Al_2O_3 catalyst for oxidation of CO, hydrocarbon, and NO [286]. In catalytic oxidation of benzenes over Pt-xW/CeO_2 catalysts [127], the W–O–Ce and Pt–O–W ensembles were revealed that respectively increased the concentration of oxygen vacancies and acidity and promoted the reducibility and availability of the surface oxygen. The synergistic effects of several metal dopants were shown in 4%Ni-0.2 %Au-0.2 %Pt-Al_2O_3-10 %CeO_2 catalyst [287], where the interactions between metal dopants and Ni provided easy NiO reduction and decreasing of particle size. The trimetal catalyst showed high performance due to the formation of Ni–Au–Pt ensembles participating in the growth of bamboo-like carbon nanotubes.

The models accounting for different surface defects (Fig. 26) were proposed [288]. The Pt adatoms preferably were segregated at the steps, with the Pt binding energies being higher than at the stoichiometric or
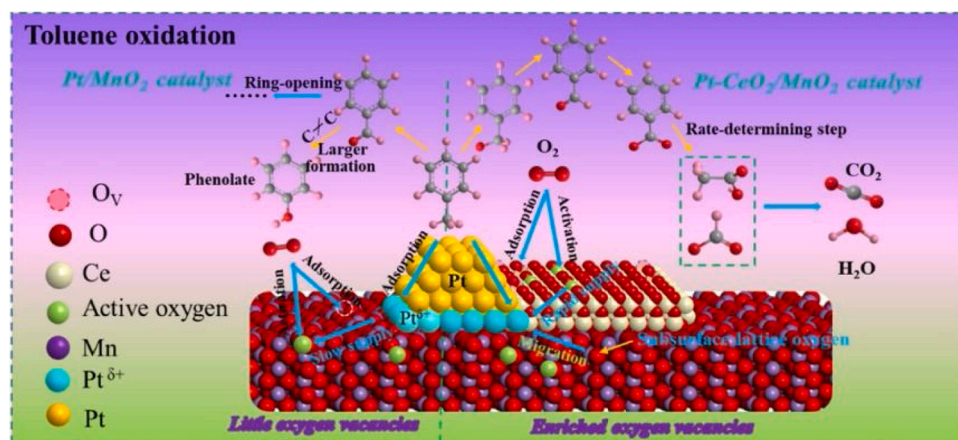

Fig. 23. Schematic illustration of proposed mechanisms for toluene oxidation over the Pt-CeO_2/MnO_2 catalyst. Reproduced with permission from Ref. [282]. Copyright Elsevier.
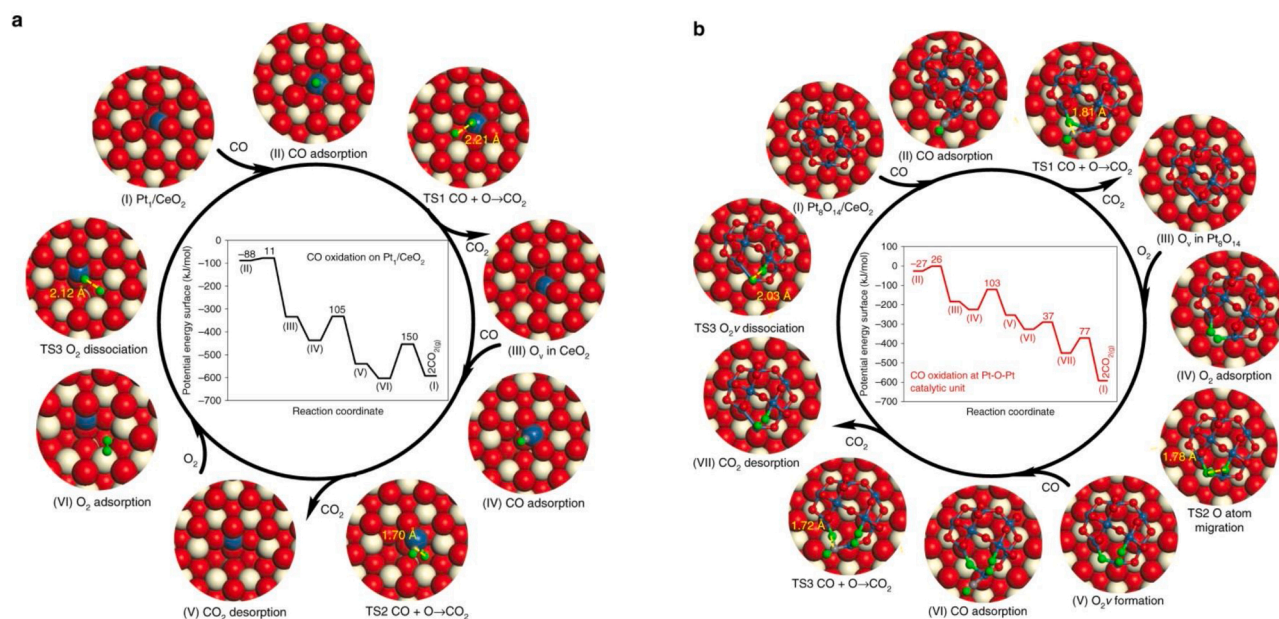
Fig. 25. Potential energy diagrams and configurations for CO oxidation cycle. CO oxidation proceeds on (a) the Pt_1/CeO_2 and (b) at the Pt-O-Pt catalytic unit in Pt_8O_{14}/CeO_2. Beige, red, and blue spheres are Ce, O, and Pt atoms, respectively. The small gray and green spheres are C and O atoms involved in CO oxidation. Reproduced with permission from Ref. [177]. Copyright Nature Publishing Group. (For interpretation of the references to colour in this figure legend, the reader is referred to the web version of this article.)

defective (111) terraces. Such an approach is rather informative, while still there exists the need to characterize the effects arising from the cooperative action of these defects since such interpretations can definitely deepen the understanding of the process mechanisms and make the models used closer to the real catalytic systems.

To sum up, the surface of the real catalyst features the combination of active sites related to solely Pt (single-atom species, clusters and/or nanoparticles with edges, corners, steps, etc.) and/or ceria (oxygen vacancies, terraces, etc.) as well to the Pt–CeO_2 interface (Pt-O-Ce ensembles, interfacial oxygen species, etc.), and, hence, the cooperation of such sites should be further considered. The interplay between these sites significantly contributes to the overall catalyst performance (e.g., the synergistic action of the acid-base and/or redox interfacial sites in tuning the catalyst performance under reducing conditions was demonstrated [289]). However, detailed surface science studies are required to reveal the ratios between these species, their surface distribution. Understanding these challenges will allow rational designing of active and stable surface ensembles determining the enhanced catalyst performance. Moreover, various solid solutions are formed [99] depending on the catalyst composition and preparation conditions, and their exact composition and structure remain unclear. The understanding of these issues requires the application of sophisticated surface science techniques.

6.2. Metal–support interactions

The MSI is among the most important aspects defining the catalyst performance in many catalytic reactions [290], and a plethora of publications dealing with Pt/CeO_2 catalysts mentions the MSI as the main reason for the enhanced catalyst performance [e.g., 67,909,196,254, 266,183,187,193,114,207,280]. The MSI is usually interconnected with one or more aspects such as the parameters of interfacial perimeter [199], charge transfer [65,289], morphology [291,193], chemical and phase composition (mostly, synergistic effects between the catalyst components [220] as well as with the SMSI [175]. The strength of the MSI can be also affected by such factors as, for instance, the type of Pt precursor used [147], thermal stability under reducing/oxidizing conditions [90], catalyst pretreatment conditions [96]. The facet

dependence of the MSI strength was also revealed [193] and followed the row: (100) > (110) > (111). The effects of modification of the catalyst composition on the MSI were also shown. For instance, for single-atom S-$Pt/Ce_{0.7}Zr_{0.3}O_2$ catalysts [167], the CeO_2 promoter showed the effect on the catalyst performance due to the strong Pt–CeO_2 interaction. For the ceria- and zirconia-supported Pt–Co_3O_4 catalysts of CO oxidation and NO_x reduction [292] the observed catalytic activity was attributed to the uniform particle size and the electronic MSI. The N dopant to Ce-doped activated carbon used as the Pt support showed improved performance due to SMSI of both N and Pt in the activated carbon skeleton [255]. In Pt-Au/TiO_2-CeO_2 composites, the MSI can be weakened upon Au^+ reduction and Ce^{3+} content decrease [266].

Multiple interactions were considered in several catalysts. For instance, a triple strong interaction between Pt, CeO_2, and ZnO was shown to maximize the photocatalytic activity of $Pt/CeO_2/ZnO$ ternary composite for phenol photodegradation [293], with the 91 % phenol degrading during the 60 min under the UV light irradiation. The redox cycle of Ce species, the formation of ZnO–CeO_2 interface, and Pt-induced electron transfer were mentioned as the major reasons for performance enhancement. The triple WO_x–ceria–Pt interactions [127] resulted in the formation of W–O–Ce and Pt–O–W surface ensembles that respectively increased the concentration of oxygen vacancies and acidity and promoted the reducibility and availability of the surface oxygen. The structures were stable for 50 h even under moist conditions. Chlorobenzene interacted with hydroxyls to produce phenolate further converted to acetaldehyde and carboxylates with ceria lattice oxygen. Simultaneously, surface oxygen completely oxidized partial oxidation products. Thus, the catalyst composition and organization of proper interplays between the catalyst components open up new opportunities for catalyst intensification. However, the exact component ratios should be precisely preselected.

Several publications demonstrated that the MSI effect can be affected by the phase composition of Pt/CeO_2 catalyst. In particular, the controlling of the MSI strength mediated the CO oxidation ability of Pt/CeO_2 catalysts. The support treated at 800 °C prior to Pt deposition kept high Pt dispersion after thermal aging and was sintering-resistant. The enhanced catalytic activity was explained by weaker MSI caused by the formation of PtO_2 species instead of Pt–O–Ce ensembles. The formation
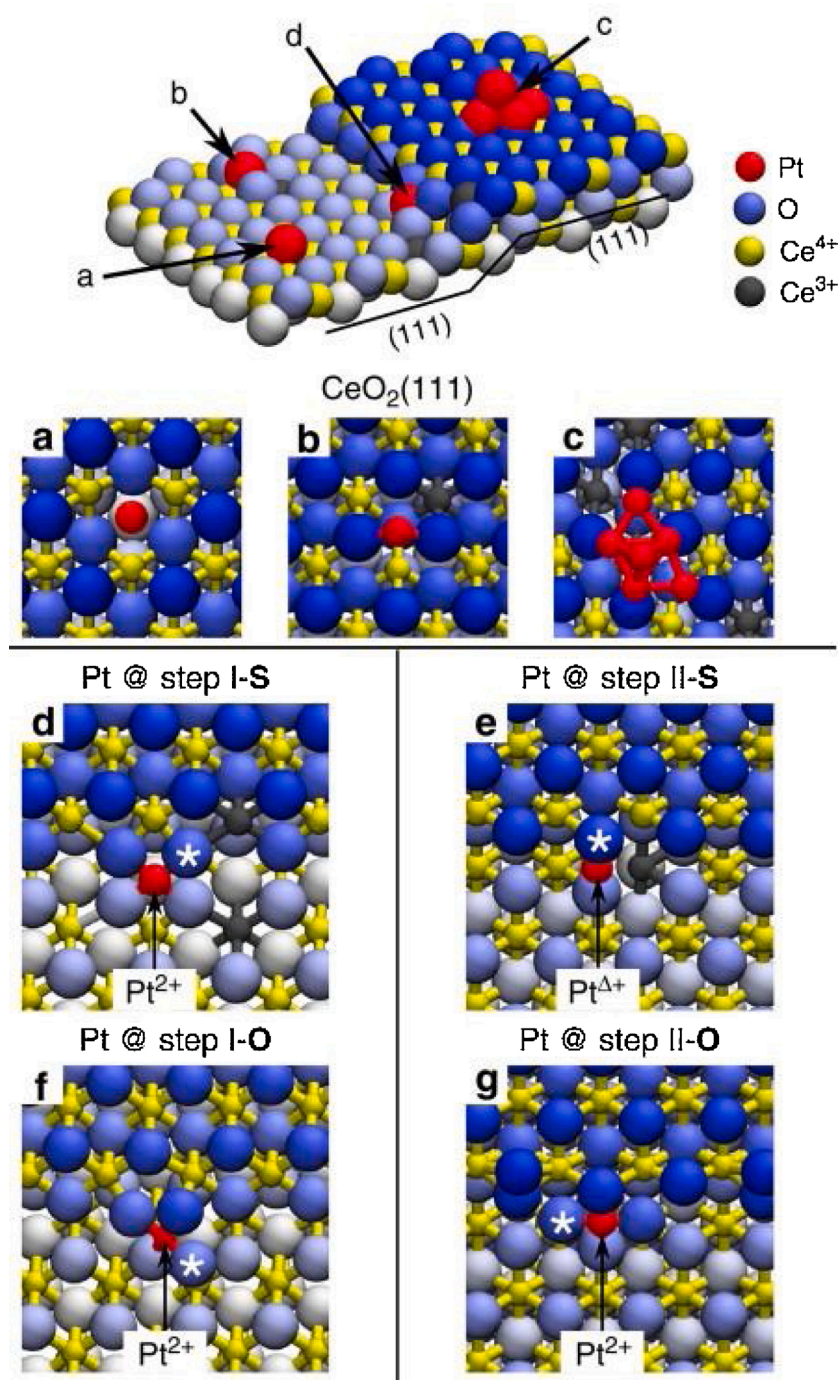
Fig. 26. Pt adsorption sites on the CeO₂(111) surface obtained from DFT calculations. (a) Pt adatom in a surface O vacancy, (b) on the stoichiometric CeO₂(111) terrace and (c) supported Pt₆ cluster. (d) Pt adatom at the stoichiometric step I (step I—S) and (e) at the stoichiometric step II (step II—S). (f) Pt adatom at the step I with excess O (step I—O) and (g) at the step II with excess O (step II—O). (d–g) The * symbol denotes the O atom removed to calculate the O vacancy formation energy. Reproduced with permission from Ref. [288]. Copyright Nature Publishing group.

of the terrace sites over large Pt NPs was shown to contribute to the improved CO oxidation performance [100]. To deepen the understanding of the roles played by oxidized Pt species, the PtO₂ and PtO₂–CeO₂ powders were treated in air and showed that at 600 °C, PtO₂ powder yielded Pt and Pt₃O₄ phases, while PtO₂–CeO₂ decomposition mostly produced Pt₃O₄ [294]. The specific role of the Pt₃O₄ phase remains unclear.

It is noteworthy that that H₂ pretreatment of the nanosized Pt species yielded well-dispersed ceria-uncovered NPs to ensure the RT catalyst activity due to the strong MSI controlled by the Pt–O bond elongation [96]. At the same time, the competition between the formation of Pt–O and Pt–Pt bonds was mentioned [183], with the SMSI being caused by ceria reducibility. Size dependence of the morphology was attributed to

Pt–Pt interaction in the cluster and the Pt–O interaction between the cluster and CeO₂(111) surface [187].

The effect of the Pt loading on the MSI strength was recently shown [295]. The resistant behavior of 0.1 %Pt/CeO₂ catalysts to reduction and sintering up to 500 °C was shown along with their weak interactions with CO, while higher Pt loadings led to difficult-to-detect sub-nanometer Pt structures that exerted strong interactions with CO and low sintering resistance (Fig. 27).

The effects of electron transfer in the Ptₙ/CeO₂(111) catalysts (n = 95; 122) were considered [296]. The Pt–CeO₂ interaction reconstructed the interface-forming Pt nanofacets and shifted the valence Pt d-states to affect the electronic structure of the interfacial oxygen anions (Fig. 28). In single-atom Pt/CeO₂(100) catalyst [171], the dynamically
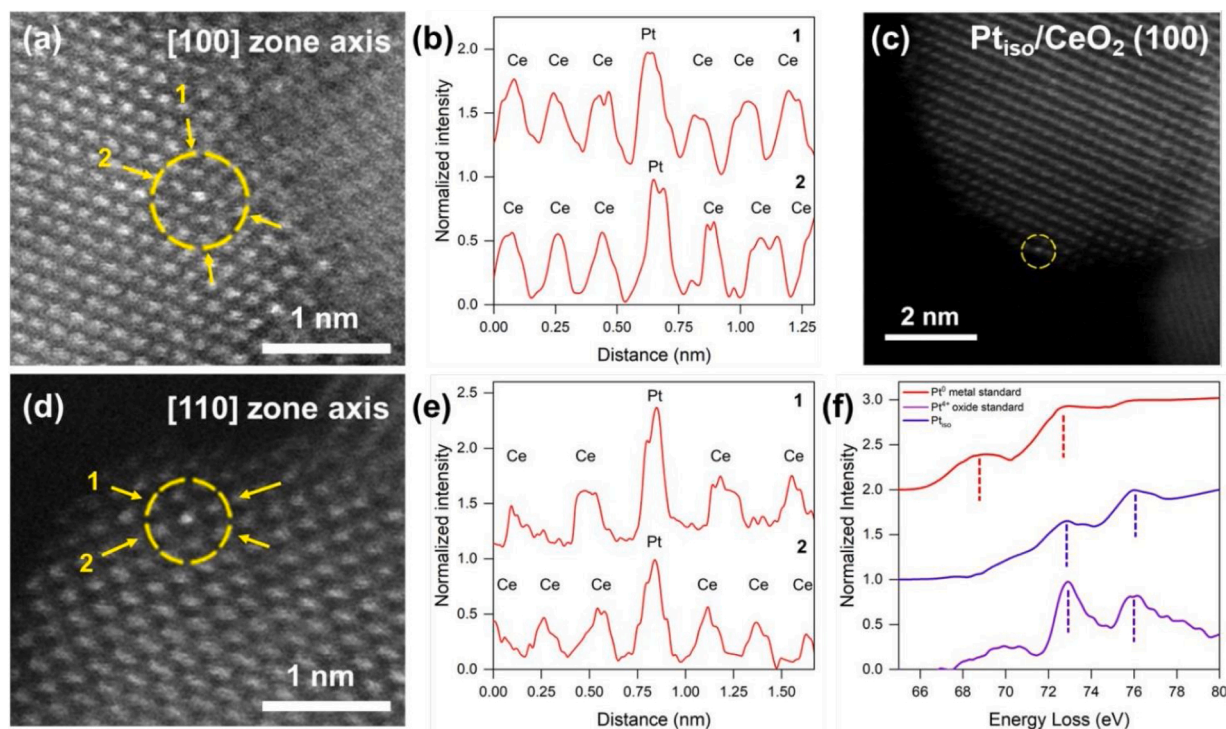
Fig. 27. Atomic scale structure of Pt$_{iso}$ on CeO$_2$ revealed by STEM imaging. a) An ex situ HAADF-STEM image of Pt$_{iso}$/CeO$_2$ following reduction at 250 °C along the [100] zone axis of CeO$_2$. The yellow circles highlight the Pt single atoms in this and other images in the figure. b) Normalized intensity profiles taken along the lines indicated by the yellow arrows and numbered in a. c) HAADF-STEM image of a CeO$_2$ (111) termination showing Pt sitting at the oxide surface. d,e) Image and linescans taken along the CeO$_2$ [110] zone axis. f) Pt N edge electron energy loss spectroscopy of Pt$_{iso}$ with respect to measured Pt° and Pt^{4+} standards. Reproduced with permission from Ref. [295]. Copyright American Chemical Society. (For interpretation of the references to colour in this figure legend, the reader is referred to the web version of this article.)

interconnected coexisting charge states that participate in strong MSIs were shown to be connected with the phonon-assisted electron injection/recovery of Ce4f and Pt states, where Ce4f states adjust the surface atom displacement.

It is noteworthy that the term "metal–support interaction" is now in vogue in catalysis science when one needs to explain the experimentally observed enhancement in catalyst performance, and Pt/CeO$_2$ environmental catalysts are not the exception. At the same time, not all publications provide adequate proofs for the existence of such interaction in the systems under consideration. It seems that a solid indicator is

required to qualitatively estimate the MSI strength. This will allow more precisely controlling the Pt–CeO$_2$ interaction experimentally as well as accounting for the effects of promoters, modifiers, and supports and support/catalyst treatment procedures to compare the catalysts with different compositions. Other aspects that should be clarified are connected with the competition between the Pt–ceria interaction and the Pt (or ceria)–substrate interaction and derived effects on the MSI strength.
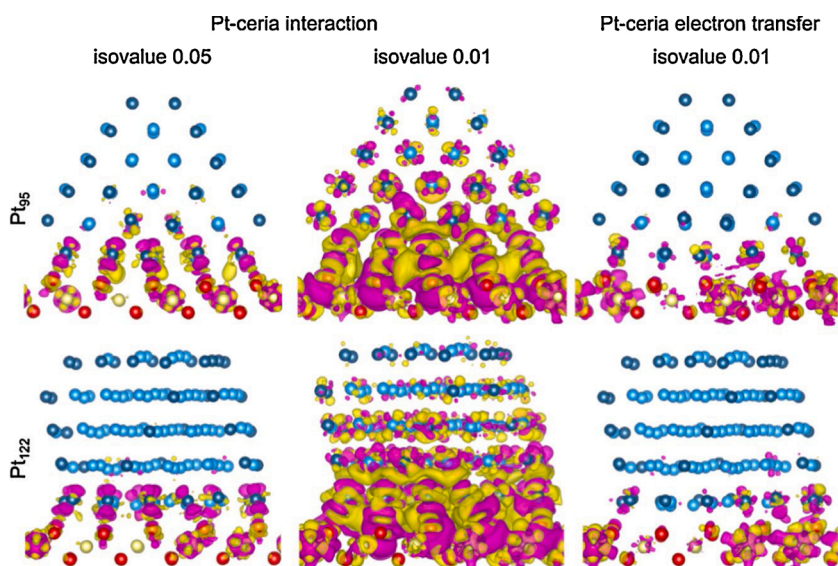
Fig. 28. Isosurfaces of charge density difference for the interaction between ceria and the considered Pt particles involving the transfer of 6 electrons plotted at different isovalues (in a.u.) as well as the distilled contribution of Pt-ceria electron transfer to the electron polarization. Regions of electron accumulation (depletion) are colored yellow (pink). (Edge) Pt atoms are (dark) blue, O atoms are red, Ce cations are beige. Reproduced with permission from Ref. [296]. Copyright Elsevier. (For interpretation of the references to colour in this figure legend, the reader is referred to the web version of this article.)

7. Conclusions and outlook

The Pt/CeO$_2$ catalysts and Pt–CeO$_x$ interfaces have found diverse applications in environmental catalysis. This was caused by the high compatibility and synergy of Pt and ceria to activate and purposefully transform chemicals into value-added products. A number of techniques, such as plasma treatment, were shown to contribute to the formation of the desired defective structure solely or in combination with other pretreatment procedures (e.g., H$_2$ treatment) imposed on the support or catalyst. A complex of experimental and theoretical methods allowed specifying the peculiarities of formation of the active surface of the composites, with the particular efforts being given to Pt coordination, the effect of ceria facets, and defective surface. In Pt/CeO$_2$ composites, the high efficiency of Pt utilization was achieved due to the single-atom configuration and suitable ceria morphology, while in some reactions the formation of the single-atom Pt species did not result in significant activity enhancement.

To further enhance the performance, the composition of the Pt/CeO$_2$ catalysts was modified to a large extent. Stability issues were addressed using additional supports (alumina, silica, titania, zirconia, etc.) that affected the redox, acid-base, and other surface properties of catalysts. Various promoters (Sn, Zr, La, Yb, Y, etc.) were also proposed for such systems. The organization of the Pt–CeO$_2$ interfaces in the catalysts that already contain Pt or ceria as a component was shown to be rather beneficial and can be used as a way of the catalyst intensification.

Large progress in the understanding of Pt–CeO$_2$ interfaces and their roles in catalytic reactions forms the basis for further research. The following key directions can be elaborated:

(1) To enhance the catalyst performance and overcome their current drawbacks and limitations, new strategies for the facile, robust, and source-efficient synthesis of environmental catalysts utilizing Pt–CeO$_x$ interfaces are required. The influence of the order of components introduction, combined treatment procedures, Pt (re)dispersion can be further developed. For single-atom catalysts, the homogeneous distribution and stabilization of the Pt species are of particular interest. The approaches to organizing the compatible tailor-made defect structure on the surface of ceria with the predetermined morphology are also required. To confirm the high catalyst stability, the testing of the developed composites should be also carried out under the simulated real exhaust conditions paying attention to the probable effects of humidity and poisoning.

(2) To ensure the catalyst robustness, the new generation of composites can be prepared by using new types of precursors of Pt (e.g., organo multimetallic complexes) and Ce (e.g., Ce-based- or functionalized MOFs, including MOF-on-MOF configurations) along with the high-surface ordered supports (3DOM, SBA-15, etc.). The specific roles of surface groups (e.g., hydroxyls, NH$_2$-, PtO$_x$, CeO$_x$, etc.) should be specified for these cases. The comprehensive experimental and theoretical work will be required to reveal the component distribution within such composites as well as the action of each component in specific transformations during the catalytic reaction.

(3) Advanced surface science studies will be required to clarify the questions related to intrinsic activities of several Pt species of different sizes (e.g., single-atom species and Pt NPs) coexisting on the ceria surface. Additionally, the issues of nucleation, agglomeration, coalescence, sintering, and restructuring of Pt species will require close attention given the role of the substrate molecule. The mechanisms of ceria surface restructuring induced by "immersion" of Pt species are also of interest.

(4) The roles of promoters and modifiers both for ceria support (Zr, Sn, etc.) and Pt component (Au, Ag, Ni, Fe, etc., to form bimetallic, trimetallic or multimetallic composites) in the formation of active sites and, generally, in catalyst performance of Pt/CeO$_2$ catalysts in various reactions is topical and requires additional systematic studies since it has a high potential in environmental catalysis.

(5) Coexistence, interplay, and synergistic action of multiple surface defects and active surface ensembles related to Pt, CeO$_2$, Pt–CeO$_2$ interfaces as well as their interfaces with promoters/modifiers/supports, requires sophisticated surface science and theoretical studies. The morphology and facet effects should also be taken into account.

(6) To provide the opportunities for the quantitative comparison of various Pt-CeO$_2$-based catalyst formulations in terms of the metal–support interaction strength, the indicator is required.

All this will allow rational experimental and in silico design of new generations of composites utilizing Pt–CeO$_2$ interfaces for existing and new catalytic processes that will demonstrate high durability and catalytic efficiency. General tendency to reduce the content of expensive noble metals, including Pt, in the catalysts with the opportunity to enhance the Pt activity by controlling its state, high dispersity, cooperation with ceria active sites as well as the addition of the second, less expensive, component (e.g., Ag, Ni, Fe, etc.) unlocks new potential for the use of Pt–CeO$_2$-based composites in environmental catalysis.

Declaration of Competing Interest

The authors declare that they have no known competing financial interests or personal relationships that could have appeared to influence the work reported in this paper.

Acknowledgements

References

[1] T. Montini, M. Melchionna, M. Monai, P. Fornasiero, Fundamentals and catalytic applications of CeO$_2$-based materials, Chem. Rev. 116 (2016) 5987–6041, https://doi.org/10.1021/acs.chemrev.5b00603.

[2] J.A. Rodriguez, D.C. Grinter, Z. Liu, R.M. Palomino, S.D. Senanayake, Ceria-based model catalysts: fundamental studies on the importance of the metal–ceria interface in CO oxidation, the water–gas shift, CO$_2$ hydrogenation, and methane and alcohol reforming, Chem. Soc. Rev. 46 (2017) 1824–1841, https://doi.org/10.1039/c6cs00863a.

[3] V. Potin, N. Zanfoni, L. Imhoff, P. Simon, B. Domenichini, Self-supported Pt-doped ceria nanofilms directly investigated by transmission electron microscopy, Appl. Surf. Sci. 509 (2020) 145177, https://doi.org/10.1016/j.apsusc.2019.145177.

[4] W. Chen, J. Xue, Y. Bao, L. Feng, Surface engineering of nano-ceria facet dependent coupling effect on Pt nanocrystals for electro-catalysis of methanol oxidation reaction, Chem. Eng. J. 381 (2020) 122752, https://doi.org/10.1016/j.cej.2019.122752.

[5] Y. Lykhach, A. Figueroba, T. Skála, T. Duchoň, N. Tsud, M. Aulická, A. Neitzel, K. Veltruská, K.C. Prince, V. Matolín, K.M. Neyman, J. Libuda, Redox-mediated conversion of atomically dispersed platinum to sub-nanometer particles, J. Mater. Chem. A 5 (2017) 9250–9261, https://doi.org/10.1039/c7ta02204b.

[6] D.V. Dao, T.D. Le, G. Adilbish, I.-H. Lee, Y.-T. Yu, Pt-loaded Au@CeO$_2$ core-shell nanocatalysts for improving methanol oxidation reaction activity, J. Mater. Chem. A 7 (2019) 26996–27006, https://doi.org/10.1039/c9ta09333h.

[7] M.J. Paulo, R.H.D. Venancio, R.G. Freitas, E.C. Pereira, A.C. Tavares, Investigation of the electrocatalytic activity for ethanol oxidation of Pt nanoparticles modified with small amount (≤5 wt%) of CeO$_2$, J. Electroanal. Chem. 840 (2019) 367–375, https://doi.org/10.1016/j.jelechem.2019.04.008.

[8] A. Mahata, A.S. Nair, B. Pathak, Recent advancements in Pt-nanostructure-based electrocatalysts for the oxygen reduction reaction, Catal. Sci. Technol. 9 (2019) 4835–4863, https://doi.org/10.1039/C9CY00895K.

[9] V.S. Pinheiro, F.M. Souza, T.C. Gentil, P. Böhnstedt, E.C. Paz, L.S. Parreira, P. Hammer, B.L. Batista, M.C. Santos, Insights in the study of the oxygen reduction reaction in direct ethanol fuel cells using hybrid platinum-ceria nanorods electrocatalysts, Chem. Electro. Chem. 6 (2019) 5124–5135, https://doi.org/10.1002/celc.201901253.

[10] J.C.S. Araújo, L.F. Oton, B. Bessa, A.B.S. Neto, A.C. Oliveira, R. Lang, L. Otubo, J. M.C. Bueno, The role of Pt loading on La$_2$O$_3$-Al$_2$O$_3$ support for methane conversion reactions via partial oxidation and steam reforming, Fuel 254 (2019) 115681, https://doi.org/10.1016/j.fuel.2019.115681.

[11] Z. Xie, B. Yan, S. Kattel, J.H. Lee, S. Yao, Q. Wu, N. Rui, E. Gomez, Z. Liu, W. Xu, L. Zhang, J.G. Chen, Dry reforming of methane over CeO₂-supported Pt-Co catalysts with enhanced activity, Appl. Catal. B. Environ. 236 (2018) 280–293, https://doi.org/10.1016/j.apcatb.2018.05.035.

[12] U. Amjad, C.W.M. Quintero, G. Ercolino, C. Italiano, A. Vita, S. Specchia, Methane steam reforming on the Pt/CeO₂ Catalyst: effect of daily start-up and shut-down on long-term stability of the catalyst, Ind. Eng. Chem. Res. 58 (2019) 16395–16406, https://doi.org/10.1021/acs.iecr.9b02436.

[13] N.A.K. Aramouni, J.G. Touma, B.A. Tarboush, J. Zeaiter, M.N. Ahmad, Catalyst design for dry reforming of methane: analysis review, Renewable Sustainable Energy Rev. 82 (2018) 2570–2585, https://doi.org/10.1016/j.rser.2017.09.076.

[14] W.-J. Jang, J.-O. Shim, H.-M. Kim, S.-Y. Yoo, H.-S. Roh, A review on dry reforming of methane in aspect of catalytic properties, Catal. Today 324 (2019) 15–26, https://doi.org/10.1016/j.cattod.2018.07.032.

[15] M. Pudukudy, Z. Yaakob, Q. Jia, M. Sobri Takriff, Catalytic decomposition of undiluted methane into hydrogen and carbon nanotubes over Pt promoted Ni/CeO₂ catalysts, New J. Chem. 42 (2018) 14843–14856, https://doi.org/10.1039/c8nj02842g.

[16] M.D. Porosoff, M. Noe, Z. Myint, S. Kattel, Z. Xie, E. Gomez, P. Liu, J.G. Chen, Identifying different types of catalysts for CO₂ reduction by ethane through dry reforming and oxidative dehydrogenation, Angew. Chem. Int. Ed. 11973 (2015) 15501–15505, https://doi.org/10.1002/anie.201508128.

[17] B. Yan, X. Yang, S. Yao, J. Wan, M. Myint, E. Gomez, Z. Xie, S. Kattel, W. Xu, J.G. Chen, Dry reforming of ethane and butane with CO₂ over PtNi/CeO₂ bimetallic catalysts, ACS Catal. 6 (2016) 7283–7292, https://doi.org/10.1021/acscatal.6b02176.

[18] Z. Xie, B. Yan, J.H. Lee, Q. Wu, X. Li, B. Zhao, D. Su, L. Zhang, J.G. Chen, Effects of oxide supports on the CO₂ reforming of ethane over Pt-Ni bimetallic catalysts, Appl. Catal. B. Environ. 245 (2019) 376–388, https://doi.org/10.1016/j.apcatb.2018.12.070.

[19] L. Pastor-Perez, E.V. Ramos-Fernandez, A. Sepulveda-Escribano, Effect of the CeO₂ synthesis method on the behaviour of Pt/CeO₂ catalysis for the water-gas shift reaction, Int. J. Hydrogen Energ. 44 (2019) 21837–21846, https://doi.org/10.1016/j.ijhydene.2019.06.206.

[20] J. Papavasiliou, A. Paxinou, G. Slowik, S. Neophytides, G. Avgouropoulos, Steam reforming of methanol over nanostructured Pt/TiO₂ and Pt/CeO₂ catalysts for fuel cell applications, Catalysts 8 (2018) 544, https://doi.org/10.3390/catal8110544.

[21] A. Claudio-Piedras, R.M. Ramírez-Zamora, B.C. Alcántar-Vázquez, A. Gutiérrez-Martínez, G. Mondragón-Galicia, F. Morales-Anzures, R. Pérez-Hernández, One dimensional Pt/CeO₂-NR catalysts for hydrogen production by steam reforming of methanol: effect of Pt precursor, Catal. Today 360 (2021) 55–62, https://doi.org/10.1016/j.cattod.2019.08.013.

[22] L. Chen, K. Hou, Y. Liu, Z. Qi, Q. Zheng, Y. Lu, J. Chen, J. Chen, C. Pao, S. Wang, Y. Li, S. Xie, F. Liu, D. Prendergast, L.E. Klebanoff, V. Stavila, M.D. Allendorf, J. Guo, L. Zheng, J. Su, G.A. Somorjai, Efficient hydrogen production from methanol using a single-site Pt₁/CeO₂ Catalyst, J. Am. Chem. Soc. 141 (2019) 17995–17999, https://doi.org/10.1021/jacs.9b09431.

[23] V. Palma, C. Ruocco, E. Meloni, F. Gallucci, A. Ricca, Enhancing Pt-Ni/CeO₂ performances for ethanol reforming by catalyst supporting on high surface silica, Catal. Today 307 (2018) 175–188, https://doi.org/10.1016/j.cattod.2017.05.034.

[24] H. Dai, Y.-P. Qiu, H.-B. Dai, P. Wang, Ni-Pt/CeO₂ loaded on granular activated carbon: an efficient monolithic catalyst for controlled hydrogen generation from hydrous hydrazine, ACS Sustain. Chem. Eng. 6 (2018) 9876–9882, https://doi.org/10.1021/acssuschemeng.8b01098.

[25] J.C.S. Araújo, L.F. Oton, B. Bessa, A.B.S. Neto, A.C. Oliveira, R. Lang, L. Otubo, J.M.C. Bueno, The role of Pt loading on La₂O₃-Al₂O₃ support for methane conversion reactions via partial oxidation and steam reforming, Fuel 254 (2019) 115681, https://doi.org/10.1016/j.fuel.2019.115681.

[26] K. Vikanova, E. Redina, G. Kapustin, V. Nissenbaum, I. Mishin, E. Kostyukhin, L. Kustov, Template-free one-step synthesis of micro-mesoporous CeO₂–ZrO₂ mixed oxides with a high surface area for selective hydrogenation, Ceram. Int. 46 (2020) 13980–13988, https://doi.org/10.1016/j.ceramint.2020.02.197.

[27] K. Vikanova, E. Redina, G. Kapustin, M. Chernova, O. Tkachenko, V. Nissenbaum, L. Kustov, Advanced room-temperature synthesis of 2,5-Bis(hydroxymethyl)furan-A monomer for biopolymers-from 5-Hydroxymethylfurfural, ACS Sustain. Chem. Eng. 9 (2021) 1161–1171, https://doi.org/10.1021/acssuschemeng.0c06560.

[28] C. Lin, H. Pan, Z. Yang, X. Han, P. Tian, P. Li, Z. Xiao, J. Xu, Y.-F. Han, Effects of cerium doping on Pt-Sn/Al₂O₃ catalysts for n-heptane reforming, Ind. Eng. Chem. Res. 59 (2020) 6424–6434, https://doi.org/10.1021/acs.iecr.9b05953.

[29] Y. Long, S. Song, J. Li, L. Wu, Q. Wang, Y. Liu, R. Jin, H. Zhang, Pt/CeO₂@MOF Core@shell nanoreactor for selective hydrogenation of furfural via the channel screening effect, ACS Catal. 8 (2018) 8506–8512, https://doi.org/10.1021/acscatal.8b01851.

[30] P.D. Coan, M.B. Griffin, P.N. Ciesielski, J.W. Medlin, Phosphonic acid modifiers for enhancing selective hydrodeoxygenation over Pt catalysts: the role of the catalyst support, J. Catal. 372 (2019) 311–320, https://doi.org/10.1016/j.jcat.2019.03.011.

[31] Y. Ma, B. Chi, W. Liu, L. Cao, Y. Lin, X. Zhang, X. Ye, S. Wei, J. Lu, Tailoring of the proximity of platinum single atoms on CeO₂ using phosphorus boosts the hydrogenation activity, ACS Catal. 9 (2019) 8404–8412, https://doi.org/10.1021/acscatal.9b01536.

[32] L. Chen, I.S. Ali, G.E. Sterbinsky, J.T.L. Gamler, S.E. Skrabalak, S.L. Tait, Alkene hydrosilylation on oxide-supported Pt-ligand single-site catalysts, Chem. Cat. Chem. 11 (2019) 2843–2854, https://doi.org/10.1002/cctc.201900530.

[33] W.H. Saputera, J.A. Scott, D. Friedmann, R. Amal, Revealing the key oxidative species generated by Pt-loaded metal oxides under dark and light conditions, Appl. Catal. B. Environ. 223 (2018) 216–227, https://doi.org/10.1016/j.apcatb.2017.08.083.

[34] M. Mao, Y. Li, H. Lv, J. Hou, M. Zeng, L. Ren, H. Huang, X. Zhao, Efficient UV-vis-IR light-driven thermocatalytic purification of benzene on a Pt/CeO₂ nanocomposite significantly promoted by hot electron-induced photoactivation, Environ. Sci. Nano 4 (2017) 373–384, https://doi.org/10.1039/c6en00472e.

[35] Z.-Y. Zheng, D. Wang, Y. Zhang, F. Yang, X.-Q. Gong, Structures and reactivities of the CeO₂/Pt(111) reverse catalyst: a DFT+U study, Chin. J. Catal. 41 (2020) 1360–1368, https://doi.org/10.1016/S1872-2067(20)63564-1.

[36] H. Chen, Z. Huang, W. Rong, J. Zhou, Z. Xu, W. Li, Y. Lin, X. Zhou, K. Wu, Atomically resolved structure of Monolayer Ceria island on Pt(111), J. Phys. Chem. C. 124 (2020) 28531–28538, https://doi.org/10.1021/acs.jpcc.0c08303.

[37] C. Xu, Y. Wu, S. Li, J. Zhou, J. Chen, M. Jiang, H. Zhao, G. Qin, Engineering the epitaxial interface of Pt-CeO₂ by surface redox reaction guided nucleation for low temperature CO oxidation, J. Mater. Sci. Technol. 40 (2020) 39–46, https://doi.org/10.1016/j.jmst.2019.08.036.

[38] G. Gasperi, P. Luches, C. Barth, Stability of ultrathin ceria films on Pt(111) exposed to air and treated in redox cycles, J. Phys. Chem. C. 122 (2018) 25954–25963, https://doi.org/10.1021/acs.jpcc.8b07231.

[39] D.C. Grinter, M. Allan, H.J. Yang, A. Salcedo, G.E. Murgida, B.-J. Shaw, C.L. Pang, H. Idriss, M.V. Ganduglia-Pirovano, G. Thornton, Ce=O terminated CeO₂, Angew. Chem. Int. Ed. 10.1002/anie.202101771.

[40] Emission Control Catalyst Market by Metal Type (palladium, Platinum, Rhodium, and Others), Application (mobile Sources and Stationary Sources), Region (APAC, Europe, North America, MEA, South America) - Global Trends & Forecast to 2024. Markets and Markets, 2020.

[41] A. Månberger, B. Stenqvist, Global metal flows in the renewable energy transition: exploring the effects of substitutes, technological mix and development, Energy Policy 119 (2018) 226–241, https://doi.org/10.1016/j.enpol.2018.04.056.

[42] Platinum and Palladium Carbon Catalyst Market: Information by Metal (platinum Carbon Catalyst and Palladium-carbon Catalyst), End-use Industry (automotive, Chemicals, Aerospace, Pharmaceuticals and Others) and Region (North America, Europe, Latin America, Asia-pacific and Middle East & Africa) – Global Forecast Till 2024. Market Research Future, 2020.

[43] M. Konsolakis, The role of Copper–ceria interactions in catalysis science: recent theoretical and experimental advances, Appl. Catal. B. Environ. 198 (2016) 49–66, https://doi.org/10.1016/j.apcatb.2016.05.037.

[44] N.K. Soliman, Factors affecting CO oxidation reaction over nanosized materials: a review, J. Mater. Res. Technol. 8 (2019) 2395–2407, https://doi.org/10.1016/j.jmrt.2018.12.012.

[45] M.J. Kale, D. Gidcumb, F.J. Gulian, S.P. Miller, C.H. Clark, P. Christopher, Evaluation of platinum catalysts for naval submarine pollution control, Appl. Catal. B. Environ. 203 (2017) 533–540, https://doi.org/10.1016/j.apcatb.2016.10.060.

[46] C. He, J. Cheng, X. Zhang, M. Douthwaite, S. Pattisson, Z. Hao, Recent advances in the catalytic oxidation of volatile organic compounds: a review based on pollutant sorts and sources, Chem. Rev. 119 (2019) 4471–4568, https://doi.org/10.1021/acs.chemrev.8b00408.

[47] H. Huang, Y. Xu, Q. Feng, D.Y.C. Leung, Low temperature catalytic oxidation of volatile organic compounds: a review, Catal. Sci. Technol. 5 (2015) 2649–2669, https://doi.org/10.1039/C4CY01733A.

[48] L.F. Liotta, Catalytic oxidation of volatile organic compounds on supported noble metals, Appl. Catal. B. Environ. 100 (2010) 403–412, https://doi.org/10.1016/j.apcatb.2010.08.023.

[49] T. Gelles, A. Krishnamurthy, B. Adebayo, A. Rownaghi, F. Rezaei, Abatement of gaseous volatile organic compounds: a material perspective, Catal. Today 350 (2020) 3–18, https://doi.org/10.1016/j.cattod.2019.06.017.

[50] R.J. Farrauto, M. Deeba, S. Alerasool, Gasoline automobile catalysis and its historical journey to cleaner air, Nat. Catal. 2 (2019) 603–613, https://doi.org/10.1038/s41929-019-0312-9.

[51] J. Lee, J.R. Theis, E.A. Kyriakidou, Vehicle emissions trapping materials: successes, challenges, and the path forward, Appl. Catal. B. Environ. 243 (2019) 397–414, https://doi.org/10.1016/j.apcatb.2018.10.069.

[52] G. Liu, P. Gao, A review of NOₓ storage/reduction catalysts: mechanism, materials and degradation studies, Catal. Sci. Technol. 1 (2011) 552–568, https://doi.org/10.1039/c1cy00007a.

[53] D. Fino, S. Bensaid, M. Piumetti, N. Russo, A review on the catalytic combustion of soot in Diesel particulate filters for automotive applications: from powder catalysts to structured reactors, Appl. Catal. A Gen. 509 (2016) 75–96, https://doi.org/10.1016/j.apcata.2015.10.016.

[54] C.-B. Lim, H. Kusaba, H. Einaga, Y. Teraoka, Catalytic performance of supported precious metal catalysts for the combustion of diesel particulate matter, Catal. Today 175 (2011) 106–111, https://doi.org/10.1016/j.cattod.2011.03.062.

[55] A. Shukla, R.K. Singha, T. Sasaki, R. Bal, Nanocrystalline Pt-CeO₂ as an efficient catalyst for a room temperature selective reduction of nitroarenes, Green Chem. 17 (2015) 785–790, https://doi.org/10.1039/c4gc01664e.

[56] Q. Wang, Y. Li, B. Liu, Q. Dong, G. Xu, L. Zhang, J. Zhang, Novel recyclable dual-heterostructured Fe₃O₄@CeO₂/M (M = Pt, Pd and Pt-Pd) catalysts: synergetic and redox effects for superior catalytic performance, J. Mater. Chem. A 3 (2015) 139–147, https://doi.org/10.1039/c4ta05691d.

[57] N. Zhang, S. Liu, Y.-J. Xu, Recent progress on metal core@semiconductor shell nanocomposites as a promising type of photocatalyst, Nanoscale 4 (2012) 2227–2238, https://doi.org/10.1039/c2nr00009a.

[58] K. Mondal, A. Sharma, Recent advances in the synthesis and application of photocatalytic metal-metal oxide core-shell nanoparticles for environmental remediation and their recycling process, RSC Adv. 6 (2016) 83589–83612, https://doi.org/10.1039/c6ra18102c.

[59] K. Chang, H. Zhang, M. Cheng, Q. Lu, Application of ceria in CO_2 conversion catalysis, ACS Catal. 10 (2020) 613–631, https://doi.org/10.1021/acscatal.9b03935.

[60] A. Sápi, T. Rajkumar, M. Ábel, A. Efremova, A. Grósz, A. Gyuris, K.B. Ábrahámné, I. Szenti, J. Kiss, T. Varga, Á. Kukovecz, Z. Kónya, Noble-metal-free and Pt nanoparticles-loaded, mesoporous oxides as efficient catalysts for CO_2 hydrogenation and dry reforming with methane, J. CO_2 Util. 32 (2019) 106–118, https://doi.org/10.1016/j.jcou.2019.04.004.

[61] Y. Wang, H. Arandiyan, J. Scott, K.-F. Aguey-Zinsou, R. Amal, Single atom and nanoclustered Pt catalysts for selective CO_2 reduction, ACS Appl. Energy Mater. 1 (2018) 6781–6789, https://doi.org/10.1021/acsaem.8b00817.

[62] R. Ma, S. Zhang, T. Wen, P. Gu, L. Li, G. Zhao, F. Niu, Q. Huang, Z. Tang, X. Wang, A critical review on visible-light-response CeO_2-based photocatalysts with enhanced photooxidation of organic pollutants, Catal. Today 335 (2019) 20–30, https://doi.org/10.1016/j.cattod.2018.11.016.

[63] X. Hong, Y. Sun, Effect of preparation methods on the performance of Pt/CeO_2 catalysts for the catalytic oxidation of carbon monoxide, Catal. Letters 146 (2016) 2001–2008, https://doi.org/10.1007/s10562-016-1828-0.

[64] A. Jan, J. Shin, J. Ahn, S. Yang, K.J. Yoon, J.-W. Son, H. Kim, J.-H. Lee, H.-I. Ji, Promotion of Pt/CeO_2 catalyst by hydrogen treatment for low-temperature CO oxidation, RSC Adv. 9 (2019) 27002–27012, https://doi.org/10.1039/c9ra05965b.

[65] M.S. Ozório, K.F. Andriani, J.L.F. Da Silva, A hybrid-DFT investigation of the Ce oxidation state upon adsorption of F, Na, Ni, Pd and Pt on the $(CeO_2)_6$ cluster, Phys. Chem. Chem. Phys. 22 (2020) 14099–14108, https://doi.org/10.1039/c9cp07005b.

[66] R. Peng, X. Sun, S. Li, L. Chen, M. Fu, J. Wu, D. Ye, Shape effect of Pt/CeO_2 catalysts on the catalytic oxidation of toluene, Chem. Eng. J. 306 (2016) 1234–1246, https://doi.org/10.1016/j.cej.2016.08.056.

[67] H.-H. Liu, Y. Wang, A.-P. Jia, S.-Y. Wang, M.-F. Luo, J.-Q. Lu, Oxygen vacancy promoted CO oxidation over Pt/CeO_2 catalysts: a reaction at Pt–CeO_2 interface, Appl. Surf. Sci. 314 (2014) 725–734, https://doi.org/10.1016/j.apsusc.2014.06.196.

[68] Z. Xie, B. Yan, S. Kattel, J.H. Lee, S. Yao, Q. Wu, N. Rui, E. Gomez, Z. Liu, W. Xu, L. Zhang, J.G. Chen, Dry reforming of methane over CeO_2-supported Pt-Co catalysts with enhanced activity, Appl. Catal. B. Environ. 236 (2018) 280–293, https://doi.org/10.1016/j.apcatb.2018.05.035.

[69] K. Wu, L. Zhou, C.J. Jia, C.H. Yan, Pt-embedded-CeO_2 hollow spheres for enhancing CO oxidation performance, Mater. Chem. Front. 1 (2017) 1754–1763, https://doi.org/10.1039/C7QM00244K.

[70] B. Zhao, Y. Jian, Z. Jiang, R. Albilali, C. He, Revealing the unexpected promotion effect of EuO_x on Pt/CeO_2 catalysts for catalytic combustion of toluene, Chinese J. Catal. 40 (2019) 543–552, https://doi.org/S1872-2067(19)63292-4.

[71] F. Zhang, F. Yang, M. Hua, Z. Yang, H. Wei, Y. Yang, J. Wei, Buckling of two-dimensional colloidal nanoplatelets in confined space to design heterogeneous catalysts, Chem. Mater. 31 (2019) 3812–3817, https://doi.org/10.1021/acs.chemmater.9b01260.

[72] B. Wang, B. Chen, Y. Sun, H. Xiao, X. Xu, M. Fu, J. Wu, L. Chen, D. Ye, Effects of dielectric barrier discharge plasma on the catalytic activity of Pt/CeO_2 catalysts, Appl. Catal. B. Environ. 238 (2018) 328–338, https://doi.org/10.1016/j.apcatb.2018.07.044.

[73] V. Abdelsayed, A. Aljarash, M.S. El-Shall, Z. Al Othman, A.H. Alghamdi, Microwave synthesis of bimetallic nanoalloys and CO oxidation on ceria-supported nanoalloys, Chem. Mater. 21 (2009) 2825–2834, https://doi.org/10.1021/cm9004486.

[74] J. Li, Y. Tang, Y. Ma, Z. Zhang, F. Tao, Y. Qu, In situ formation of isolated bimetallic PtCe sites of single-dispersed Pt on CeO_2 for low-temperature CO oxidation, ACS Appl. Mater. Interfaces 10 (2018) 38134–38140, https://doi.org/10.1021/acsami.8b15585.

[75] H.-P. Zhou, H.-S. Wu, J. Shen, A.-X. Yin, L.-D. Sun, C.-H. Yan, Thermally stable Pt/CeO_2 hetero-nanocomposites with high catalytic activity, J. Am. Chem. Soc. 132 (2010) 4998–4999, https://doi.org/10.1021/ja101110m.

[76] E.M. Slavinskaya, A.I. Stadnichenko, V.V. Muravyov, T.Y. Kardash, E. A. Derevyannikova, V.I. Zaikovskii, O.A. Stonkus, I.N. Lapin, V.A. Svetlichnyi, A. I. Boronin, Transformation of a Pt–CeO_2 mechanical mixture of pulsed-laser-ablated nanoparticles to a highly active catalyst for carbon monoxide oxidation, Chem. Cat. Chem. 10 (2018) 2232–2247, https://doi.org/10.1002/cctc.201702050.

[77] X. Zhang, P. Yang, Y. Liu, J. Pan, D. Li, B. Wang, J. Feng, Support morphology effect on the selective oxidation of glycerol over $AuPt/CeO_2$ catalysts, J. Catal. 385 (2020) 146–159, https://doi.org/10.1016/j.jcat.2020.01.008.

[78] H. Xiong, S. Lin, J. Goetze, P. Pletcher, H. Guo, L. Kovarik, K. Artyushkova, B. M. Weckhuysen, A.K. Datye, Thermally stable and regenerable platinum–tin clusters for propane dehydrogenation prepared by atom trapping on ceria, Angew. Chem. Int. Ed. English 56 (2017) 8986–8991, https://doi.org/10.1002/anie.201701115.

[79] A.H. Samia, M.S. Mohammed, S. Faramawy, S.A. Ahmed, H.B. Ahmed, Influence of Pt nanoparticles modified by La and Ce oxides on catalytic dehydrocyclization

of n-alkanes, Egyptian J. Petrol. 24 (2015) 163–174, https://doi.org/10.1016/j.ejpe.2015.05.007.

[80] W. Wang, L. Miao, K. Wu, G. Chen, Y. Huang, Y. Yang, Hydrogen evolution in the dehydrogenation of methylcyclohexane over Pt/Ce–Mg–Al–O catalysts derived from their layered double hydroxides, Int. J. Hydrogen Energ. 44 (2019) 2918–2925, https://doi.org/10.1016/j.ijhydene.2018.12.072.

[81] F. Saad, J.D. Comparot, R. Brahmi, M. Bensitel, L. Pirault-Roy, Influence of acid-base properties of the support on the catalytic performances of Pt-based catalysts in a gas-phase hydrogenation of acetonitrile, Appl. Catal. A Gen. 544 (2017) 1–9, https://doi.org/10.1016/j.apcata.2017.06.038.

[82] J. Chen, Y. Wanyan, J. Zeng, H. Fang, Z. Li, Y. Dong, R. Qin, C. Wu, D. Liu, M. Wang, Q. Kuang, Z. Xie, L. Zheng, Surface engineering protocol to obtain an atomically dispersed Pt/CeO_2 catalyst with high activity and stability for CO oxidation, ACS Sustain. Chem. Eng. 6 (2018) 14054–14062, https://doi.org/10.1021/acssuschemeng.8b02613.

[83] F.X. Cao, S. Zhang, W. Gao, T. Cao, Y.Q. Qu, Facile synthesis of highly-dispersed Pt/CeO_2 by a spontaneous surface redox chemical reaction for CO oxidation, Catal. Sci. Technol. 8 (2018) 3233–3237, https://doi.org/10.1039/C8CY00123E.

[84] L. Artiglia, F. Orlando, K. Roy, R. Kopelent, O. Safonova, M. Nachtegaal, T. Huthwelker, J.A. van Bokhoven, Introducing time Resolution to detect catalytically active sites at the Pt/CeO_2 interface through ambient pressure X-ray photoelectron spectroscopy, J. Phys. Chem. Lett. 8 (2017) 102–108, https://doi.org/10.1021/acs.jpclett.6b02314.

[85] X. Wang, D. Liu, S. Song, H. Zhang, $Pt@CeO_2$ multicore@shell self-assembled nanospheres: clean synthesis, structure optimization, and catalytic applications, J. Am. Chem. Soc. 135 (2013) 15864–15872, https://doi.org/10.1021/ja4069134.

[86] Q. Wang, Y. Zhang, Y. Zhou, Z. Zhang, Y. Xu, C. Zhang, H. Zhang, X. Sheng, Preparation of platinum nanoparticles immobilized on ordered mesoporous Co_3O_4–CeO_2 composites and their enhanced catalytic activity, RSC Adv. 6 (2016) 67173, https://doi.org/10.1039/c6ra08784a.

[87] R.-R. Zheng, D.-W. Feng, D. Hu, Fe_3O_4–CeO_2 heterostructure gel particles with enhanced catalytic performance for the reduction of 4-nitrophenol, Appl. Organomet. Chem. 34 (2020) e5341, https://doi.org/10.1002/aoc.5341.

[88] V.V. Denisov, Y.K. Akhmadeev, N.N. Koval, E.V. Ostroverkhov, Low-temperature plasma source based on a cold hollow-cathode ARC with increased service life, High Temp, Mater. Process. 20 (2016) 309–316, https://doi.org/10.1615/HighTempMatProc.2016019390.

[89] O.V. Krysina, V.V. Shugurov, N.A. Prokopenko, E.A. Petrikova, O.S. Tolkachev, Y. A. Denisova, Synthesis of single-layer ZrN-coatings using vacuum-arc plasma-assisted deposition with plasma flow filtering, Russ. J. Plant Physiol. 62 (2019) 848–853, https://doi.org/10.1007/s11182-019-01786-w.

[90] J. Lee, Y. Ryou, X. Chan, T.J. Kim, D.H. Kim, How Pt interacts with CeO_2 under the reducing and oxidizing environments at elevated temperature: the origin of improved thermal stability of Pt/CeO_2 compared to CeO_2, J. Phys. Chem. C. 120 (2016) 25870–25879, https://doi.org/10.1021/acs.jpcc.6b08656.

[91] K. Xi, Y. Wang, K. Jiang, J. Xie, Y. Zhou, H. Lu, Support interaction of Pt/CeO_2 and Pt/SiC catalysts prepared by nano platinum colloid deposition for CO oxidation, J. Rare Earths. 38 (2020) 376–383, https://doi.org/10.1016/j.jre.2019.07.012.

[92] A.M. Gänzler, M. Casapu, P. Vernoux, S. Loridant, F.J. Cadete Santos Aires, T. Epicier, B. Betz, R. Hoyer, J.-D. Grunwaldt, Tuning the structure of platinum particles on ceria in situ for enhancing the catalytic performance of exhaust gas catalysts, Angew. Chem. Int. Ed. English 56 (2017) 13078–13082, https://doi.org/10.1002/anie.201707842.

[93] C. Zhang, S. Li, T. Wang, G. Wu, X. Ma, J. Gong, Pt-based core-shell nanocatalysts with enhanced activity and stability for CO oxidation, Chem. Commun. 49 (2013) 10647–10649, https://doi.org/10.1039/c3cc45957h.

[94] T.Y. Kardash, E.A. Derevyannikova, E.M. Slavinskaya, A.I. Stadnichenko, V. A. Maltsev, A.V. Zaikovskii, S.A. Novopashin, A.I. Boronin, K.M. Neyman, Pt/CeO_2 and $Pt/CeSnO_x$ catalysts for low-temperature CO oxidation prepared by plasma-arc technique, Front. Chem. 7 (2019) 114, https://doi.org/10.3389/fchem.2019.00114.

[95] S. Song, Y. Wu, S. Ge, L. Wang, Y. Wang, Y. Guo, W. Zhan, Y. Guo, A facile way to improve Pt atom efficiency for CO oxidation at low temperature: modification by transition metal oxides, ACS Catal. 9 (2019) 6177–6187, https://doi.org/10.1021/acscatal.9b01679.

[96] S. Gatla, D. Aubert, G. Agostini, O. Mathon, S. Pascarelli, T. Lunkenbein, M. G. Willinger, H. Kaper, Room-temperature CO oxidation catalyst: low-temperature metal-support interaction between platinum nanoparticles and nanosized ceria, ACS Catal. 6 (2016) 6151–6155, https://doi.org/10.1021/acscatal.6b00677.

[97] L. Nie, D. Mei, H. Xiong, B. Peng, Z. Ren, X.I.P. Hernandez, A. DeLaRiva, M. Wang, M.H. Engelhard, L. Kovarik, A.K. Datye, Y. Wang, Activation of surface lattice oxygen in single-atom Pt/CeO_2 for low-temperature CO oxidation, Science 358 (2017) 1419–1423, https://doi.org/10.1126/science.aao2109.

[98] F. Morfin, T.-S. Nguyen, J.-L. Rousset, L. Piccolo, Synergy between hydrogen and ceria in Pt-catalyzed CO oxidation: an investigation on Pt–CeO_2 catalysts synthesized by solution combustion, Appl. Catal. B. Environ. 197 (2016) 2–13, https://doi.org/10.1016/j.apcatb.2016.01.056.

[99] T.A. Bugrova, T.S. Kharlamova, A.S. Savel'eva, V.A. Svetlichnyi, M.A. Salaev, G. V. Mamontov, Insights into formation of Pt species in Pt/CeO_2 Catalysts: effect of treatment conditions and metal-support interaction, Catal. Today (2020), https://doi.org/10.1016/j.cattod.2020.04.039. In Press, Corrected Proof.

[100] J. Lee, Y. Ryou, J. Kim, X. Chan, T.J. Kim, D.H. Kim, Influence of the defect concentration of ceria on the Pt dispersion and the CO oxidation activity of Pt/CeO₂, J. Phys. Chem. C. 122 (2018) 4972–4983, https://doi.org/10.1021/acs.jpcc.8b00254.

[101] J. Ke, W. Zhu, Y. Jiang, R. Si, Y.-J. Wang, S.-C. Li, C. Jin, H. Liu, W.-G. Song, C.-H. Yan, Y.-W. Zhang, Strong local coordination structure effects on subnanometer PtOₓ clusters over CeO₂ nanowires probed by low-temperature CO oxidation, ACS Catal. 59 (2015) 5164–5173, https://doi.org/10.1021/acscatal.5b00832.

[102] N. Singhania, E.A. Anumol, N. Ravishankar, G. Madras, Influence of CeO₂ morphology on the catalytic activity of CeO₂-Pt hybrids for CO oxidation, Dalton Trans. 42 (2013) 15343, https://doi.org/10.1039/c3dt51364e.

[103] P.E. Plyusnin, E.M. Slavinskaya, R.M. Kenzhin, A.K. Kirilovich, E.V. Makotchenko, O.A. Stonkus, Y.V. Shubin, A.A. Vedyagin, Synthesis of bimetallic AuPt/CeO₂ catalysts and their comparative study in CO oxidation under different reaction conditions, React. Kinet. Mech. Catal. 127 (2019) 69–83, https://doi.org/10.1007/s11144-019-01545-5.

[104] S.S. Punde, B.J. Tatarchuk, Pt-CeO₂/SiO₂ catalyst for CO oxidation in humid air at ambient temperature, Chin. J. Catal. 38 (2017) 475–488, https://doi.org/10.1016/S1872-2067(17)62749-9.

[105] W. Tang, X. Lu, F. Liu, S. Du, J. Weng, S. Hoang, S. Wang, C.-Y. Nam, P.-X. Gao, Ceria-based nanoflake arrays integrated on 3D cordierite honeycombs for efficient low-temperature diesel oxidation catalyst, Appl. Catal. B. Environ. 245 (2019) 623–634, https://doi.org/10.1016/j.apcatb.2019.01.028.

[106] X. Yang, X. Cheng, J. Ma, Y. Zou, W. Luo, Y. Deng, Large-pore mesoporous CeO₂–ZrO₂ solid solutions with in-pore confined Pt nanoparticles for enhanced CO oxidation, Small 15 (2019) 1903058, https://doi.org/10.1002/smll.201903058.

[107] J.H. Park, H. Noh, T.S. Chang, C.-H. Shin, Low-temperature CO oxidation of Pt/Al₀.₁Ce₀.₉Oₓ catalysts: effects of supports prepared with different precipitants, Korean J. Chem. Eng. 35 (2018) 645–653, https://doi.org/10.1007/s11814-017-0343-3.

[108] A.M. Gänzler, M. Casapu, F. Maurer, H. Störmer, D. Gerthsen, G. Ferré, P. Vernoux, B. Bornmann, R. Frahm, V. Murzin, M. Nachtegaal, M. Votsmeier, J.-D. Grunwaldt, Tuning the Pt/CeO₂ interface by in situ variation of the Pt particle size, ACS Catal. 8 (2018) 4800–4811, https://doi.org/10.1021/acscatal.8b00330.

[109] J. Jin, C. Li, C. Tsang, B. Xu, C. Liang, Catalytic combustion of methane over Pt–Ce oxides under scarce oxygen condition, Ind. Eng. Chem. Res. 55 (2016) 2293–2301, https://doi.org/10.1021/acs.iecr.5b04202.

[110] A. Gremminger, P. Lott, M. Merts, M. Casapu, J.-D. Grunwaldt, O. Deutschmann, Sulfur poisoning and regeneration of bimetallic Pd-Pt methane oxidation catalysts, Appl. Catal. B. Environ. 218 (2017) 833–843, https://doi.org/10.1016/j.apcatb.2017.06.048.

[111] Z. Abbasi, M. Haghighi, E. Fatehifar, S. Saedy, Synthesis and physicochemical characterizations of nanostructured Pt/Al₂O₃-CeO₂ catalysts for total oxidation of VOCs, J. Hazard. Mater. 186 (2011) 1445–1454, https://doi.org/10.1016/j.jhazmat.2010.12.034.

[112] J. Zheng, Z. Wang, Z. Chen, S. Zuo, Mechanism of CeO₂ synthesized by thermal decomposition of Ce-MOF and its performance of benzene catalytic combustion, J. Rare Earths (2020) https://doi.org/10.1016/j.jre.2020.08.009. In Press, Corrected Proof.

[113] S.M. Saqer, D.I. Kondarides, X.E. Verykios, Catalytic activity of supported platinum and metal oxide catalysts for toluene oxidation, Top. Catal. 52 (2009) 517–527, https://doi.org/10.1007/s11244-009-9182-8.

[114] B. Chen, B. Wang, Y. Sun, X. Wang, M. Fu, J. Wu, L. Chen, Y. Tan, D. Ye, Plasma-assisted surface interactions of Pt/CeO₂ catalyst for enhanced toluene catalytic oxidation, Catalysts 9 (2019) 2, https://doi.org/10.3390/catal9010002.

[115] R. Peng, S. Li, X. Sun, Q. Ren, L. Chen, M. Fu, J. Wu, D. Ye, Size effect of Pt nanoparticles on the catalytic oxidation of toluene over Pt/CeO₂ catalysts, Appl. Catal. B. Environ. 220 (2018) 462–470, https://doi.org/10.1016/j.apcatb.2017.07.048.

[116] F. Rahmani, M. Haghighi, P. Estifaee, Synthesis and characterization of Pt/Al₂O₃–CeO₂ nanocatalyst used for toluene abatement from waste gas streams at low temperature: conventional vs. Plasma–ultrasound hybrid synthesis methods, Microporous Mesoporous Mater. 185 (2014) 213–223, https://doi.org/10.1016/j.micromeso.2013.11.019.

[117] Y. Yang, G. Wang, P. Zheng, F. Dang, J. Han, Carbon deposits during catalytic combustion of toluene on Pd–Pt-based catalysts, Catal. Sci. Technol. 10 (2020) 2452–2461, https://doi.org/10.1039/D0CY00101E.

[118] A.R. Supandi, N. Nunotani, N. Imanaka, Complete phenol removal in liquid-phase under moderate condition over Pt/CeO₂-ZrO₂-SnO₂/ZrO₂/SBA-16 catalysts, Func. Mater. Lett. 13 (2020) 2050030, https://doi.org/10.1142/S1793604720500307.

[119] Z. Yan, Z. Xu, J. Yu, M. Jaronie, Enhanced formaldehyde oxidation on CeO₂/AlOOH-supported Pt catalyst at room temperature, Appl. Catal. B. Environ. 199 (2016) 458–465, https://doi.org/10.1016/j.apcatb.2016.06.052.

[120] Z. Yan, S. Gong, L. An, L. Yue, Z. Xu, Enhanced catalytic activity of graphene oxide/CeO₂ supported Pt toward HCHO decomposition at room temperature, Reac. Kinet. Mech. Cat. 124 (2018) 293–304, https://doi.org/10.1007/s11144-018-1348-6.

[121] K. Fuku, M. Goto, T. Sakano, T. Kamegawa, K. Mori, H. Yamashita, Efficient degradation of CO and acetaldehyde using nano-sized Pt catalysts supported on CeO₂ and CeO₂/ZSM-5 composite, Catal. Today 201 (2013) 57–61, https://doi.org/10.1016/j.cattod.2012.04.034.

[122] K. Inoue, S. Somekawa, VOCs treatment with Pt/Co₃O₄–CeO₂ catalyst, Chem. Eng. Technol. 42 (2019) 257–260, https://doi.org/10.1002/ceat.201800245.

[123] Z. El Assal, S. Ojala, S. Pitkäaho, L. Pirault-Roy, B. Darif, J.-D. Comparot, M. Bensitel, R.L. Keiski, R. Brahmi, Comparative study on the support properties

[124] in the total oxidation of dichloromethane over Pt catalysts, Chem. Eng. J. 313 (2017) 1010–1022, https://doi.org/10.1016/j.cej.2016.10.139.

[124] T.K. Nevanperä, S. Pitkäaho, S. Ojala, R.L. Keiski, Oxidation of dichloromethane over Au, Pt, and Pt-Au containing catalysts supported on γ-Al₂O₃ and CeO₂-Al₂O₃, Molecules 25 (2020), 4644, https://doi.org/10.3390/molecules25204644.

[125] Y. Shi, Z. Li, J. Wang, R. Zhou, Synergistic effect of Pt/Ce and USY zeolite in Pt-based catalysts with high activity for VOCs degradation, Appl. Catal. B. Environ. 286 (2021) 119936, https://doi.org/10.1016/j.apcatb.2021.119936.

[126] X. Zhang, L. Dai, Y. Liu, J. Deng, L. Jing, X. Yu, Z. Han, K. Zhang, H. Dai, 3DOM CeO₂-supported Ru: YM (M = Au, Pd, Pt) alloy nanoparticles with improved catalytic activity and chlorine-tolerance in trichloroethylene oxidation, Catal. Sci. Technol. 10 (2020) 3755–3770, https://doi.org/10.1039/d0cy00681e.

[127] Y. Gu, S. Shao, W. Sun, H. Xia, X. Gao, Q. Dai, W. Zhan, X. Wang, The oxidation of chlorinated organic compounds over W-modified Pt/CeO₂ catalysts, J. Catal. 380 (2019) 375–386, https://doi.org/10.1016/j.jcat.2019.06.041.

[128] C. Wang, S. Mao, Z. Wang, Y. Chen, W. Yuan, Y. Ou, H. Zhang, Y. Gong, Y. Wang, B. Mei, Z. Jiang, Insight into single-atom-induced unconventional size dependence over CeO₂-supported Pt catalysts, Chemistry 6 (2020) 752–765, https://doi.org/10.1016/j.chempr.2019.12.029.

[129] J.S. Du, T. Bian, J. Yu, Y. Jiang, X. Wang, Y. Yan, Y. Jiang, C. Jin, H. Zhang, D. Yang, Embedding ultrafine and high-content Pt nanoparticles at ceria surface for enhanced thermal stability, Adv. Sci. 4 (2017) 1700056, https://doi.org/10.1002/advs.201700056.

[130] Q. Wang, Y. Zhang, Y. Zhou, Z. Zhang, J. Xue, Y. Xu, C. Zhang, X. Sheng, N. Kui, Nanocasting synthesis of an ordered mesoporous CeO₂-supported Pt nanocatalyst with enhanced catalytic performance for the reduction of 4-nitrophenol, RSC Adv. 6 (2015) 730–739, https://doi.org/10.1039/c5ra23472g.

[131] S. Yuan, Y. Gao, J. Bao, Y. Zhang, W. Chen, J. Fang, Y. Zhou, Y. Wang, W. Zhu, Preparation of disk-like Pt/CeO₂-p-TiO₂ catalyst derived from MIL-125(Ti) for excellent catalytic performance, Appl. Organomet. Chem. 32 (2018) e4395, https://doi.org/10.1002/aoc.4395.

[132] J. Zhang, G. Chen, D. Guay, M. Chaker, D. Ma, Highly active PtAu alloy nanoparticle catalysts for the reduction of 4-nitrophenol, Nanoscale. 6 (2014) 2125–2130, https://doi.org/10.1039/c3nr04715f.

[133] T.S. Kharlamova, M.V. Salina, V.A. Svetlichnyi, M.A. Salaev, G.V. Mamontov, CeO₂-supported Pt–Ag bimetallic catalysts for 4-nitrophenol reduction, Catal. Today (2021). Under review.

[134] A.C. Oliveira, D.C. Carvalho, H.S.A. De Souza, J.M. Filho, A.C. Oliveira, A. Campos, É.R.C. Milet, F.F. De Sousa, E. Padron-Hernandez, A study on the modification of mesoporous mixed oxides supports for dry reforming of methane by Pt or Ru, Appl. Catal. A Gen. 473 (2014) 132–145, https://doi.org/10.1016/j.apcata.2013.12.031.

[135] S. Damyanova, B. Pawelec, K. Arishtirova, M.V.M. Huerta, J.L.G. Fierro, The effect of CeO₂ on the surface and catalytic properties of Pt/CeO₂-ZrO₂ catalysts for methane dry reforming, Appl. Catal. B. Environ. 89 (2009) 149–159, https://doi.org/10.1016/j.apcatb.2008.11.035.

[136] D.G. Araiza, D.G. Arcos, A. Gómez-Cortés, G. Díaz, Dry reforming of methane over Pt-Ni/CeO₂ catalysts: effect of the metal composition on the stability, Catal. Today. In press. (2019), https://doi.org/10.1016/j.cattod.2019.06.018.

[137] A. Jawad, F. Rezaei, A.A. Rownaghi, Highly efficient Pt/Mo-Fe/Ni-based Al₂O₃-CeO₂ catalysts for dry reforming of methane, Catal. Today 350 (2020) 80–90, https://doi.org/10.1016/j.cattod.2019.06.004.

[138] R.O. da Fonseca, R.C. Rabelo-Neto, R.C.C. Simoes, L.V. Mattos, F.B. Noronha, Pt supported on doped CeO₂/Al₂O₃ as catalyst for dry reforming of methane, Int. J. Hydrogen Energ. 45 (2020) 5182–5191, https://doi.org/10.1016/j.ijhydene.2019.09.207.

[139] G. Ferré, M. Aouine, F. Bosselet, L. Burel, F.J. Cadete Santos Aires, C. Geantet, S. Ntais, F. Maurer, M. Casapu, J.-D. Grunwaldt, T. Epicier, S. Loridant, P. Vernoux, Exploiting the dynamic properties of Pt on ceria for low-temperature CO oxidation, Catal. Sci. Technol. 10 (2020) 3904–3917, https://doi.org/10.1039/d0cy00732c.

[140] M.V. Grabchenko, G.V. Mamontov, V.I. Zaikovskii, V. La Parola, L.F. Liotta, O.V. Vodyankina, The role of metal–support interaction in Ag/CeO₂ catalysts for CO and soot oxidation, Appl. Catal. B. Environ. 260 (2020) 118148, https://doi.org/10.1016/j.apcatb.2019.118148.

[141] P. Wang, J. Yi, C. Sun, P. Luo, L. Lei, Evaluation of H₂ influence on the evolution mechanism of NOₓ storage and reduction over Pt–Ba–Ce/γ-Al₂O₃ catalysts, Engineering 5 (2019) 568–575, https://doi.org/10.1016/j.eng.2019.02.005.

[142] L. Roiban, S. Koneti, F. Morfin, T.-S. Nguyen, P. Mascunan, M. Aouine, T. Epicier, L. Piccolo, Uncovering the 3D structure of combustion-synthesized noble metal-ceria nanocatalysts, Chem. Cat. Chem. 9 (2017) 4607–4613, https://doi.org/10.1002/cctc.201701474.

[143] R. Schmitt, A. Nenning, O. Kraynis, R. Korobko, A.I. Frenkel, I. Lubomirsky, S.M. Hailef, J.L.M. Rupp, A review of defect structure and chemistry in ceria and its solid solutions, Chem. Soc. Rev. 49 (2020) 554–592, https://doi.org/10.1039/C9CS00588A.

[144] K. Wu, L. Zhou, C.J. Jia, C.H. Yan, Pt-embedded-CeO₂ hollow spheres for enhancing CO oxidation performance, Mater. Chem. Front. 1 (2017) 1754–1763, https://doi.org/10.1039/C7QM00244K.

[145] S. Gatla, D. Aubert, V. Flaud, R. Grosjean, T. Lunkenbein, O. Mathon, S. Pascarelli, H. Kaper, Facile synthesis of high-surface area platinum-doped ceria for low temperature CO oxidation, Catal. Today 333 (2019) 105–112, https://doi.org/10.1016/j.cattod.2018.06.032.

[146] P. Simon, N. Zanfoni, L. Avril, Z. Li, V. Potin, B. Domenichini, S. Bourgeois, Nanoporous platinum doped cerium oxides thin films grown on silicon substrates:

ionic platinum localization and stability, Adv. Mater. Interfaces 4 (2017) 1600821, https://doi.org/10.1002/admi.201600821.

[147] Z. Yang, Effect of platinum precursor type on activity of Pt/CeO₂ catalyst in C₃H₈ and CO Oxidation, Int. J. Sci. Res. Innovat. Technol. 4 (2017).

[148] D. Vasilchenko, P. Topchiyan, I. Baidina, I. Korolkov, E. Filatov, V. Zvereva, P. Plyusnin, E. Slavinskaya, E. Gerasimov, Double complex salts containing [Pt(NO₃)₆]²⁻ anion and Rh(III) complex cations: Synthesis, structure and utilisation for preparing (Rh–Pt)/CeO₂ catalysts, J. Molec. Struct. 1211 (2020) 128108, https://doi.org/10.1016/j.molstruc.2020.128108.

[149] D. Vasilchenko, T. Asanova, B. Kolesov, A. Tsygankova, A. Stadnichenko, E. Slavinskaya, E. Gerasimov, K. Lomachenko, A. Boronin, S. Korenev, Cerium(III) nitrate derived CeO₂ support stabilising PtOₓ active species for room temperature CO oxidation, Chem. Cat. Chem. 12 (2020) 1413–1428, https://doi.org/10.1002/cctc.201902146.

[150] D. Vasilchenko, P. Topchiyan, S. Berdyugin, E. Filatov, S. Tkachev, I. Baidina, V. Komarov, E. Slavinskaya, A. Stadnichenko, E. Gerasimov, Tetraalkylammonium salts of platinum nitrato complexes: isolation, structure, and relevance to the preparation of PtOₓ/CeO₂ catalysts for low-temperature CO oxidation, Inorg. Chem. 58 (2019) 6075–6087, https://doi.org/10.1021/acs.inorgchem.9b00370.

[151] Z. Abdelouahab-Reddam, R. El Mail, F. Coloma, A. Sepúlveda-Escribano, Effect of the metal precursor on the properties of Pt/CeO₂/C catalysts for the total oxidation of ethanol, Catal. Today 249 (2015) 109–116, https://doi.org/10.1016/j.cattod.2014.11.024.

[152] G. Li, L. Li, Highly efficient formaldehyde elimination over meso-structured M/CeO₂ (M = Pd, Pt, Au and Ag) catalyst under ambient conditions, RSC Adv. 5 (2015) 36428–36433, https://doi.org/10.1039/c5ra04928h.

[153] E.A. Redina, K.V. Vikanova, G.I. Kapustin, I.V. Mishin, O.P. Tkachenko, L.M. Kustov, Selective room-temperature hydrogenation of carbonyl compounds under atmospheric pressure over platinum nanoparticles supported on ceria-zirconia mixed oxide, Europ. J. Org. Chem. 26 (2019) 4159–4170, https://doi.org/10.1002/ejoc.201900215.

[154] I.Yu. Kaplin, E.S. Lokteva, E.V. Golubina, V.V. Lunin, Template synthesis of porous ceria-based catalysts for environmental application, Molecules 25 (2020) 4242. https://doi.org/10.3390/molecules25184242.

[155] X. Zhu, H. He, Y. Li, H. Wu, M. Fu, D. Ye, J. Wu, H. Huang, Y. Hu, X. Niu, CeO₂-supported Pt catalysts derived from mofs by two pyrolysis strategies to improve the oxygen activation ability, Nanomaterials 10 (2020) 983, https://doi.org/10.3390/nano10050983.

[156] S. Guo, Y. Zhao, H. Yuan, C. Wang, H. Jiang, G.J. Cheng, Ultrafast laser manufacture of stable, efficient ultrafine noble metal catalysts mediated with MOF derived high density defective metal oxides, Small 16 (2020) 2000749, https://doi.org/10.1002/smll.202000749.

[157] L. Fan, K. Wang, K. Xu, Z. Liang, H. Wang, S.-F. Zhou, G. Zhan, Structural isomerism of two Ce-BTC for fabricating Pt/CeO₂ nanorods toward low-temperature CO oxidation, Small 16 (2020) 2003597, https://doi.org/10.1002/smll.202003597.

[158] Q. Wang, Y. Li, A. Serrano-Lotina, W. Han, R. Portela, R. Wang, M.A. Bañares, K.L. Yeung, Operando investigation of toluene oxidation over 1D Pt@CeO₂-derived from Pt cluster-containing MOF, J. Am. Soc. Brew. Chem. 143 (2021) 196–205, https://doi.org/10.1021/jacs.0c08640.

[159] Z. Guo, Q. You, L. Song, G. Sun, G. Chen, C. Li, X. Yang, X. Hu, X. Jiang, Highly dispersed Pt species anchored onto NH₂-Ce-MOFs and their derived mesoporous catalysts for CO oxidation, Nanoscale 13 (2021) 117–123, https://doi.org/10.1039/d0nr05626j.

[160] L. Liu, A. Corma, Metal catalysts for heterogeneous catalysis: from single atoms to nanoclusters and nanoparticles, Chem. Rev. 118 (2018) 4981–5079, https://doi.org/10.1021/acs.chemrev.7b00776.

[161] M. Cargnello, V.V.T. Doan-Nguyen, T.R. Gordon, R.E. Diaz, E.A. Stach, R.J. Gorte, P. Fornasiero, C.B. Murray, Control of metal nanocrystal size reveals metal-support interface role for ceria catalysts, Science 341 (2013) 771–773, https://doi.org/10.1126/science.1240148.

[162] M. Monai, M. Melchionna, P. Fornasiero, Chapter one - from metal to metal-free catalysts: routes to sustainable chemistry, J. Adv. Catal. Sci. Technol. 63 (2018) 1–73, https://doi.org/10.1016/bs.acat.2018.10.001.

[163] C. Wang, X.-K. Gu, H. Yan, Y. Lin, J. Li, D. Liu, W.-X. Li, J. Lu, Water-mediated Mars-Van Krevelen mechanism for CO oxidation on ceria-supported single-atom Pt₁ catalyst, ACS Catal. 7 (2017) 887–891, https://doi.org/10.1021/acscatal.6b02685.

[164] X. Ye, H. Wang, Y. Lin, X. Liu, L. Cao, J. Gu, J. Lu, Insight of the stability and activity of platinum single atoms on ceria, Nano Res. 12 (2019) 1401–1409, https://doi.org/10.1007/s12274-019-2351-6.

[165] J. Jones, M. Xiong, A.T. DeLaRiva, E.J. Peterson, H. Pham, S.R. Challa, G. Qi, S. Oh, M.H. Wiebenga, X.I. Pereira-Hernández, Y. Wang, A.K. Datye, Thermally stable single-atom platinum-on-ceria catalysts via atom trapping, Science 353 (2016) 6295, https://doi.org/10.1126/science.aaf8800.

[166] X.I. Pereira-Hernández, A. DeLaRiva, V. Muravev, D. Kunwar, H. Xiong, B. Sudduth, M. Engelhard, L. Kovarik, E.J.M. Hensen, Y. Wang, A.K. Datye, Tuning Pt-CeO₂ interactions by high-temperature vapor-phase synthesis for improved reducibility of lattice oxygen, Nat. Commun. 10 (2019) 1358, https://doi.org/10.1038/s41467-019-09308-5.

[167] Q. Wu, J. Ba, X. Yan, J. Bao, Z. Huang, S. Dou, D. Dai, T. Tang, W. Luo, D. Meng, Insight of Pt-support interaction in S-Pt/Ce₀.₇Zr₀.₃O₂ by in situ Raman spectroscopy, Catal. Commun. 98 (2017) 34–37, https://doi.org/10.1016/j.catcom.2017.04.045.

[168] M. Kottwitz, Y. Li, R.M. Palomino, Z. Liu, G. Wang, Q. Wu, J. Huang, J. Timoshenko, S.D. Senanayake, M. Balasubramanian, D. Lu, R.G. Nuzzo, A.I. Frenkel, Local structure and electronic state of atomically dispersed Pt supported on nanosized CeO₂, ACS Catal. 9 (2019) 8738–8748, https://doi.org/10.1021/acscatal.9b02083.

[169] E.A. Derevyannikova, T. Yu, Kardash, A.I. Stadnichenko, O.A. Stonkus, E.M. Slavinskaya, V.A. Svetlichnyi, A.I. Boronin, Structural insight into strong Pt−CeO₂ interaction: from single Pt atoms to PtOₓ clusters, J. Phys. Chem. C 123 (2019) 1320–1334, https://doi.org/10.1021/acs.jpcc.8b11009.

[170] A. Figueroba, G. Kovács, A. Bruix, K.M. Neyman, Towards stable single-atom catalysts: strong binding of atomically dispersed transition metals on the surface of nanostructured ceria, Catal. Sci. Technol. 6 (2016) 6806–6813, https://doi.org/10.1039/c6cy00294c.

[171] N. Daelman, M. Capdevila-Cortada, N. López, Dynamic charge and oxidation state of Pt/CeO₂ single-atom catalysts, Nat. Mater. 18 (2019) 1215–1221, https://doi.org/10.1038/s41563-019-0444-y.

[172] M.V. Grabchenko, N.N. Mikheeva, G.V. Mamontov, M.A. Salaev, L.F. Liotta, O.V. Vodyankina, Ag/CeO₂ composites for catalytic abatement of CO, soot and VOCs, Catalysts 8 (2018) 1–36, https://doi.org/10.3390/catal8070285.

[173] Z.-Y. Zheng, D. Wang, Y. Zhang, F. Yang, X.-Q. Gong, Structures and reactivities of the CeO₂/Pt(111) reverse catalyst: a DFT+U study, Chinese J. Catal. 41 (2020) 1360–1368, https://doi.org/10.1016/S1872-2067(20)63564-1.

[174] Y. Su, Y. Wang, J. Liu, I.A.W. Filot, K. Alexopoulos, L. Zhang, V. Muravev, B. Zijlstra, D.G. Vlachos, E.J.M. Hensen, Theoretical approach to predict the stability of supported single-atom catalysts, ACS Catal. 9 (2019) 3289–3297, https://doi.org/10.1021/acscatal.9b00252.

[175] Z. Jiang, M. Jing, X. Feng, J. Xiong, C. He, M. Douthwaite, L. Zheng, W. Song, J. Liu, Z. Qu, Stabilizing platinum atoms on CeO₂ oxygen vacancies by metal-support interaction induced interface distortion: mechanism and application, Appl. Catal. B. Environ. 278 (2020) 119304, https://doi.org/10.1016/j.apcatb.2020.119304.

[176] Y. Tang, Y.-G. Wang, J. Li, Theoretical investigations of Pt₁@CeO₂ single-atom catalyst for CO oxidation, J. Phys. Chem. C 121 (2017) 11281–11289, https://doi.org/10.1021/acs.jpcc.7b00313.

[177] H. Wang, J. Liu, L.F. Allard, S. Lee, J. Liu, H. Li, J. Wang, J. Wang, S.H. Oh, W. Li, M. Flytzani-Stephanopoulos, M. Shen, B.R. Goldsmith, M. Yang, Surpassing the single-atom catalytic activity limit through paired Pt-O-Pt ensemble built from isolated Pt₁ atoms, Nat. Commun. 10 (2019) 3808, https://doi.org/10.1038/s41467-019-11856-9.

[178] G. Zhou, P. Li, Q. Ma, Z. Tian, Y. Liu, Density functional theory plus Hubbard U study of the segregation of Pt to the CeO₂₋ₓ grain boundary, Nano Lett. 18 (2018) 1668–1677, https://doi.org/10.1021/acs.nanolett.7b04680.

[179] Y.-Q. Su, L. Zhang, V. Muravev, E.J.M. Hensen, Lattice oxygen activation in transition metal doped ceria, Chinese J. Catal. 41 (2020) 977–984, https://doi.org/10.1016/S1872-2067(19)63468-6.

[180] A. Neitzel, A. Figueroba, Y. Lykhach, T. Skála, M. Vorokhta, N. Tsud, S. Mehl, K. Ševčíková, K.C. Prince, K.M. Neyman, V. Matolín, J. Libuda, Atomically dispersed Pd, Ni, and Pt species in ceria-based catalysts: principal differences in stability and reactivity, J. Phys. Chem. C 120 (2016) 9852–9862, https://doi.org/10.1021/acs.jpcc.6b02264.

[181] A. Figueroba, A. Bruix, G. Kovács, K.M. Neyman, Metal-doped ceria nanoparticles: stability and redox processes, Phys. Chem. Chem. Phys. 19 (2017) 21729–21738, https://doi.org/10.1039/c7cp02820b.

[182] C. Xie, C. Chen, Y. Yu, J. Su, Y. Li, G.A. Somorjai, P. Yang, Tandem catalysis for CO₂ hydrogenation to C₂-C₄ hydrocarbons, Nano Lett. 17 (2017) 3798–3802, https://doi.org/10.1021/acs.nanolett.7b01139.

[183] L.O. Paz-Borbón, A. López-Martínez, I.L. Garzón, A. Posada-Amarillas, H. Grönbeck, 2D-3D structural transition in sub-nanometer PtN clusters supported on CeO₂(111), Phys. Chem. Chem. Phys. 19 (2017) 17845–17855, https://doi.org/10.1039/c7cp02753b.

[184] H. Koga, A. Hayashi, Y. Ato, K. Tada, S. Hosokawa, T. Tanaka, M. Okumura, Effect of ceria and zirconia supports on NO reduction over platinum-group metal catalysts: a DFT study with comparative experiments, Catal. Today 332 (2019) 236–244, https://doi.org/10.1016/j.cattod.2018.07.023.

[185] I.Z. Koleva, H.A. Aleksandrov, G.N. Vayssilov, Influence of the adsorption of CO on the electronic structure of platinum clusters and nanowires deposited on CeO₂(111) and γ-Al₂O₃(001) surfaces, Catal. Today 357 (2020) 442–452, https://doi.org/10.1016/j.cattod.2019.07.053.

[186] I.Z. Koleva, H.A. Aleksandrov, G.N. Vayssilov, Decomposition behavior of platinum clusters supported on ceria and γ-alumina in presence of carbon monoxide, Catal. Sci. Technol. 7 (2017) 734–742, https://doi.org/10.1039/C6CY02586B.

[187] S.M.F. Shahed, A. Beniya, H. Hirata, Y. Watanabe, Morphology of size-selected Ptn clusters on CeO₂(111), J. Chem. Phys. 148 (2018) 114702, https://doi.org/10.1063/1.5017906.

[188] F.R. Negreiros, S. Fabris, Role of cluster morphology in the dynamics and reactivity of subnanometer Pt clusters supported on ceria surfaces, J. Phys. Chem. C. 118 (2014) 21014–21020, https://doi.org/10.1021/jp506404z.

[189] F. Pilger, A. Testino, A. Carino, C. Proff, A. Kambolis, A. Cervellino, C. Ludwig, Size control of Pt clusters on CeO₂ nanoparticles via an incorporation-segregation mechanism and study of segregation kinetics, ACS Catal. 6 (2016) 3688–3699, https://doi.org/10.1021/acscatal.6b00934.

[190] Y. Xin, N. Zhang, Y. Lv, J. Wang, Q. Li, Z. Zhang, From nanoparticles to single atoms for Pt/CeO₂: synthetic strategies, characterizations and applications, J. Rare Earths. 38 (2020) 850–862, https://doi.org/10.1016/j.jre.2020.03.007.

[191] A.S. Thill, A.S. Kilian, F. Bernardi, Key role played by metallic nanoparticles on the Ceria reduction, J. Phys. Chem. C. 121 (2017) 25323–25332, https://doi.org/10.1021/acs.jpcc.7b09013.

[192] P. Tereshchuk, R.L.H. Freire, C.G. Ungureanu, Y. Seminovski, A. Kiejna, J.L.F. Da Silva, The role of charge transfer in the oxidation state change of Ce atoms in the TM13-CeO2(111) systems (TM = Pd, Ag, Pt, Au): a DFT + U investigation, Phys. Chem. Chem. Phys. 17 (2015) 13520–13530, https://doi.org/10.1039/c4cp06016d.

[193] D. Ma, T. Li, Q. Wang, G. Yang, C. He, B. He, Z. Lu, Z. Yang, Platinum adsorption on ceria: a comparative theoretical study of different surfaces, Appl. Surf. Sci. 394 (2017) 47–57, https://doi.org/10.1016/j.apsusc.2016.10.087.

[194] D. Kunwar, C. Carrillo, H. Xiong, E. Peterson, A. DeLaRiva, A. Ghosh, G. Qi, M. Yang, M. Wiebenga, S. Oh, W. Li, A.K. Datye, Investigating anomalous growth of platinum particles during accelerated aging of diesel oxidation catalysts, Appl. Catal. B. Environ. 266 (2020) 118598, https://doi.org/10.1016/j.apcatb.2020.118598.

[195] J. Li, K. Li, L. Sun, Z. Zhang, Z. Wu, Y. Zhang, X. Yang, Sinter-resistant and high-efficient Pt/CeO2/NiAl2O4/Al2O3@SiO2 model catalysts with "composite energy traps", Sci. China Chem. 63 (2020) 519–525, https://doi.org/10.1007/s11426-019-9678-5.

[196] A. Tovt, L. Bagolini, F. Dvorak, N.D. Tran, M. Vorokhta, K. Beranova, V. Johanek, M.F. Camellone, T. Skala, I. Matolinova, J. Myslivecek, S. Fabris, V. Matolin, Ultimate dispersion of metallic and ionic platinum on ceria, J. Mater. Chem. A 7 (2019) 13019, https://doi.org/10.1039/c9ta00823c.

[197] A.I. Stadnichenko, V.V. Muravev, S.V. Koscheev, V.I. Zaikovskii, H. A. Aleksandrov, K.M. Neyman, A.I. Boronin, Study of active surface centers of Pt/CeO2 catalysts prepared using radiofrequency plasma sputtering technique, Surf. Sci. 679 (2019) 273–283, https://doi.org/10.1016/j.susc.2018.10.002.

[198] A. Zhou, J. Wang, H. Wang, H. Li, J. Wang, M. Shen, Effect of active oxygen on the performance of Pt/CeO2 catalysts for CO oxidation, J. Rare Earths. 36 (2018) 257–264, https://doi.org/10.1016/j.jre.2017.07.008.

[199] A.M. Gänzler, M. Casapu, D.E. Doronkin, F. Maurer, P. Lott, P. Glatzel, M. Votsmeier, O. Deutschmann, J.-D. Grunwaldt, Unravelling the different reaction pathways for low temperature CO oxidation on Pt/CeO2 and Pt/Al2O3 by spatially resolved structure–activity correlations, J. Phys. Chem. Lett. 10 (2019) 7698–7705, https://doi.org/10.1021/acs.jpclett.9b02768.

[200] A.I. Boronin, E.M. Slavinskaya, A. Figueroba, A.I. Stadnichenko, T. Yu, Kardash, O.A. Stonkus, E.A. Fedorova, V.V. Muravev, V.A. Svetlichnyi, A. Bruix, K. M. Neyman, CO oxidation activity of Pt/CeO2 catalysts below 0 °C: platinum loading effects, Appl. Catal. B. Environ. 286 (2021) 119931, https://doi.org/10.1016/j.apcatb.2021.119931.

[201] H.A. Aleksandrov, K.M. Neyman, K.I. Hadjiivanov, G.N. Vayssilov, Can the state of platinum species be unambiguously determined by the stretching frequency of an adsorbed CO probe molecule? Phys. Chem. Chem. Phys. 18 (2016) 22108–22121, https://doi.org/10.1039/C6CP03988J.

[202] M. Melchionna, P. Fornasiero, The role of ceria-based nanostructured materials in energy applications, Mater. Today. 17 (2014) 349–357, https://doi.org/10.1016/j.mattod.2014.05.005.

[203] K. Yoon, Y. Yang, P. Lu, D. Wan, H.-C. Peng, K. Stamm Masias, P.T. Fanson, C. T. Campbell, Y. Xia, A highly reactive and sinter-resistant catalytic system based on platinum nanoparticles embedded in the inner surfaces of CeO2 hollow fibers, Angew. Chem. Int. Ed. English 51 (2012) 9543–9546, https://doi.org/10.1002/anie.201203755.

[204] H. Wang, D. Duan, C. Ma, W. Shi, M. Liang, L. Wang, X. Song, L. Gao, Z. Sun, The preparation and catalytic properties of nanoporous Pt/CeO2 composites with nanorod framework structures, Nanomaterials 9 (2019) 683, https://doi.org/10.3390/nano9050683.

[205] M. Mao, H. Lv, Y. Li, Y. Yang, M. Zeng, N. Li, X. Zhao, Metal support interaction in Pt nanoparticles partially confined in the mesopores of microsized mesoporous CeO2 for highly efficient purification of volatile organic compounds, ACS Catal. 6 (2016) 418–427, https://doi.org/10.1021/acscatal.5b02371.

[206] Q. Wang, Q. Lu, L. Yao, K. Sun, M. Wei, E. Guo, Preparation and characterization of ultrathin Pt/CeO2/Bi2WO6 nanobelts with enhanced photoelectrochemical properties, Dyes Pigm. 149 (2018) 612–619, https://doi.org/10.1016/j.dyepig.2017.11.028.

[207] Q. Zhang, S. Mo, J. Li, Y. Sun, M. Zhang, P. Chen, M. Fu, J. Wu, L. Chen, D. Ye, In situ DRIFT spectroscopy insights into the reaction mechanism of CO and toluene cooxidation over Pt-based catalysts, Catal. Sci. Technol. 9 (2019) 4538, https://doi.org/10.1039/c9cy00751b.

[208] Y. Zhang, Y. Yu, H. He, Oxygen vacancies on nanosized ceria govern the NOx storage capacity of NSR catalysts, Catal. Sci. Technol. 6 (2016) 3950–3962, https://doi.org/10.1039/c5cy01660f.

[209] Y. Zhang, Y. Yu, W. Shan, Z. Lian, H. He, Effect of support preparation with different concentration precipitant on the NOx storage performance of Pt/BaO/CeO2 catalysts, Catal. Today 339 (2020) 135–147, https://doi.org/10.1016/j.cattod.2019.03.021.

[210] H. Yamashita, T. Ogami, K. Kanamura, Hydrothermal synthesis and catalytic activity of PtRh/CeO2/Al2O3 three-way catalysts for automotive exhaust gas, J. Ceram. Soc. Jpn. 126 (2018) 394–401, https://doi.org/10.2109/jcersj2.17240.

[211] M. Mao, Q. Zhang, Y. Yang, Y. Li, H. Huang, Z. Jiang, Q. Hu, X. Zhao, Solar-light-driven CO2 reduction by methane on Pt nanocrystals partially embedded in mesoporous CeO2 nanorods with high light-to-fuel efficiency, Green Chem. 20 (2018) 2857–2869, https://doi.org/10.1039/C8GC01058G.

[212] L.R. Borges, A.G. Marques da Silva, A.H. Braga, L.M. Rossi, M.A. Suller Garcia, P. Vidinha, Towards the effect of Pt°/Ptδ+ and Ce3+ species at the surface of CeO2 crystals: understanding the nature of the interactions under CO oxidation conditions, Chem. Cat. Chem. 13 (2021) 1340–1354, https://doi.org/10.1002/cctc.202001621.

[213] B. Han, H. Li, L. Li, Y. Wang, Y. Zhang, G. Li, Kinetic control of CeO2 nanoparticles for catalytic CO oxidation, J. Mater. Res. 34 (2019) 2201–2208, https://doi.org/10.1557/jmr.2018.456.

[214] T. Andana, M. Piumetti, S. Bensaid, L. Veyre, C. Thieuleux, N. Russo, D. Fino, E. A. Quadrelli, R. Pironea, Nanostructured equimolar ceria-praseodymia for NOx-assisted soot oxidation: insight into Pr dominance over Pt nanoparticles and metal–support interaction, Appl. Catal. B. Environ. 226 (2018) 147–161, https://doi.org/10.1016/j.apcatb.2017.12.048.

[215] T. Andana, M. Piumetti, S. Bensaid, L. Veyre, C. Thieuleux, N. Russo, D. Fino, E. A. Quadrelli, R. Pironea, Ceria-supported small Pt and Pt3Sn nanoparticles for NOx-assisted soot oxidation, Appl. Catal. B. Environ. 209 (2017) 295–310, https://doi.org/10.1016/j.apcatb.2017.03.010.

[216] Y. Li, Y. Du, Y. Wei, Z. Zhao, B. Jin, X. Zhang, J. Liu, Catalysts of 3D ordered macroporous ZrO2-supported core-shell Pt@CeO2-x nanoparticles: effect of the optimized Pt-CeO2 interface on improving the catalytic activity and stability of soot oxidation, Catal. Sci. Technol. 7 (2017) 968–981, https://doi.org/10.1039/c6cy02441f.

[217] N. Jiang, D. Li, L. Liang, Q. Xu, L. Shao, S.-B. Wang, A. Chen, J. Wang, (Metal yolk)/(porous ceria shell) nanostructures for high-performance plasmonic photocatalysis under visible light, Nano Res. 13 (2020) 1354–1362, https://doi.org/10.1007/s12274-019-2599-x.

[218] M. Konsolakis, M. Lykaki, Facet-dependent reactivity of ceria nanoparticles exemplified by CeO2-based transition metal catalysts: a critical review, Catalysts 11 (2021) 452, https://doi.org/10.3390/catal11040452.

[219] G. Chen, Y. Yang, Z. Guo, D. Gao, W. Zhao, H. Yan, W.-W. Wang, C.-J. Jia, G. Sun, Thermally stable and highly active Pt/CeO2@SiO2 catalysts with a porous/hollow structure, Catal. Sci. Technol. 8 (2018) 4413–4419, https://doi.org/10.1039/C8CY01070F.

[220] H. Peng, T. Dong, L. Zhang, C. Wang, W. Liu, J. Bao, X. Wang, N. Zhang, Z. Wang, P. Wu, P. Zhang, S. Dai, Active and stable Pt-Ceria nanowires@silica shell catalyst: design, formation mechanism and total oxidation of CO and toluene, Appl. Catal. B. Environ. 256 (2019) 117807, https://doi.org/10.1016/j.apcatb.2019.117807.

[221] K. Matsuo, N. Nunotani, N. Imanaka, Complete oxidation of formaldehyde over a Pt/CeO2-ZrO2-Bi2O3/SBA-16 catalyst at room temperature, Chem. Lett. 47 (2018) 715–718, https://doi.org/10.1246/cl.180153.

[222] A.R. Supandi, N. Nunotani, N. Imanaka, Liquid-phase oxidation of phenol in facile condition using Pt/CeO2-ZrO2-SnO2 catalyst supported on mesoporous silica SBA-16, J. Environ. Chem. Eng. 5 (2017) 3999–4003, https://doi.org/10.1016/j.jece.2017.07.072.

[223] A.R. Supandi, N. Nunotani, N. Imanaka, Effective p-cresol removal through catalytic liquid-phase oxidation under moderate conditions using Pt/CeO2-ZrO2-SnO2/SBA-16 as a catalyst, J. Asian Ceramic Soc. 8 (2020) 116–122, https://doi.org/10.1080/21870764.2020.1712800.

[224] P.-G. Choi, N. Nunotani, N. Imanaka, High catalytic efficiency in liquid-phase oxidation of 1,4-dioxane using a Pt/CeO2-ZrO2-SnO2/SBA-16 catalyst, Int. J. Appl. Ceram. Technol. 14 (2017) 9–15, https://doi.org/10.1111/ijac.12609.

[225] N.N. Mikheeva, V.I. Zaikovskii, G.V. Mamontov, Synthesis of ceria nanoparticles in pores of SBA-15: pore size effect and influence of citric acid addition, Microporous Mesoporous Mater. 277 (2019) 10–16, https://doi.org/10.1016/j.micromeso.2018.10.013.

[226] A. Taratayko, Y. Larichev, V. Zaikovskii, N. Mikheeva, G. Mamontov, Ag–CeO2/SBA-15 composite prepared from Pluronic P123@SBA-15 hybrid as catalyst for room-temperature reduction of 4-nitrophenol, Catal. Today (2020), https://doi.org/10.1016/j.cattod.2020.05.001. In Press, Corrected Proof.

[227] H. Yang, J. Deng, Y. Liu, S. Xie, Z. Wu, H. Dai, Preparation and catalytic performance of Ag, Au, Pd or Pt nanoparticles supported on 3DOM CeO2-Al2O3 for toluene oxidation, J. Mol. Catal. A Chem. 414 (2016) 9–18, https://doi.org/10.1016/j.molcata.2015.12.010.

[228] J. Gao, S. Gao, J. Wei, H. Zhao, J. Zhang, Catalytic combustion of dimethyl disulfide on bimetallic supported catalysts prepared by the wet-impregnation method, Catalysts 9 (2019) 994, https://doi.org/10.3390/catal9120994.

[229] H.-J. Sedjame, C. Fontaine, G. Lafaye, J. Barbier Jr., On the promoting effect of the addition of ceria to platinum based alumina catalysts for VOCs oxidation, Appl. Catal. B. Environ. 144 (2014) 233–242, https://doi.org/10.1016/j.apcatb.2013.07.022.

[230] S. Pitkäaho, T. Nevanperä, L. Matejova, S. Ojala, R.L. Keiski, Oxidation of dichloromethane over Pt, Pd, Rh, and V2O5 catalysts supported on Al2O3, Al2O3-TiO2 and Al2O3-CeO2, Appl. Catal. B. Environ. 138-139 (2013) 33–42, https://doi.org/10.1016/j.apcatb.2013.01.058.

[231] T.K. Nevanperä, S. Ojala, N. Bion, F. Epron, R.L. Keiski, Catalytic oxidation of dimethyl disulfide (CH3SSCH3) over monometallic Au, Pt and Cu catalysts supported on γ-Al2O3, CeO2 and CeO2-Al2O3, Appl. Catal. B. Environ. 182 (2016) 611–625, https://doi.org/10.1016/j.apcatb.2015.10.012.

[232] E.K. Gibson, E.M. Crabb, D. Gianolio, A.E. Russell, D. Thompsett, P.P. Wells, Understanding the role of promoters in catalysis: operando XAFS/DRIFTS study of CeOx/Pt/Al2O3 during CO oxidation, Catal. Struct. React. 3 (2017) 5–12, https://doi.org/10.1080/2055074X.2017.1278890.

[233] J. Březina, R. Pečinka, P. Boutikos, P. Kočí, Comparison of dual CO light-off effect on Pt/CeO2/γ-Al2O3, Pd/CeO2/γ-Al2O3, Pt/γ-Al2O3 and Pd/γ-Al2O3 in the presence of C3H6, Chem. Eng. Sci. 218 (2020) 115542, https://doi.org/10.1016/j.ces.2020.115542.

[234] Z. Zhou, M.P. Harold, D. Luss, Comparison of Pt-BaO/Al$_2$O$_3$ and Pt-CeO$_2$/Al$_2$O$_3$ for NO$_x$ storage and reduction: impact of cycling frequency, Appl. Catal. B. Environ. 255 (2019) 117742, https://doi.org/10.1016/j.apcatb.2019.05.044.

[235] A.W.-L. Ting, M.P. Harold, V. Balakotaiah, Elucidating the mechanism of fast cycling NO$_x$ storage and reduction using C$_3$H$_6$ and H$_2$ as reductants, Chem. Eng. Sci. 189 (2018) 413–421, https://doi.org/10.1016/j.ces.2018.05.021.

[236] A.W.-L. Ting, M. Li, M.P. Harold, V. Balakotaiah, Fast cycling in a non-isothermal monolithic lean NO$_x$ trap using H$_2$ as reductant: experiments and modeling, Chem. Eng. J. 326 (2017) 419–435, https://doi.org/10.1016/j.cej.2017.05.002.

[237] B.-S. Kim, P.S. Kim, J. Bae, H. Jeong, C.H. Kim, H. Lee, Synergistic Effect of Cu/CeO$_2$ and Pt-BaO/CeO$_2$ catalysts for a low-temperature lean NO$_x$ trap, Environ. Sci. Technol. 53 (2019) 2900–2907, https://doi.org/10.1021/acs.est.8b05329.

[238] B.-S. Kim, H. Jeong, J. Bae, P.S. Kim, C.H. Kim, H. Lee, Lean NO$_x$ trap catalysts with high low-temperature activity and hydrothermal stability, Appl. Catal. B. Environ. 270 (2020) 118871, https://doi.org/10.1016/j.apcatb.2020.118871.

[239] A.A. Salaeva, M.A. Salaev, O.V. Vodyankina, G.V. Mamontov, Synergistic effect of Cu and Zn modifiers on the activity of CrO$_x$/Al$_2$O$_3$ catalysts in isobutane dehydrogenation, Appl. Catal. A Gen. 581 (2019) 82–90, https://doi.org/10.1016/j.apcata.2019.05.018.

[240] A.A. Salaeva, M.A. Salaev, G.V. Mamontov, Effect of Cu modifier on the performance of CrO$_x$/Al$_2$O$_3$ catalysts for isobutane dehydrogenation, Chem. Eng. Sci. 215 (2020) 115462, https://doi.org/10.1016/j.ces.2019.115462.

[241] M.A.L. Rocha, G. Del Ángel, G. Torres-Torres, A. Cervantes, A. Vázquez, A. Arrieta, J.N. Beltramini, Effect of the Pt oxidation state and Ce^{3+}/Ce^{4+} ratio on the Pt/TiO$_2$-CeO$_2$ catalysts in the phenol degradation by catalytic wet air oxidation (CWAO), Catal. Today 250 (2015) 145–154, https://doi.org/10.1016/j.cattod.2014.09.016.

[242] Z. Wang, S. Li, S. Xie, Y. Liu, H. Dai, G. Guo, J. Deng, Supported ultralow loading Pt catalysts with high H$_2$O-, CO$_2$-, and SO$_2$-resistance for acetone removal, Appl. Catal. A Gen. 579 (2019) 106–115, https://doi.org/10.1016/j.apcata.2019.04.018.

[243] Y. Guo, S. Zhang, W. Mu, X. Li, Z. Li, Methanol total oxidation as model reaction for the effects of different Pd content on Pd-Pt/CeO$_2$-Al$_2$O$_3$-TiO$_2$ catalysts, Mol. Catal. 429 (2017) 18–26, https://doi.org/10.1016/j.molcata.2016.11.041.

[244] Y. Shi, J. Wang, R. Zhou, Pt-support interaction and nanoparticle size effect in Pt/CeO$_2$–TiO$_2$ catalysts for low temperature VOCs removal, Chemosphere 265 (2021) 129127, https://doi.org/10.1016/j.chemosphere.2020.129127.

[245] Y. Wei, J. Jiao, X. Zhang, B. Jin, Z. Zhao, J. Xiong, Y. Li, J. Liu, J. Li, Catalysts of self-assembled Pt@CeO$_{2−δ}$-rich core-shell nanoparticles on 3D ordered macroporous Ce$_{1−x}$Zr$_x$O$_2$ for soot oxidation: nanostructure-dependent catalytic activity, Nanoscale 9 (2017) 4558–4571, https://doi.org/10.1039/c7nr00326a.

[246] F. Dong, T. Tanabe, N. Takahashi, H. Shinjoh, Investigation of the effective oxygen storage and release performances on the Pt/CeO$_2$-ZrO$_2$ catalysts by breakthrough method, Catal. Today 332 (2019) 259–266, https://doi.org/10.1016/j.cattod.2018.07.046.

[247] M. Ozawa, M. Misaki, M. Iwakawa, M. Hattori, K. Kobayashi, K. Higuchi, S. Arai, Low content Pt-doped CeO$_2$ and core-shell type CeO$_2$/ZrO$_2$ model catalysts, microstructure, TPR and three way catalytic activities, Catal. Today 332 (2019) 251–258, https://doi.org/10.1016/j.cattod.2018.08.015.

[248] J. Ouyang, Z. Zhao, H. Yang, J. He, S.L. Suib, Surface redox characters and synergetic catalytic properties of macroporous ceria-zirconia solid solutions, J. Hazard. Mater. 366 (2019) 54–64, https://doi.org/10.1016/j.jhazmat.2018.11.083.

[249] Y. Ji, D. Xu, S. Bai, U. Graham, M. Crocker, B. Chen, C. Shi, D. Harris, D. Scapens, J. Darab, Pt- and Pd-promoted CeO$_2$-ZrO$_2$ for passive NO$_x$ adsorber applications, Ind. Eng. Chem. Res. 56 (2017) 111–125, https://doi.org/10.1021/acs.iecr.6b03793.

[250] S. Andonova, Z.A. Ok, N. Drenвschev, E. Ozensoy, K. Hadjiivanov, Pt/CeO$_x$/ZrO$_x$/γ-Al$_2$O$_3$ ternary mixed oxide DeNO$_x$ catalyst: surface chemistry and NO$_x$ interactions, J. Phys. Chem. C. 122 (2018) 12850–12863, https://doi.org/10.1021/acs.jpcc.8b03186.

[251] J.M. Gatica, R.T. Baker, P. Fornasiero, S. Bernal, J. Kašpar, Characterization of the metal phase in NM/Ce$_{0.68}$Zr$_{0.32}$O$_2$ (NM: Pt and Pd) catalysts by hydrogen chemisorption and HRTEM microscopy: a comparative study, J. Phys. Chem. B 105 (2001) 1191–1199, https://doi.org/10.1021/jp003632g.

[252] S. Cimino, L. Lisi, G. Totarella, S. Barison, M. Musiani, E. Verlato, Highly stable core–shell Pt-CeO$_2$ nanoparticles electrochemically deposited onto Fecralloy foam reactors for the catalytic oxidation of CO, J. Ind. Eng. Chem. 66 (2018) 404–410, https://doi.org/10.1016/j.jiec.2018.06.007.

[253] E. Verlato, S. Barison, S. Cimino, L. Lisi, G. Mancino, M. Musiani, F. Paolucci, Electrochemical preparation of nanostructured CeO$_2$-Pt catalysts on Fe-Cr-Al alloy foams for the low-temperature combustion of methanol, Chem. Eng. J. 317 (2017) 551–560, https://doi.org/10.1016/j.cej.2017.02.077.

[254] H. Xiao, J. Wu, X. Wang, J. Wang, S. Mo, M. Fu, L. Chen, D. Ye, Ozone-enhanced deep catalytic oxidation of toluene over a platinum-ceria-supported BEA zeolite catalyst, Molec. Catal. 460 (2018) 7–15, https://doi.org/10.1016/j.mcat.2018.09.005.

[255] W. Bao, H. Chen, H. Wang, R. Zhang, Y. Wei, L. Zheng, Pt nanoparticles supported on N/Ce-doped activated carbon for the catalytic oxidation of formaldehyde at room temperature, ACS Appl. Nano Mater. 3 (2020) 2614–2624, https://doi.org/10.1021/acsanm.0c00005.

[256] M.L. Godoy, E.D. Banús, O. Sanz, M. Montes, E. Miró, V.G. Milt, Stacked wire mesh monoliths for the simultaneous abatement of VOCs and diesel soot, Catalysts 8 (2018) 16, https://doi.org/10.3390/catal8010016.

[257] M.L. Godoy, E.D. Banús, E.E. Miró, V.G. Milt, Single and double bed stacked wire mesh cartridges for the catalytic treatment of diesel exhausts, J. Environ. Chem. Eng. 7 (2019) 103290, https://doi.org/10.1016/j.jece.2019.103290.

[258] X. Hong, Y. Sun, T. Zhu, Z. Liu, Pt-Au/CeO$_2$ catalysts for the simultaneous removal of carbon monoxide and formaldehyde, Catal. Sci. Technol. 6 (2016) 3606–3615, https://doi.org/10.1039/c5cy01744k.

[259] A.H.M. da Silva, T.S. Rodrigues, A.G.M. da Silva, P.H.C. Camargo, J.F. Gomes, J.M. Assaf, Systematic investigation of the effect of oxygen mobility on CO oxidation over AgPt nanoshells supported on CeO$_2$, TiO$_2$ and Al$_2$O$_3$, J. Mater. Sci. 52 (2017) 13764–13778, https://doi.org/10.1007/s10853-017-1481-z.

[260] K. Inoue, S. Somekawa, VOCs treatment with Pt/Co$_3$O$_4$–CeO$_2$ catalyst, Chem. Eng. Technol. 42 (2019) 257–260, https://doi.org/10.1002/ceat.201800245.

[261] L. Yang, X. You, Z. Sheng, D. Ma, D. Yu, X. Xiao, S. Wang, The promoting effect of noble metal (Rh, Ru, Pt, Pd) doping on the performances of MnO$_x$-CeO$_2$/graphene catalysts for the selective catalytic reduction of NO with NH$_3$ at low temperatures, New J. Chem. 42 (2018) 11673–11681, https://doi.org/10.1039/c8nj01417e.

[262] S.W. Lee, H. Lee, D.-G. Lee, S. Oh, I.S. Lee, J.Y. Park, Facile tuning of Metal/Oxide interface in hollow nanoreactor affecting catalytic activity and selectivity, Catal. Letters 149 (2019) 119–126, https://doi.org/10.1007/s10562-018-2600-4.

[263] Q. Li, Z. Yan, N. Wang, Z. Xu, Z. Xu, G. Wang, G. Huang, 0D/2D CeO$_2$ quantum dot/NiO nanoplate supported an ultralow-content Pt catalyst for the efficient oxidation of formaldehyde at room temperature, Catal. Sci. Technol. 10 (2020) 4030–4041, https://doi.org/10.1039/d0cy00653j.

[264] M. Jeong, N. Nunotani, N. Moriyama, N. Imanaka, Introduction of NiO in Pt/CeO$_2$-ZrO$_2$/γ-Al$_2$O$_3$ catalysts for removing toluene in indoor air, Mater. Lett. 208 (2017) 43–45, https://doi.org/10.1016/j.matlet.2017.05.048.

[265] D. Hosseini, P.M. Abdala, F. Donat, S.M. Kim, C.R. Müller, Bifunctional core-shell architecture allows stable H$_2$ production utilizing CH$_4$ and CO$_2$ in a catalytic chemical looping process, Appl. Catal. B. Environ. 258 (2019) 117946, https://doi.org/10.1016/j.apcatb.2019.117946.

[266] X. Hong, J. Chen, Y. Peng, H. Song, C. Wang, J. Li, Deactivation of Pt-Au/TiO$_2$-CeO$_2$ catalyst for co-oxidation of HCHO, H$_2$ and CO at room temperature: degradations of active sites and mutual influence between reactants, Appl. Catal. A Gen. 582 (2019) 117116, https://doi.org/10.1016/j.apcata.2019.117116.

[267] S. Varshney, R. Bar-Ziv, T. Zidki, On the remarkable performance of silver-based alloy nanoparticles in 4-nitrophenol catalytic reduction, Chem. Cat. Chem. 12 (2020) 4680–4688, https://doi.org/10.1002/cctc.202000584.

[268] X. Fu, Y. Liu, J. Deng, L. Jing, X. Zhang, K. Zhang, Z. Han, X. Jiang, H. Dai, Intermetallic compound PtMn$_y$-derived Pt–MnO$_x$ supported on mesoporous CeO$_2$: highly efficient catalysts for the combustion of toluene, Appl. Catal. A Gen. 595 (2020) 117509, https://doi.org/10.1016/j.apcata.2020.117509.

[269] H. Li, L. Cui, Y. Lu, Y. Huang, J. Cao, D. Park, S.-C. Lee, W. Ho, In situ intermediates determination and cytotoxicological assessment in catalytic oxidation of formaldehyde: implications for catalyst design and selectivity enhancement under ambient conditions, Environ. Sci. Technol. 53 (2019) 5230–5240, https://doi.org/10.1021/acs.est.8b06234.

[270] H. Zhang, S. Yuan, J. Wang, M. Gong, Y. Chen, Effects of contact model and NO$_x$ on soot oxidation activity over Pt/MnO$_x$-CeO$_2$ and the reaction mechanisms, Chem. Eng. J. 327 (2017) 1066–1076, https://doi.org/10.1016/j.cej.2017.06.013.

[271] Y. Gao, X. Wu, R. Nord, H. Härelind, D. Weng, Sulphation and ammonia regeneration of a Pt/MnO$_x$-CeO$_2$/Al$_2$O$_3$ catalyst for NO$_x$-assisted soot oxidation, Catal. Sci. Technol. 8 (2018) 1621–1631, https://doi.org/10.1039/c8cy00027a.

[272] Morphological, Compositional, and shape control of materials for catalysis, Stud. Surf. Sci. Catal. 177 (2017) 1–692. Edited by P. Fornasiero, M. Cargnello.

[273] R.M. Palomino, R. Hamlyn, Z. Liu, D.C. Grinter, I. Waluyo, J.A. Rodriguez, S.D. Senanayake, Interfaces in heterogeneous catalytic reactions: ambient pressure XPS as a tool to unravel surface chemistry, J. Electron Spectros. Relat. Phenomena 221 (2017) 28–43, https://doi.org/10.1016/j.elspec.2017.04.006.

[274] G. Zhuang, Y. Chen, Z. Zhuang, Y. Yu, J. Yu, Oxygen vacancies in metal oxides: recent progress towards advanced catalyst design, Sci. China Mater. 63 (2020) 2089–2118, https://doi.org/10.1007/s40843-020-1305-6.

[275] H. Zhang, S. Li, Q. Lin, X. Feng, Y. Chen, J. Wang, Study on hydrothermal deactivation of Pt/MnO$_x$-CeO$_2$ for NO$_x$-assisted soot oxidation: redox property, surface nitrates, and oxygen vacancies, Environ. Sci. Pollut. Res. 25 (2018) 16061–16070, https://doi.org/10.1007/s11356-018-1582-5.

[276] S. Loridant, Raman spectroscopy as a powerful tool to characterize ceria-based catalysts, Catal. Today (2020), https://doi.org/10.1016/j.cattod.2020.03.044. In Press.

[277] A.R. Puigdollers, P. Schlexer, S. Tosoni, G. Pacchioni, Increasing oxide reducibility: the role of metal/oxide interfaces in the formation of oxygen vacancies, ACS Catal. 7 (2017) 6493–6513, https://doi.org/10.1021/acscatal.7b01913.

[278] W. Zhang, M. Pu, M. Lei, Theoretical studies on the stability and reactivity of the metal-doped CeO$_2$(100) surface: toward H$_2$ dissociation and oxygen vacancy formation, Langmuir 36 (2020) 5891–5901, https://doi.org/10.1021/acs.langmuir.0c00644.

[279] Y. Feng, Q. Wan, H. Xiong, S. Zhou, X. Chen, X.I. Pereira Hernandez, Y. Wang, S. Lin, A.K. Datye, H. Guo, Correlating DFT calculations with CO oxidation reactivity on Ga-doped Pt/CeO$_2$ single-atom catalysts, J. Phys. Chem. C. 122 (2018) 22460–22468, https://doi.org/10.1021/acs.jpcc.8b05815.

[280] Y. Yang, S. Wang, Y. Jiang, X. Wu, C. Xia, R. Peng, Y. Lu, CO$_2$ activation and reduction on Pt-CeO$_2$-based catalysts, J. Phys. Chem. C. 123 (2019) 17092–17101, https://doi.org/10.1021/acs.jpcc.9b02878.

[281] J.H. Lee, D.Y. Jo, J.W. Choung, C.H. Kim, H.C. Ham, K.-Y. Lee, Roles of noble metals (M = Ag, Au, Pd, Pt and Rh) on CeO$_2$ in enhancing activity toward soot

oxidation: active oxygen species and DFT calculations, J. Hazard. Mater. 403 (2021) 124085, https://doi.org/10.1016/j.jhazmat.2020.124085.

[282] S. Mo, J. Li, R. Liao, P. Peng, J. Li, J. Wu, M. Fu, L. Liao, T. Shen, Q. Xie, D. Ye, Unraveling the decisive role of surface CeO$_2$ nanoparticles in the Pt-CeO$_2$/MnO$_2$ hetero-catalysts for boosting toluene oxidation: synergistic effect of surface decorated and intrinsic O-vacancies, Chem. Eng. J. 418 (2021) 129399, https://doi.org/10.1016/j.cej.2021.129399.

[283] Y. Lu, C. Thompson, D. Kunwar, A.K. Datye, A.M. Karim, Origin of the high CO oxidation activity on CeO$_2$ supported Pt nanoparticles: weaker binding of CO or facile oxygen transfer from the support? Chem. Cat. Chem. 12 (2020) 1726–1733, https://doi.org/10.1002/cctc.201901848.

[284] W.H. Saputera, J.A. Scott, D. Friedmann, R. Amal, Revealing the key oxidative species generated by Pt-loaded metal oxides under dark and light conditions, Appl. Catal. B. Environ. 223 (2018) 216–227, https://doi.org/10.1016/j.apcatb.2017.08.083.

[285] A.I. Stadnichenko, V.V. Murav'ev, V.A. Svetlichnyi, A.I. Boronin, Platinum state in highly active Pt/CeO$_2$ catalysts from the X-ray photoelectron spectroscopy data, J. Struct. Chem. 58 (2017) (2017) 1152–1159, https://doi.org/10.1134/S0022476617060129.

[286] X. Ding, J. Qiu, Y. Liang, M. Zhao, J. Wang, Y. Chen, New insights into excellent catalytic performance of the Ce-Modified catalyst for NO oxidation, Ind. Eng. Chem. Res. 58 (2019) 7876–7885, https://doi.org/10.1021/acs.iecr.9b00415.

[287] H. Wu, G. Pantaleo, V. La Parola, A.M. Venezia, X. Collard, C. Aprile, L.F. Liotta, Bi- and trimetallic Ni catalysts over Al$_2$O$_3$ and Al$_2$O$_3$-MO$_x$ (M=Ce or Mg) oxides for methane dry reforming: Au and Pt additive effects, Appl. Catal. B. Environ. 156-157 (2014) 350–361, https://doi.org/10.1016/j.apcatb.2014.03.018.

[288] F. Dvořák, M.F. Camellone, A. Tovt, N.-D. Tran, F.R. Negreiros, M. Vorokhta, T. Skála, I. Matolínová, J. Mysliveček, V. Matolín, S. Fabris, Creating single-atom Pt-ceria catalysts by surface step decoration, Nat. Commun. 7 (2016) 10801, https://doi.org/10.1038/ncomms10801.

[289] K. An, S. Alayoglu, N. Musselwhite, S. Plamthottam, G. Melaet, A.E. Lindeman, G. A. Somorjai, Enhanced CO oxidation rates at the interface of mesoporous oxides and Pt nanoparticles, J. Am. Chem. Soc. 135 (2013) 16689–16696, https://doi.org/10.1021/ja4088743.

[290] T.W. van Deelen, C. Hernández Mejía, K.P. de Jong, Control of metal-support interactions in heterogeneous catalysts to enhance activity and selectivity, Nat. Catal. 2 (2019) 955–970, https://doi.org/10.1038/s41929-019-0364-x.

[291] Q. Hu, K. Cao, Y. Lang, R. Chen, S. Chu, L. Jia, J. Yue, B. Shan, Improved NO-CO reactivity of highly dispersed Pt particles on CeO$_2$ nanorod catalysts prepared by atomic layer deposition, Catal. Sci. Technol. 9 (2019) 2664–2672, https://doi.org/10.1039/c9cy00212j.

[292] Z.Z. Khan, I.A. Khan, I. Khan, M.H. Sarwar Wattoo, A. Badshah, Pt and Co$_3$O$_4$ supported on ceria and zirconia for the catalytic reduction of N$_2$O in the presence of CO, Solid State Sci. 98 (2019) 106035, https://doi.org/10.1016/j.solidstatesciences.2019.106035.

[293] P. Zhao, J. Zhang, J. Jiang, H. Wang, T. Xie, Y. Lin, Synthesis and study on photogenerated charge behavior of novel Pt/CeO$_2$/ZnO ternary composites with enhanced photocatalytic degradation activity, J. Inorg. Organomet. Polym. Mater. 30 (2020) 1–11, https://doi.org/10.1007/s10904-019-01312-y.

[294] H. Sasakia, H. Matsushita, K. Sakamoto, T. Sakamoto, M. Maeda, Formation of Pt$_3$O$_4$ particles on PtO$_2$–CeO$_2$ solid solution, J. Phys. Chem. Solids 135 (2019) 109097, https://doi.org/10.1016/j.jpcs.2019.109097.

[295] J. Resasco, L. Derita, S. Dai, J.P. Chada, M. Xu, X. Yan, J. Finzel, S. Hanukovich, A.S. Hoffman, G.W. Graham, S.R. Bare, X. Pan, P. Christopher, Uniformity is key in defining structure-function relationships for atomically dispersed metal catalysts: the case of Pt/CeO$_2$, J. Am. Chem. Soc. 142 (2020) 169–184, https://doi.org/10.1021/jacs.9b09156.

[296] S.M. Kozlov, K.M. Neyman, Effects of electron transfer in model catalysts composed of Pt nanoparticles on CeO$_2$(111) surface, J. Catal. 344 (2016) 507–514, https://doi.org/10.1016/j.jcat.2016.10.014.